LIÈGE université Library

https://lib.uliege.be

https://matheo.uliege.be

Characterization and Three-Dimensional Modeling of the Lamellar Architecture within Bone Osteons

Auteur : Lakhel, Ahmed
Promoteur(s) : Ruffoni, Davide
Faculté : Faculté des Sciences appliquées
Diplôme : Master en ingénieur civil biomédical, à finalité spécialisée
Année académique : 2024-2025
URI/URL : http://hdl.handle.net/2268.2/23338

Avertissement à l'attention des usagers :

Tous les documents placés en accès ouvert sur le site le site MatheO sont protégés par le droit d'auteur. Conformément aux principes énoncés par la "Budapest Open Access Initiative"(BOAI, 2002), l'utilisateur du site peut lire, télécharger, copier, transmettre, imprimer, chercher ou faire un lien vers le texte intégral de ces documents, les disséquer pour les indexer, s'en servir de données pour un logiciel, ou s'en servir à toute autre fin légale (ou prévue par la réglementation relative au droit d'auteur). Toute utilisation du document à des fins commerciales est strictement interdite.

Par ailleurs, l'utilisateur s'engage à respecter les droits moraux de l'auteur, principalement le droit à l'intégrité de l'oeuvre et le droit de paternité et ce dans toute utilisation que l'utilisateur entreprend. Ainsi, à titre d'exemple, lorsqu'il reproduira un document par extrait ou dans son intégralité, l'utilisateur citera de manière complète les sources telles que mentionnées ci-dessus. Toute utilisation non explicitement autorisée ci-avant (telle que par exemple, la modification du document ou son résumé) nécessite l'autorisation préalable et expresse des auteurs ou de leurs ayants droit.





UNIVERSITY OF LIÈGE
SCHOOL OF ENGINEERING

CHARACTERIZATION AND THREE-DIMENSIONAL MODELING OF THE LAMELLAR ARCHITECTURE WITHIN BONE OSTEONS

MASTER'S THESIS CONDUCTED BY

AHMED LAKHEL

WITH THE AIM OF OBTAINING A
MASTER'S DEGREE IN BIOMEDICAL ENGINEERING

SUPERVISOR:
DAVIDE RUFFONI

POST-DOC SUPERVISOR:
ALEXANDRA TITS

CO-SUPERVISOR:
RICHARD WEINKAMER

PHD SUPERVISOR:
EDOARDO PEDRINAZZI

ACADEMIC YEAR 2024-2025

Abstract

Bone strength is a crucial concept in biomechanics and clinical practice. For bone to withstand significant loads without fracturing, it must exhibit high mechanical resistance. This resistance is the result of the combination of three essential factors: bone mass, geometry, and intrinsic quality.

Bone mineral density (BMD) is considered as an indirect clinical indicator of bone strength. Although this measurement accounts for a significant part of the mechanical performance of bone, it remains insufficient on its own to accurately predict the risk of fracture. Other determining aspects, such as bone microarchitecture, remain insufficiently explored and deserve further investigation in ongoing research.

In this context, this thesis presents an innovative approach to investigate bone architecture at the micrometer length scale. The focus is placed on the morphology of the lamellae forming cortical bone osteons combining experiments and mathematical modeling. To achieve this, images acquired with second harmonic generation (SHG) microscopy of three osteons from a bone sample collected from the femur midshaft of a 56-year-old patient were processed using a series of rigorous methods, detailed throughout this report.

Firstly, the lamellar morphology is analyzed and characterized based on the raw images of each osteon. Although these images correspond to transverse sections, we were able to reconstruct the lamellae in several longitudinal planes of the osteon, where they appear in the form of relatively straight lines. This observation motivated the fitting of linear regressions to derive a first mathematical representation of these structures. This representation allowed us to extract relevant morphological features and revealed that lamellae have a conical geometry when observed in three dimensions, thereby challenging the cylindrical model that has long been accepted in the literature.

Secondly, a protocol was developed to reconstruct the imaged osteons as individual mathematical objects, allowing for simple and coherent interpretation. Although SHG microscopy provides high-contrast images, the resulting signal remains complex and can clearly be simplified. To achieve this, we proposed a series of steps aimed at reducing the SHG signal to a unit-thickness object which exhibits smoother appearance. Specifically, following post-processing that included binarization, the images were skeletonized. Given the quite circular geometry of the lamellae, transforming the images into polar coordinates proved useful for fitting smoothing splines along the lamellae. This initial reconstruction, performed manually, was limited to three transverse slices per osteon. Then, it became necessary to develop a method for estimating the lamellar structure across all other slices, based both on the reconstructions from the three reference slices and on the linear regressions obtained from the first part of this work. Ultimately, we demonstrated that, overall, the proposed protocol is relatively robust and provides a reliable approximation of the raw SHG signal.

This work is not limited to a detailed exploration of cortical bone microarchitecture; it also paves the way to a wide range of research opportunities. In particular, the simplified model of lamellae that we propose appears promising for being superimposed onto images of the lacuno-canalicular network and osteocytes, with the aim of gaining more insight into the interactions involved between these structures that coexist within bone tissue, and whose formation results from successive temporal episodes. For instance, our model could be used to estimate the number of canaliculi crossing a lamella formed at time t, and an adjacent, more internal lamella formed at time $t + 1$, thereby enabling a temporal assessment of cortical bone development.

Résumé

La résistance osseuse constitue un concept fondamental en biomécanique, ainsi que dans le domaine clinique. Pour que l'os puisse supporter des charges importantes sans se fracturer, il doit faire preuve d'une résistance mécanique élevée. Cette résistance découle de la combinaison de trois facteurs essentiels : la masse osseuse, sa géométrie, et sa qualité intrinsèque.

La densité minérale osseuse est considérée comme un indicateur clinique indirect de la résistance de l'os. Bien que cet indicateur permette d'expliquer, en grande partie, les performances mécaniques de l'os, il demeure insuffisant pour prédire, avec précision, le risque de fracture. D'autres éléments déterminants, tels que la microarchitecture osseuse, restent encore insuffisamment explorés et méritent une investigation plus approfondie dans la recherche actuelle.

Dans cette optique, cette thèse propose une approche innovante pour explorer l'architecture osseuse à l'échelle micrométrique. L'accent est mis sur la morphologie des lamelles constituant les ostéons de l'os cortical, étudiée et caractérisée en combinant des processus expérimentaux et de la modélisation mathématique. Pour y parvenir, des images acquises par microscopie à génération de seconde harmonique de trois ostéons d'un échantillon osseux, prélevé de la diaphyse moyenne fémorale d'un patient âgé de 56 ans, ont fait l'objet d'une succession de méthodes rigoureuses, détaillées tout au long de ce rapport.

Dans un premier temps, la morphologie des lamelles est étudiée et caractérisée sur base des images brutes de chaque ostéon. Bien que ces images correspondent à des coupes transversales, nous avons pu reconstituer les lamelles dans plusieurs coupes longitudinales à l'ostéon, où elles apparaissent sous forme de lignes relativement rectilignes. Cette observation a motivé l'ajustement de régressions linéaires afin de dériver une première représentation mathématique de ces structures. Cette représentation nous a permis d'extraire des caractéristiques morphologiques pertinentes et a notamment révélé que les lamelles présentent une géométrie conique, lorsqu'elles sont observées en trois dimensions, remettant ainsi en question le modèle cylindrique généralement admis dans la littérature.

Ensuite, un protocole a été développé dans le but de reconstruire les ostéons imagés sous la forme d'objets mathématiques individuels, interprétables de manière simple et cohérente. Bien que les images acquises par génération de seconde harmonique (SHG) offrent un contraste élevé, le signal demeure complexe et peut clairement faire l'object d'une simplification. À cette fin, nous avons proposé une série d'étapes afin de réduire le signal SHG à un objet d'épaisseur unitaire, avec un aspect plus régulier. Concrètement, après un post-traitement incluant la binarisation des images, celles-ci ont été squeletisées. Étant donné la géométrie globalement circulaire des lamelles, le passage en coordonnées polaires s'est avéré utile pour faciliter l'ajustement de courbes de type smoothing splines sur les lamelles. Cette première reconstruction, réalisée manuellement, n'a été effectuée que sur trois coupes transversales par ostéon. Il a donc été nécessaire de développer une technique permettant d'estimer la structure des lamelles dans l'ensemble des autres coupes, en s'appuyant à la fois sur les reconstructions obtenues dans ces trois coupes de référence, et sur les régressions linéaires issues de la première phase de ce travail. Finalement, nous avons illustré que, dans l'ensemble, le protocole développé s'est avéré relativement robuste et a permis une approximation fidèle du signal SHG brut.

Ce travail ne se limite pas à une exploration approfondie de la microarchitecture de l'os cortical ; il ouvre également la voie à de nombreuses perspectives de recherche. En particulier, le modèle simplifié des lamelles que nous proposons semble prometteur pour être superposé aux images du réseau lacuno-canaliculaire et des ostéocytes, dans le but d'en apprendre plus sur les interactions entre ces structures coexistant au sein du tissu osseux, et dont la formation résulte d'épisodes temporels successifs. À titre d'exemple, notre modèle pourrait être utilisé pour évaluer le nombre de canalicules traversant une lamelle - formée en un temps t - et une lamelle adjacente, plus interne - formée en un temps $t + 1$ - ouvrant ainsi la voie à une évaluation temporelle du développement de l'os cortical.

Acknowledgments

Nicki Minaj once said: "*it's not cool to be a loser. Go to school, graduate*". So here I am, achieving a Master's thesis. This project is the result of several months of hard work, new experiences, and discoveries - each more enriching than the last, even if sometimes quite scary and challenging. But I have never been alone. Throughout this journey, there was always a shoulder I could lean on, no matter the need I felt. For this reason, I would like to properly express my sincere gratitude to all people who, in one way or another, helped me complete this thesis under the best possible conditions. This part of the manuscript being the most personal, which truly reflects who I am, I would like to fully express my thoughts here, and write down the words I was not always able to say out loud.

This work was, for me, an introduction to the world of research. It allowed me to discover so many things, both from a scientific and personal point of view. It was not always easy, but I am glad I overcame this challenge - something I could never have done on my own.

Firstly, I would like to thank Davide, my supervisor, for giving me the opportunity to work on this subject, and for taking the time to support me throughout this journey. Without you, I would have never had the enriching experience I lived in Berlin and at the Max Planck Institute. I must confess, however, that I still cannot figure out how - with your overbooked schedule ("I'm very busy", as he used to say with an Italian accent) - we managed to have so many meetings.

Thank you, Alex, for agreeing to supervise me throughout the whole project, from beginning to end. This work would have never been the same without you. Thank you for your patience, the time you dedicated (whether it was for the thesis in general or for reviewing the report), the energy you gave and your brilliant ideas – and thank you as well for the gossip sessions between two serious talks. Thank you for the moments we shared at the MPI - but also outside of it - for the symposium and for the confocal imaging session. Seeing you so enthusiastic about my work, my progress and my results truly warmed my heart, especially during times of self-doubt. You made my experience in Berlin so enjoyable, and I am really glad I had the chance to make a new friend along the way.

Thank you, Ricci, for believing in me and for always pushing me forward, despite the obstacles I tended to place in my own path. Your remarkable intuition and suggestions helped me bring out the best in this work. Thank you for your availability (because two-hour meetings are no small thing!), and for giving me the opportunity to complete this thesis at the MPI.

Thank you, Edo, for your guidance and presence throughout the year, and for getting involved in my work. Thank you for your advice, and for taking the time to meticulously correct my manuscript. Thank you for saying "bravo" for even the smallest things I do - even when I just say "good" in response to you asking how I am doing. It means a lot to me.

Thank you also to the team members of the MBBM lab. Hearing your valuable advice and experiences did me a lot of good.

I would like to thank my parents – especially my mom – for the emotional support you gave me throughout the year, even during the toughest times. I hope I have made you proud.

Thank you to my closest friends - Clémence, Fanny, Julien, Linpha and Lucas - for all the funny and unforgettable moments we shared throughout our studies. I could never have dreamed of better friends, though I do wonder how you will manage to laugh without me next year.

Thank you to my cousin, Kaouthar, for all your support, for always listening to my stories about the thesis - down to the smallest details - and for bringing me motivation so many times in moments I felt at my lowest. Seeing each other progress will forever be precious to me. In our voice messages, your "I feel like crying" and my "I feel like killing myself" at the slightest inconvenience will always make me laugh.

Finally, I would like to deeply thank my best friend, Fanny, who has always been there for me, for better or worse. God knows this year has been turbulent (to say the least), but nothing would have been the same without you. Thank you for the moments we cherished together, for all the days we spent together laughing like hyenas for hours in my office instead of working (glad I helped extend your life expectancy — and sorry to the people in the office next door), and for comforting me during more delicate times. Having someone in my life with whom a single glance can express so many words means a lot to me. I am grateful that fate placed us on each other's way.

I am thankful to have been able to carry out this project, and to be able to call it "*my work*". I feel really proud of myself.

Table of contents

Abstract 2

Résumé 3

Acknowledgments 4

Introduction 7

1. Background 8
- 1.1 Human bone . . . 8
  - 1.1.1 Bone quality . . . 8
  - 1.1.2 Various forms of bone . . . 8
  - 1.1.3 Functions of bone . . . 9
  - 1.1.4 Hierarchical structure of bone . . . 9
  - 1.1.5 Bone remodeling . . . 17
- 1.2 Bone imaging . . . 19
  - 1.2.1 Overview of a few imaging techniques . . . 19
  - 1.2.2 Second harmonic generation . . . 24
- 1.3 Main aims of the thesis . . . 29

2. Experimental Part 30
- 2.1 Sample preparation . . . 30
- 2.2 Second harmonic imaging . . . 31

3. Structural analysis of lamellae 34
- 3.1 Introduction . . . 34
- 3.2 Simplifying hypothesis . . . 34
- 3.3 Image segmentation . . . 35
- 3.4 Osteon centering . . . 38
- 3.5 Osteon reslicing . . . 40
- 3.6 Linear regression fit . . . 41
- 3.7 Relative slopes . . . 42
- 3.8 Lamellar absolute angle vs. osteon rotation angle . . . 43
- 3.9 Results and discussion . . . 45

4. Reconstruction of an osteon as a mathematical object 59
- 4.1 Introduction . . . 59
- 4.2 Image skeletonization . . . 59
- 4.3 Lamellar surface area . . . 62
- 4.4 Reconstruction of an osteon at specific slices . . . 62
- 4.5 Reconstruction of an entire osteon . . . 66
- 4.6 Interlamellar thickness . . . 69
- 4.7 Results and discussion . . . 70

5. Perspectives 78
- 5.1 Limitations . . . 78
- 5.2 Future work . . . 80

Conclusion 85

Appendices 86

References 93

Introduction

Bone tissue is classified into two distinct types: trabecular bone and cortical bone. Cortical bone, also known as compact bone, is made up of structural units called osteons. These osteons consist of sheets of concentric layers of collagen fibers, called lamellae, which are organized around the Haversian canal — the central feature of the osteon which houses the blood and lymphatic vessels (Fratzl and Weinkamer, 2007). Unlike trabeculae, osteons are relatively well-defined structural units in space, which allows us to analyze them individually — as was done in this study. Since each osteon results from a discrete and temporally well-defined process, it makes sense to treat it as a separate region of interest, almost independently of its surroundings.

In vertebrates, bone exhibits great mechanical properties. It is capable of transmitting loads and resisting deformation, while simultaneously deforming sufficiently to absorb energy and limit the initiation and propagation of cracks (Kanis, 2002; Seeman and Delmas, 2006). Notably, bone has the ability to adapt its microscopic architecture to the mechanical requirements of the environment, thereby optimizing its structural performance over time (R. B. Martin, 1991).

Despite its remarkable mechanical properties, bone remains susceptible to fracture risks. Diseases such as osteoporosis are known to alter the microscopic structure of bone — particularly by decreasing bone density — which in turn increases the risk of fracture (McClung, 2005). To reduce this risk, bone must exhibit sufficient strength. Bone strength goes hand in hand with the concept of bone quality, which is determined by its composition, structure, architecture, and remodeling dynamics (Compston, 2006). Bone strength — and therefore fracture risk — is often evaluated by measuring bone mineral density (BMD). However, BMD alone is not sufficient to fully explain bone strength (Mazess, 1982). In this study, another factor that contributes to bone strength — yet underexplored — is investigated: microarchitecture. More specifically, our attention is directed toward the micrometric-scale organization of cortical bone, particularly at the level of osteons. Given that osteons are the result of the bone remodeling process — which is also a key contributor to bone strength — we also aim to explore the relationship between microarchitecture and bone remodeling.

To carry out our analysis, we applied image processing techniques to images of osteons acquired through second harmonic generation (SHG) microscopy, the goal being to extract relevant information and offer a novel description of cortical bone.

This thesis is organized into five chapters. The first chapter introduces all the theoretical background necessary for the reader to properly understand the project, and outlines the specific objectives of this study. In particular, it offers a detailed description of bone structure across several length scales, introduces the concept of bone remodeling, and presents a few imaging techniques commonly used for bone imaging. Particular attention is given to SHG microscopy, since this technique enabled the acquisition of the images at the center of this work.

The second chapter presents the experimental part that led to the acquisition of SHG images. This chapter is treated separately, mainly because it was not conducted by the author of this thesis. It contains relevant details related to the preparation and imaging of the bone sample.

As this project is articulated in two main parts, one chapter is dedicated to each. The third chapter introduces the protocol developed to investigate the three-dimensional organization of lamellae within the imaged osteons. Once the intended objectives are mentioned, the chapter describes the methodology, followed by a presentation and discussion of the results. The fourth chapter focuses on the implementation of a protocol designed to model an osteon using a simplified representation. The objective is to reduce the osteon to a single, well-defined mathematical object. Each step of the approach is detailed, followed by a presentation and discussion of the corresponding results.

Finally, the fifth chapter outlines the limitations of the current work, and suggests potential improvements, followed by a wide range of directions intended for future work.

Chapter 1

Background

This chapter aims to introduce the reader to all the fundamental concepts and background knowledge necessary to understand the thesis. First, the bone structure, and in particular that of the osteon, is described in details. The basics of bone remodeling are explained as well. Then, a few imaging techniques used to characterize bone are presented. These include imaging methods that will be mentioned later in this report, as well as technologies specifically appropriate for collagen fibers imaging. Special emphasis is placed on one method in particular: second harmonic generation. Since this is the technique used to produce the images at the core of this work, it is important to understand the physical principle, the operating mechanisms, the interpretation of the images, as well as the limitations of this type of imaging. Finally, the main objectives of this thesis are presented.

1.1 Human bone

Bone is a complex biological material that is part of the musculoskeletal system of vertebrates. In humans, bones are organs that perform various functions, providing shape, mechanical support, and protection to the body, as well as facilitating movement (Oryan, n.d.).

It is a composite material, consisting of mineral crystals, an organic extracellular matrix, cells, lipids and water (Boskey and Coleman, 2010). Water represents about 20% of bone mass, whereas dry weight consists of approximately 30 to 35% organic matrix and 65 to 70% inorganic substances (Pilitsis et al., 2002).

Bone is made of cells that are divided into four classes: osteoblasts, osteocytes, osteoclasts and mesenchymal osteoprogenitor cells (Webb and Tricker, 2000), each having a specific and crucial role in bone development. Moreover, like other organs, bone is vascularized, enabling it to receive nutrients and oxygen through blood flowing in its vessels, and therefore modulating its metabolic activity (Lafage-Proust et al., 2015).

1.1.1 Bone quality

Bone strength is determined by three main factors: bone mass, bone geometry, and bone quality (Compston, 2006). As many other biological materials, bone must fulfill two conflicting mechanical properties: it must be stiff enough to resist deformation and take load, but also flexible enough to absorb energy by deforming, thus limiting crack formation and propagation (Seeman and Delmas, 2006).

Among the determinants of bone quality are bone composition, bone structure, bone microarchitecture, and bone remodeling. All of these aspects are interdependent, so an irregularity in one will likely lead to alterations in others.

Bone remodeling is a key factor that highly affects the other determinants, and its measurement is crucial in clinical practice (Compston, 2006). Traditional bone strength measurements, such as bone densiometry (*i.e.* evaluation of bone mineral density), are not sufficient to reliably predict the risk of bone fracture (Delmas and Seeman, 2004). For this reason, other characteristics of bone composition and structure that might play a role in bone strength have been, and are still being investigated.

1.1.2 Various forms of bone

Bone comes in various shapes, which allows it to fulfill specific biomechanical functions (Fratzl and Weinkamer, 2007):

- Long bones, such as the femur and the tibia, are hollow inside and provide stability against bending and buckling.
- Short bones, like vertebrae, provide stability against compression and are capable of shock absorption.
- Plate-like bones, or flat bones, such as the skull, protect vital organs (*e.g.* the brain), and ensure muscle attachment.

1.1.3 Functions of bone

The musculoskeletal system, and particularly bone, is multifunctional. Indeed, bone has several functions (Currey, 2002):

(a) Hematopoiesis: it produces red blood cells and stem cells in the red bone marrow, housed in trabecular bone (located at the ends of long bones, in vertebrae, and in flat bones). On the other hand, the shaft of the bone is filled with yellow bone marrow, which stores fat.

(b) Mineral storage: 99% of calcium ions is stored in the skeleton. Through the process of bone remodeling, blood calcium levels are regulated by bone resorption and deposition.

(c) Protection of vital organs: bone is remarkably capable of highly absorbing energy while still having a low weight. While cortical bone provides rigidity and the ability to bear load, trabecular bone (which is porous and therefore lightweight) can transfer load and absorb energy.

(d) Support and motion: the skeleton is a structural support to the human body. In addition, it works together with the joints and muscles to allow motion.

1.1.4 Hierarchical structure of bone

From the organ level to the basic chemical components, bone extends over approximately 9 hierarchical levels (as Figure 1.1 shows) (Reznikov et al., 2014).

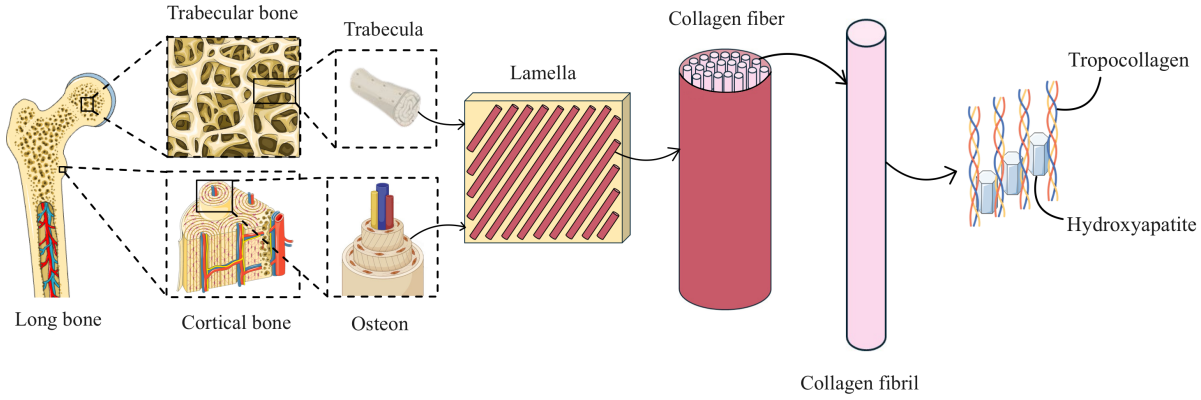


Figure 1.1: Schematic illustration of the hierarchical organization of bone. This Figure includes images adapted from Servier Medical Art., from Cortical Versus Trabecular Bone – My Endo Consult, (n.d.), and Bucky (n.d.).

A) Nanoscale: biomolecules and structural components

At the nanoscale, bone is composed of three main components: an organic matrix (mainly made of tropocollagen, *i.e.* a triple helix of type I collagen), mineral carbonated hydroxyapatite (made of calcium phosphate) and water.

The tropocollagen molecules are organized to form collagen fibrils, with a diameter ranging from 80 to 120 nm (Reznikov et al., 2014).

Hydroxyapatite, which is the mineral phase of bone, is arranged in the form of thin platelets, filling the space available between the collagen fibrils. These building blocks are arranged in a staggered fashion (see Figure 1.2), allowing bone to exhibit both high stiffness and toughness at the nanometer length scale, which are known to be conflicting mechanical properties (Fratzl and Weinkamer, 2007).

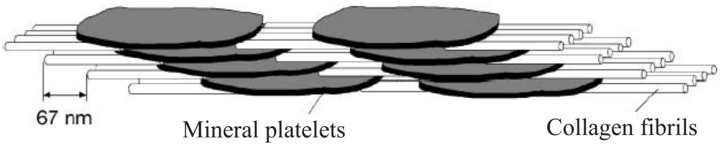


Figure 1.2: Schematic illustration of bone at the nanoscale. The mineral platelets typically have a thickness that ranges between 1.5 and 4.5 nm, and a length that can reach up to 200 nm. Figure from (Fratzl et al., 2004).

At a slightly higher length scale, collagen fibrils are also arranged in a staggered configuration, surrounded by an extrafibrillar matrix to form a collagen fiber.

B) Microscale: lamellar organization

Collagen fibers align in parallel to form a sheet called lamella. In principle, within the same lamella, these fibers have a common orientation, forming a specific angle with respect to the vertical axis.

C) Mesoscale: trabeculae

At the mesoscale (ranging from about 50 to 500 µm in length) - depending on the type of bone tissue considered at the macroscale (see Subsection 1.1.4 E) - lamellae can organize together to form bone structural units called lamellar packets (also called bone packets, trabecular packets or hemi-osteons), separated by erosive hypermineralized cement lines that are rich in osteopontin. Within the same lamellar packet, the lamellae are all aligned, but their orientation is different from that of another packet (as can be seen in Figure 1.3) (Reznikov et al., 2015).

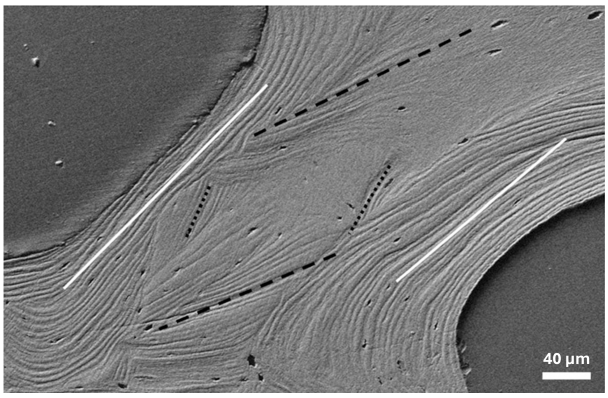


Figure 1.3: Scanning electron microscope (SEM) image of a trabecula showing multiple lamellar packets. Within a single bone packet, lamellae exhibit a common orientation, whereas the orientation varies between adjacent bone packets. Pairs of parallel lines indicate the lamellar orientation. Figure adapted from (Reznikov et al., 2015).

Bone packets are organized to form trabeculae, which exhibit either a plate-like or a rod-like shape. Typically, a trabecular rod is about 50 to 300 µm in diameter (Rho et al., 1998). As shown in Figure 1.4B, each bone packet is not only characterized by a particular lamellar orientation, but also by a specific mineral content which increases over time. This heterogeneity in the intrinsic properties of bone is due to the process of trabecular bone remodeling and mineralization (Currey, 2002).

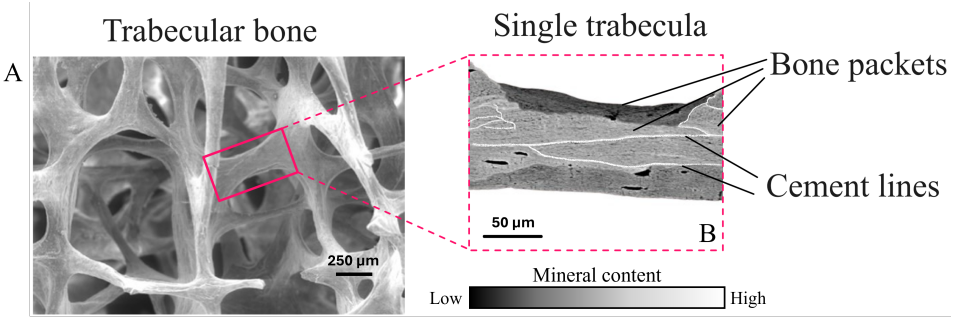


Figure 1.4: **A.** Scanning electron microscope image of trabecular bone. **B.** Quantitative backscattered electron image of a single trabecula. The bone packets and the cement lines are highlighted. As indicated by the qualitative color bar, darker regions correspond to younger bone packets, with lower mineral content. Image courtesy of Paul Roschger (Ludwig Boltzmann Institute of Osteology, Vienna).

D) Mesoscale: osteons

In the other type of bone tissue, lamellae organize themselves to form structural elements called osteons, or Haversian systems. In principle, an osteon has a cylindrical shape which is about 200 µm in diameter, formed around what are known as the Haversian canals (approximately 50 µm in diameter). These canals surround blood and lymphatic vessels which ensure the transport of oxygen and nutrients to bone. A nerve and some interstitial fluid are also contained in the Haversian canal (Pfeiffer et al., 2006).

An osteon is made up of several concentric sheets, *i.e.* several lamellae (Fratzl and Weinkamer, 2007), as can be seen in Figure 1.5A. However, the exact definition of a lamella depends from one study to another. On the one hand, some say that a sheet of collagen fibers with a common orientation is a lamella, which is the Gebhardt model (Gebhardt, 1906). On the other hand, others call that a sub-lamella, and one lamellar unit would be a series of many sub-lamellae, therefore containing collagen fibers with different orientations (Varga et al., 2013; Schrof et al., 2014).

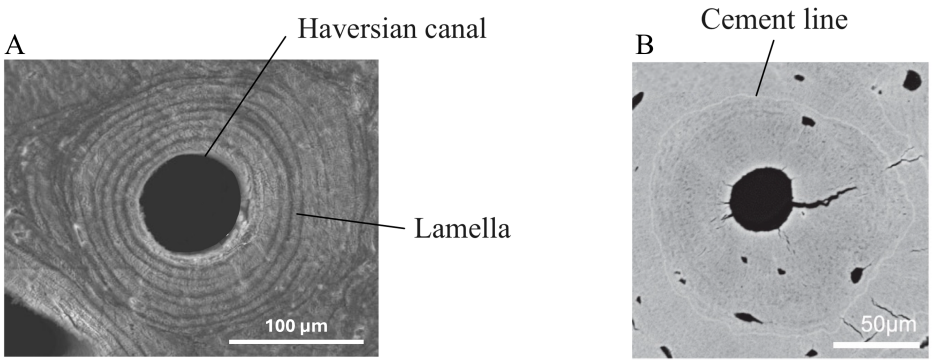


Figure 1.5: **A.** SEM image and **B.** qBEI image of two osteons. Figures adapted from (Pazzaglia et al., 2012) and (Milovanovic et al., 2018).

When the same osteon is imaged using both SEM and polarized light microscopy (see Figure 1.6) - both of which are explained in Subsection 1.2.1 - a good correspondence was observed between bright bands of the polarized light images and the grooves - which correspond to the interlamellar space - of the SEM images (where the collagen fibers are in plane with respect to the plane of the section), as well as between the dark bands and the space between two grooves - which corresponds to a lamella - where the collagen fibers are not in plane with respect to the plane of the section. This configuration is illustrated in Figure 1.7A. The assumption of an alternative model stems from the fact that birefringence bands could sometimes be observed within the same lamella. Consequently, this means that the orientation of the collagen fibers may gradually vary within the same lamella (Mitchell and Van Heteren, 2016). This is what the alternative configuration, shown in Figure 1.7B, aims to illustrate.

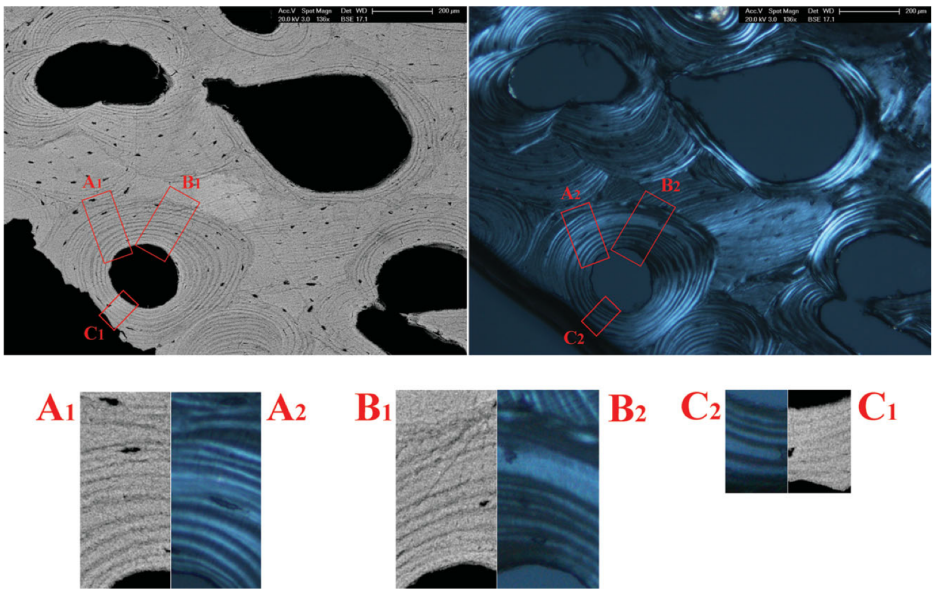


Figure 1.6: SEM image (on the top-left) and polarized light image (on the top-right) of the same osteon. Boxes 1, 2 and 3 have been cut to compare both types of images. Figure from (Pazzaglia et al., 2012).

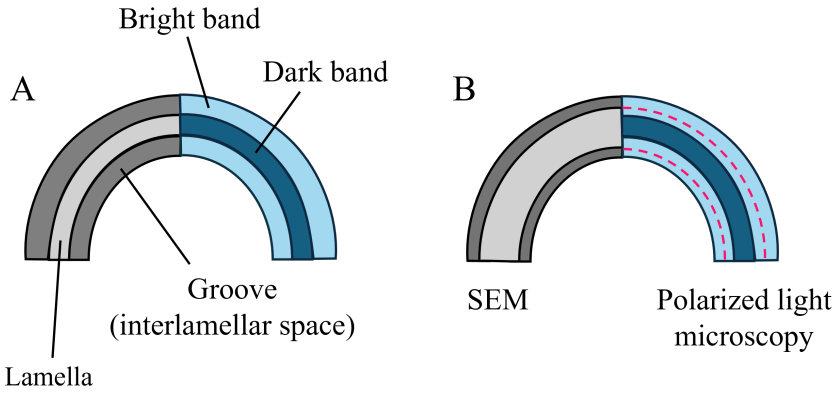


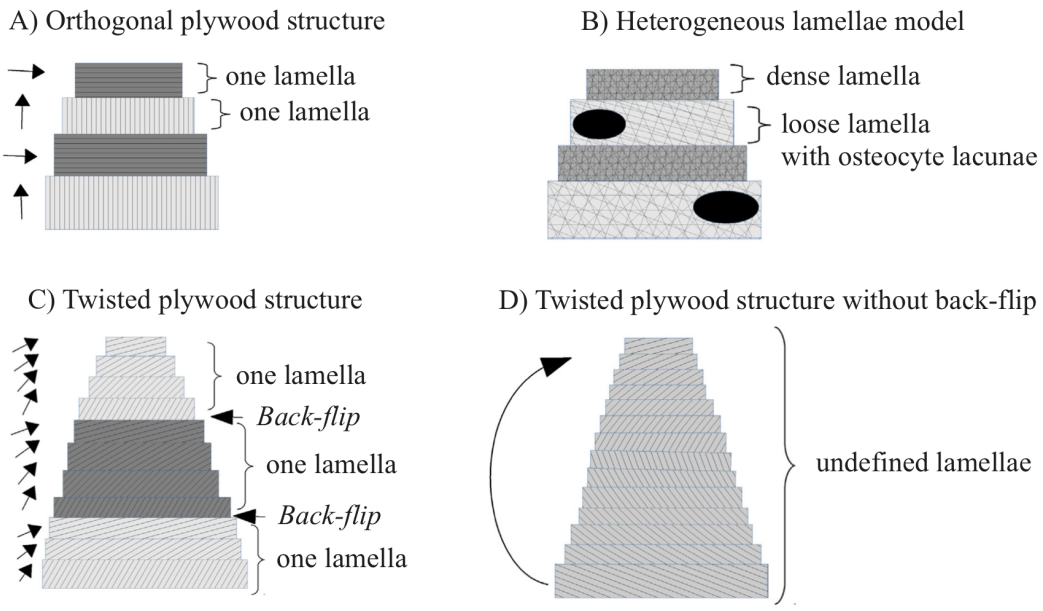
Figure 1.7: Schematic representation of the two configurations observed when comparing the same osteon using both SEM and polarized light microscopy. **A.** Configuration in which a bright band in the polarized light image perfectly matches to a groove in the SEM image. **B.** Alternative configuration, in which a single lamella (defined by the region between two consecutive grooves in the SEM image) corresponds to more than one band in the polarized light microscopy image, suggesting the presence of multiple collagen fiber orientations within a single lamella. The red dashed lines depict the boundaries of the lamella.

Different models have been proposed in the literature regarding how collagen fibers could be arranged in adjacent lamellae (or sub-lamellae) (Pazzaglia et al., 2012). Here, the main models are listed, with a schematic representation in Figure 1.8):

- The **orthogonal plywood structure** - illustrated in Figure 1.8A - is the simplest model, first introduced by Gebhardt (Gebhardt, 1906). This model suggests that successive lamellae are made up of collagen fibers that are offset by 90°.
- The **heterogeneous model** (Marotti et al., 2013) - which can be visualized in Figure 1.8B - emphasizes that osteons are made of alternating dense lamellae, composed of a large number of collagen fibers, and loose lamellae (or disorganized lamellae), which are much less dense in terms of collagen fibers. Within these loose lamellae, osteocyte lacunae can be found. In this model, the

collagen fibers do not have a preferred orientation within the same lamella, but are rather organized in small bundles, where they lay parallel to each other. Between two neighboring bundles, the angle defined by the collagen fibers changes.

- In the **twisted (or fanning) plywood model** (Varga et al., 2013; Schrof et al., 2014), the orientation of the collagen fibers changes continuously, always rotating in the same direction (either clockwise, as in Figure 1.8D, or anti-clockwise, but not both). However, there are cases where the gradual change in fiber orientation is periodic (at times clockwise, at other times anti-clockwise), which gives rise to the **oscillatory plywood structure** - as displayed in Figure 1.8E. In these configurations lamellae are undefined, meaning that the boundaries of the lamellae are not specified.
- The **twisted plywood structure with back-flip** (Weiner et al., 1999; Wagermaier et al., 2006) - which can be seen in Figure 1.8C - is a model in which the fiber orientation is offset by approximately 30° between one layer (or sub-lamella) and the subsequent one. After about 5 layers (depending on the study), the lamella ends, as there is a 120° back-flip which allows for a return to the original orientation, marking the beginning of a new lamella.
- The **three motif model** (Reznikov et al., 2013; Reznikov et al., 2014) - displayed in Figure 1.8F - is more complex and consists of three successive distinct patterns:
  - When the degree of dispersion (which measures the variability in fiber orientation within the same sub-lamellar unit) is low, collagen fibers can either maintain their orientation constant over a certain thickness, forming a **unidirectional lamella**, or change it progressively, forming a **fanning (or twisted) plywood-like lamella**. In both cases, the lamella is said to be ordered.
  - When the degree of dispersion is high, a **disordered (or loose) lamella** is formed, which is less dense in terms of collagen fibers. This kind of lamella often serves as a transition zone between two ordered lamellar units. The collagen fibers within these units were found to finely extend and somehow "invade" the ordered patterns, causing the disordered configuration to appear locally within ordered lamellae, in between the fibers. Furthermore, these disordered fibers were found to exhibit a weak preferred orientation, radial to the Haversian canal, rather than longitudinal or transverse.



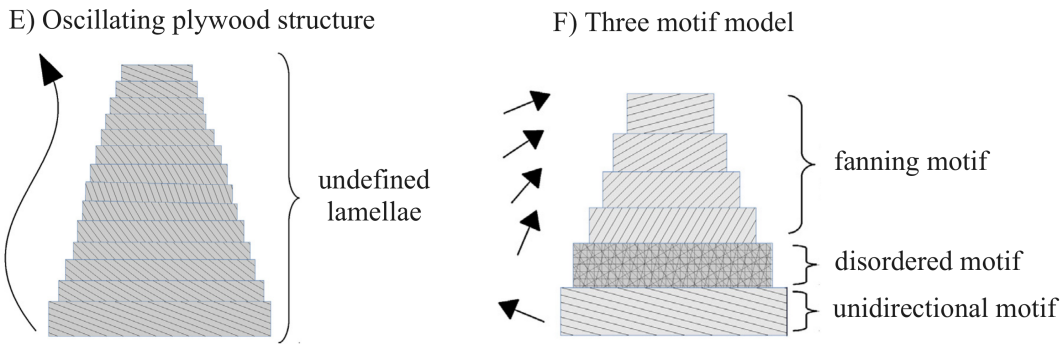


Figure 1.8: Schematic representation of the main lamellar structures and models that can be found in the literature. Arrows indicate the preferred orientations of collagen fibers. Figure adapted from (Mitchell and Van Heteren, 2016).

It should be noted that, while lamellae are mostly considered structurally homogeneous, differing only in collagen fibers orientation and keeping the same collagen density, some studies suggest that lamellae may instead differ primarily in composition, indicating structural heterogeneity (Marotti, 1993; Marotti et al., 2013). These studies sustain that lamellar bone is rather composed of alternating dense lamellae (rich in collagen fibers) and loose lamellae (poor in collagen fibers). In these lamellae, the fibers are interwoven, therefore in contradiction with the idea of a common orientation.

E) Macroscale: trabecular and cortical bone

At the macroscale (mm length scale), trabeculae form a very porous interconnecting network called trabecular or cancellous bone (see Figure 1.4A) (Rho et al., 1998). It forms the interior of bone and it is surrounded by a dense shell called cortical or compact bone, essentially made of osteons.

As the scheme in Figure 1.9 shows, compact bone consists of osteons (forming the so-called osteonal bone) surrounded by peripheral lamellar structures. These outer lamellae are arranged in broad concentric layers and typically measure 5 to 10 µm in thickness (Currey, 2002).

In osteonal bone, osteons are arranged side by side, separated by interstitial lamellae, which are residual structures of previously existing bone. Osteons have a length that ranges between 1 and 3 mm, and each one is bordered and delimited from the rest of the structure by a cement line (as shown in Figure 1.5B), also referred to as reversal line.

The Haversian canals contained within osteons are interconnected by Volkmann's canals, forming an interconnected vascular system (Cohen and Harris, 1958; Maggiano et al., 2016). These canals also connect the central vascular canal to the bone periosteum, a thin membrane that covers long bones.

Within cortical bone reside the osteocytes — the most abundant bone cells — embedded in the matrix. These cells are organized into a network known as the connected cellular network (CCN) (Moss, 1997). The lacunae house the osteocyte cell bodies, while their processes extend through tiny channels called canaliculi. Together, the lacunae and canaliculi form a porous structure referred to as the lacunocanalicular network (LCN) (Schneider et al., 2010).

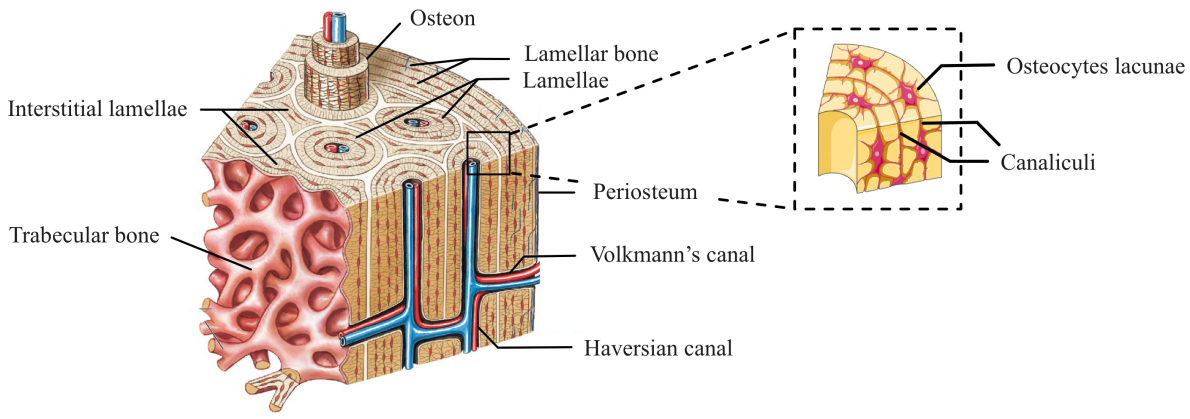


Figure 1.9: Schematic representation of cortical bone. Figure adapted from ("Diagramme De Organization of Compact and Spongy Bone," n.d.).

In human compact bone, osteons are classified in two main classes. Primary osteons form on the external surface of bone, around the blood capillaries of the periosteum. They develop in areas where there is no bone material, through the process of bone modeling. Secondary osteons, which are prevalent, form within the cortical bone, through the remodeling process, *i.e.* through bone resorption followed by bone deposition (Doube, 2022).

Secondary osteons are also referred to as Type I osteons (Andreasen et al., 2018). They are highly diverse in terms of density, geometrical properties and circularity (Cooke et al., 2022), giving rise to variants that have been described in the literature, which can be observed in Figure 1.10.

Typically, Type II osteons include all osteons described as different from "ordinary" osteons, and by definition, they usually have two concentric cement lines (van Tol et al., 2020). For this reason, the term "osteon-in-osteon" is often used to refer to them (Redelstorff, 2012). They are the result of a process called intra-osteonal remodeling, in which a Haversian system is formed within the boundaries of another one (Maggiano et al., 2016). A new reversal line is formed, which looks quite different from that of an ordinary secondary osteon, as the inner border of a type II osteon cuts irregularly through existing lamellae (Cooke et al., 2022).

Type II osteons are quite similar to what are called double-zonal osteons. However, the formation process is completely different, as double-zonal osteons are the result of a disrupted formation, followed by a sudden and rapid increase in mineralization of lamellae during bone remodeling. This results in a smooth dense continuous reversal line, in contrast to that of type II osteons, which is rather rough and irregular (Raguin and Streeter, 2018).

Another variant of Haversian systems are called drifting osteons, sometimes referenced as Waltzing osteons (Frost, 1964), or eccentric osteons (Sedlin et al., 1963). They result from a continuous resorption on one side of the Haversian system and continuous formation on the other (Robling and Stout, 1999). Consequently, the osteon becomes flattened in one plane and stretched transversely to this plane. In addition, the Haversian canal appears to be off-centered within the osteon. The migration of the bone multicellular unit (BMU), the basic functional unit of bone remodeling that involves the cellular activity (Raguin and Streeter, 2018), does not only move transversely, but longitudinally as well (Robling and Stout, 1999).

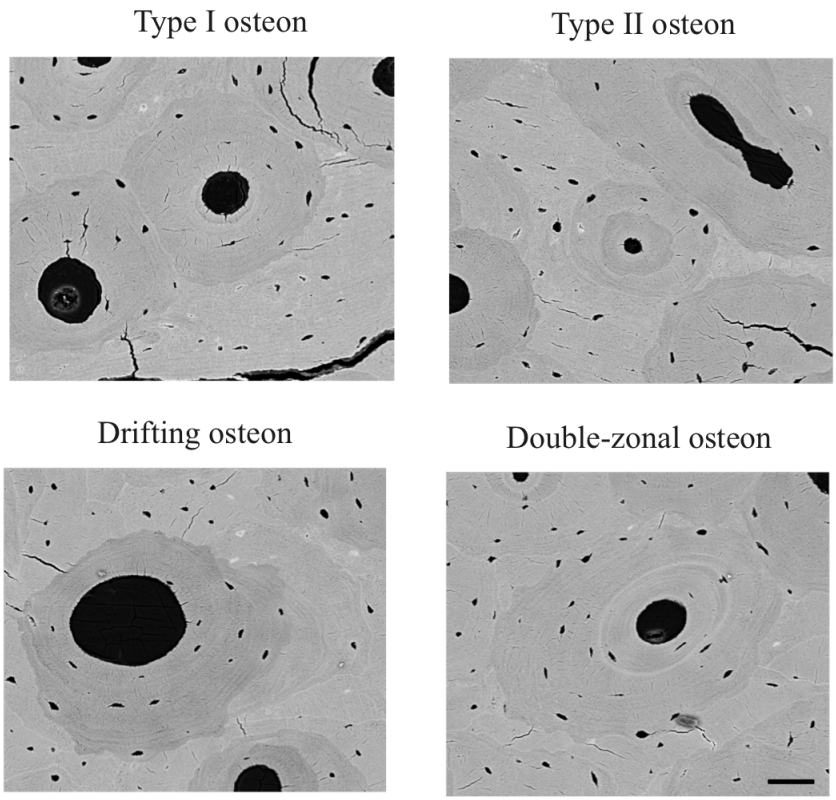


Figure 1.10: Representative qBEI images illustrating different types of osteons in human cortical bone. The scale bar represents 50 µm. Figure adapted from (Cantamessa, 2025).

Variations exist even among ordinary secondary osteons. Indeed, Haversian systems have many different shapes, and their geometrical properties differ a lot from one osteon to another. Typically, the morphology of osteons is simplified, considering them as roughly circular in cross-section (Hennig et al., 2015), forming a perfect 3D cylinder in the longitudinal plane. However, osteon formation is a biological process, thus noisy and influenced by multiple factors; therefore, this osteon model may be oversimplified. Instead, osteons generally display elliptical cross-sectional shapes (Hennig et al., 2015; Britz et al., 2009). This allows to describe the morphology of Haversian systems as a spectrum, with cross-sectional shapes going from perfect circles (for which the two axes of the ellipse are almost the same in dimension) to very long elliptical osteons (for which the major axis is much larger than the minor one). Finally, it is also clear that there exist many more irregular shapes that do not fit this elliptical model, drifting osteons are one example. Nevertheless it can be said that, depending on how osteon remodeling takes place, an osteon might have a completely random shape.

Furthermore, another feature of osteons that can be used to characterize them, is the shape and location of the Haversian canal. Some osteons may look perfectly circular, but the Haversian canal would be completely off-centered (as in drifting osteons), resulting in a Haversian system with a highly asymmetric wall thickness and, therefore a Haversian canal which is close to one side of the cement line. Interestingly, a recent study focused on quantifying the degree of wall thickness asymmetry in human osteons and, through a computational model developed by the authors, explored how osteon formation mechanisms - namely delayed initiation of bone deposition, differences in osteoblast density, and differences in osteoid deposition rates, the three occurring in specific regions of the formation front (all of these concepts are detailed in Subsection 1.1.5) - might account for this asymmetry (Hegarty-Cremer et al., 2024). In particular, the heterogeneity of osteoblast density along the resorption cavity is closely related to the local geometry of the bone surface, notably through its curvature. Indeed, as the curvature increases, the cell density increases as well, leading to enhanced deposition of bone matrix (Alias and Buenzli, 2017; Alias and Buenzli, 2018; Hegarty-Cremer et al., 2021).

In addition, similar to osteons, some Haversian canals exhibit a circular appearance, while others appear to be more elliptical or irregular in shape.

F) Organ level
Bone, as a whole, contains an outer shell of cortical bone, while the inner volume is made of trabecular bone. The shaft of long bones, known as the diaphysis, contains a hollow central space called the medullary cavity (or marrow cavity), where the bone marrow is housed (Currey, 2002).

1.1.5 Bone remodeling

As a biological material, bone evolves continuously from the embryonic stage to advanced age.
Bone maturation is the result of three tissue-level activities: bone growth, bone modeling and bone remodeling (Frost, 1991).

While bone growth is associated with enlarging size by increasing the number of cells and the amounts of intracellular materials, bone modeling is about adapting the size and shape of the bone organ to ensure mechanical strains are within a range of tolerance. Modeling occurs during growth and takes places through two approaches. The first one is micromodeling, which is the process of organizing cells and collagen fibers during their formation. It is, for instance, what makes the difference between an articular cartilage and a growth plate cartilage. The second one is macromodeling, which controls if, when and where new tissue forms or old tissue is removed. It controls the shape, size and strength of bones.

On the other hand, bone remodeling is paired with turnover, maintenance, replacement and repair. It involves one main actor, referred to as the BMU (basic multicellular unit). BMUs work in a specific triplet mechanism, known as the ARF sequence: Activation $\rightarrow$ Resorption $\rightarrow$ Formation (Hadjidakis and Androulakis, 2006):

(a) Activation of the cell phenotypes involved in bone remodeling, which are osteoblasts, osteoclasts and bone lining cells (Sims and Vrahnas, 2014).

(b) Bone resorption by osteoclasts. These cells work together to dissolve the so-called old bone matrix, by secreting an acidic substance.

(c) Bone formation by osteoblasts. These cells coordinate their activity locally, to produce a lamella by depositing aligned collagen fibers (Jones et al., 1975). The resulting unmineralized bone matrix, called osteoid, is laid down in the space previously resorbed by osteoclasts. This process is known as osteogenesis.

BMUs are involved in both compact and cancellous bone remodeling. However, as the structure is very different, the process is not exactly the same. In fact, in cortical bone, osteoclasts dig tunnels through the solid material, while in trabecular bone they rather dig trenches over the trabecular surface. Afterwards, osteoblasts fill these tunnels and trenches, creating newly formed osteons and hemi-osteons, respectively (van Oers et al., 2008). In this report, bone remodeling is explained in details for osteons; Figure 1.11 displays part of the description.

During bone resorption, osteoclasts work simultaneously to form the so-called cutting cone (Jaworski and Lok, 1972), or resorption front. This cone extends longitudinally at about 40 µm per day and radially about 7 µm per day (Doube, 2022).

During bone deposition, osteoblasts coordinate in the form of a patch team at the edge of what is known as the closing cone (Lassen et al., 2017), or formation front. This cone progresses longitudinally at about 44 µm per day (in the dog (Jaworski and Lok, 1972)). The synchronized activity of osteoblasts is possible thank to signaling via the gap junction intercellular network (Watkins et al., 2011). Osteoblasts have three possible faiths: undergo apoptosis (Jilka et al., 1998), get trapped into the newly formed bone matrix and differentiate into osteocytes (Dallas and Bonewald, 2010) or differentiate into bone lining

cells that cover the Haversian canal surface. The latter may then dedifferentiate back into osteoblasts (Matic et al., 2016).

Together, the simultaneous action of osteoblasts and osteoclasts is called the cutting cone-closing cone dynamics, which is sustained via complex biological signaling mechanisms. Indeed, osteoclasts communicate with osteoblasts, osteocytes and bone lining cells through inhibitory and stimulatory factors (Sims and Vrahnas, 2014).

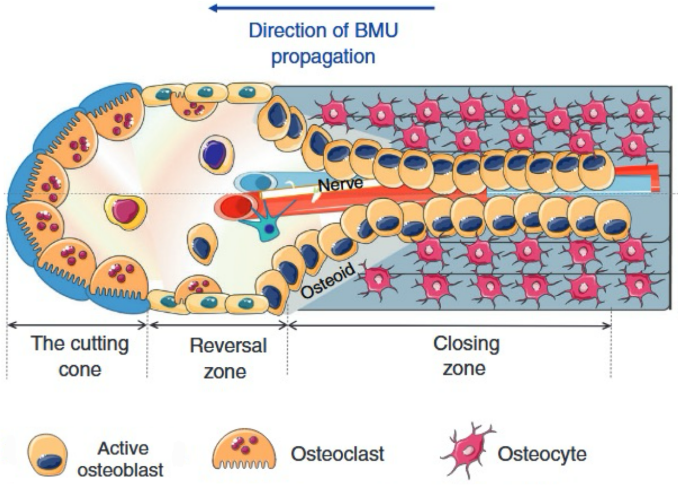


Figure 1.11: Schematic representation of bone remodeling. Other secondary cells are involved in the process, but their mechanism of action is not relevant in the context of this thesis. Figure from (Bolamperti et al., 2022).

Bone remodeling is believed to allow the skeletal system to adapt to micromechanical requirements, control bone losses near the bone marrow, repair microdamage, and replace one kind of tissue with another (Frost, 1991).

Once the osteoid is deposited, it gets mineralized by hydroxyapatite crystals. This causes a continuous increase in its mineral content. The dynamics of mineralization is described by the mineralization law, which consists of two phases. The primary mineralization is characterized by a rapid increase in the mineral content during a few days up to 70% of the final value, followed by the secondary mineralization, which involves a slow and gradual maturation of the mineral phase (Meunier and Boivin, 1997). Bone is very heterogeneous in terms of mineral content (Ruffoni et al., 2008). In trabecular bone, bone packets show very different gray scales - thus different mineral contents - when imaged by qBEI (see Figure 1.4B). Cortical bone, in turn, shows a higher bone mineral density, but a similar mineral heterogeneity around the mean compared to trabecular bone (Lerebours et al., 2020).

One tool allowing to describe how the calcium content is distributed in bone is the BMDD (bone mass density distribution), shown in Figure 1.16C. This approach, which consists of reporting the frequency of appearance of calcium contents within a sample, is useful to assess bone quality, by evaluating effects of bone turnover, mineralization kinetics and average tissue age on the intrinsic properties of bone (Ruffoni et al., 2007; Meunier and Boivin, 1997). Remarkably, despite the inherent heterogeneity of calcium content within bone, the BMDD is almost identical across all healthy individuals, regardless of their age, sex, ethnicity, or skeletal site (P. Roschger et al., 2003; P. Roschger et al., 1998). Consequently, any significant deviation in the BMDD is indicative of a bone disease — such as osteoporosis — or the effect of a therapeutic treatment (P. Roschger et al., 2003). The BMDD can therefore be used as a valuable clinical tool for the diagnosis of bone pathologies and for the assessment of the efficacy of related treatments (Ruffoni et al., 2007; P. Roschger et al., 2008; Ruffoni et al., 2008).

1.2 Bone imaging

1.2.1 Overview of a few imaging techniques

In order to characterize bone, various techniques can be used. Among these methods, imaging techniques allow to visualize bone at different length scales, and extract either qualitative or quantitative information. Each technique allows to observe one or a few more specific properties of bone. Imaging modalities mainly differ based on the underlying physical principle. A wide range of energy sources can be used to interact with the bone structure, allowing them to be visualized. In this section, a few selected techniques involving X-rays, electrons, and light are introduced. These methods are either used to visualize collagen fiber orientation — which is of significant interest in our study — or are referenced at some point throughout this report.

A) Computed tomography

Computed tomography - also known as CT - is used to generate three-dimensional images of samples. Briefly, a finely focused x-ray is sent from a source, passes through the sample and reaches a detector, where it is converted to visible light, creating the image that can be visualized. Seeing the structure of the sample is possible because x-rays interact with the material and are absorbed. Depending on the atomic composition of the sample, as well as its density, the intensity of the x-ray is more or less attenuated, resulting in a brighter or darker light signal on the image (Baird and Taylor, 2017; Philips, 2024).

From a clinical point of view, computed tomography allows imaging of bones and soft tissues, lesions, as well as tumors affecting multiple organs of the body, making it a useful tool for diagnosing a wide variety of diseases (National Institute of Biomedical Imaging and Bioengineering, 2023).

Computed tomography has proven useful for imaging both trabecular and cortical bone. Indeed, as it is made of calcium, which has a relatively high atomic number, the x-ray is considerably attenuated. This allows to clearly visualize the sample on the image. The contrast between the structure and the surrounding tissue makes this even easier, thanks to the lower atomic number of their chemical compounds (Tits, 2023; Bouxsein et al., 2010).

One of the main advantages of this technique, other than its three-dimensionality, is that it allows to image bone at different length-scales (as can be seen in Figure 1.12), ranging from several hundred micrometers down to a few hundred nanometers (Stauber and Müller, 2008).

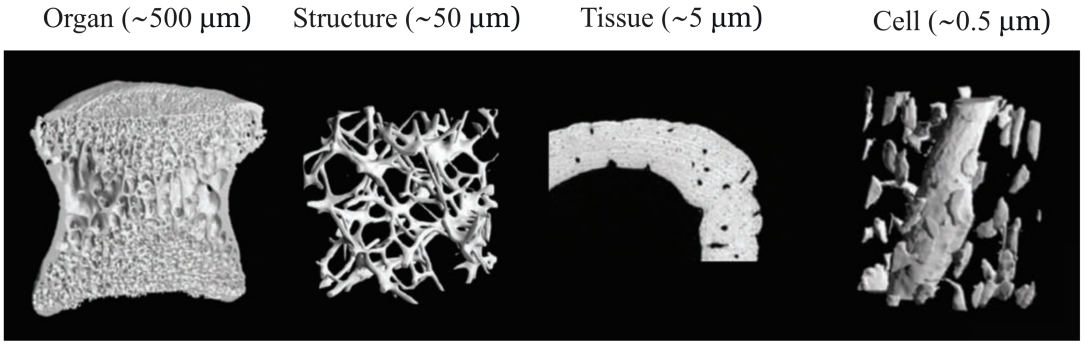


Figure 1.12: Overview of different images that can be obtained by CT, over different length scales. Figure adapted from (Müller, 2009).

X-ray micro-computed tomography (or micro-CT) uses the principles of computed tomography at high resolution (micron to sub-micron). In the past, synchrotron X-ray phase nano tomography has been used to investigate the three-dimensional orientation of the mineralized collagen fibrils in lamellar bone. This technique is based on a principle similar to micro-CT, except that the resolution is much higher (in the order of nanometers) and the electrons that generate the X-ray beam are first accelerated by a synchrotron, resulting in a higher flux, thus allowing for faster scans. This technique has enabled the

identification of the twisted fanning arrangement of collagen fibers (Varga et al., 2013). The advantage of this method is that it reduces artifacts related to tissue preparation, sample alignment, limited field of view, and lack of a third dimension (Mitchell and Van Heteren, 2016) - drawbacks often encountered in other imaging techniques. However, access to synchrotron facilities is limited, due to its high-cost and complex technology. In fact, experimental time is allocated to users through peer-review and open competition. It is also known that at the sub-micron scale, beam stability (X-ray) is not guaranteed, nor is the mechanical stability between the source, the sample, and the detector, which often leads to blurry images (Withers, 2007).

B) Scanning electron microscopy

Scanning electron microscopy (SEM) detects scattered electrons which are emitted from the surface of the sample. Therefore, it provides details about the surface topography, morphology and composition (as Figure 1.13 shows), in contrast to transmission electron microscopy (TEM), which gives information about the bulk of the material (Akhtar et al., 2018). SEM is capable of generating images with high resolution, in the nanometer range (Goldstein, 2012).

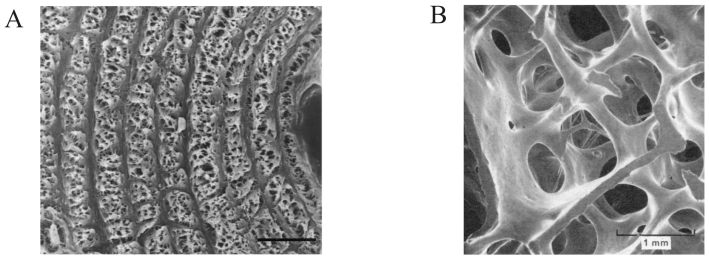


Figure 1.13: Overview of different images that can be obtained by SEM. **A.** Image of the wall of a secondary osteon, in which the lamellae can be distinguished (the scale bar represents 10 µm). **B.** Image of the trabecular network. Pictures respectively taken from (Ardizzoni, 2001) and (Whitehouse and Dyson, 1974).

SEM has been previously used to assess the morphology of osteons and, in particular, the orientation of collagen fibers within lamellae (Pazzaglia et al., 2012), which is of particular interest in the context of this work. In that specific study, the surface of the sample was cut with a saw and chemically polished to expose the tip of the collagen fibrils (as can be seen in Figure 1.14A). The reversal line (indicated by the thick arrow), and the inter-lamellar lines (which serve as transition regions between consecutive lamellae, indicated by the thin arrows) are characterized by a lower density of collagen fibers. The reversal line of the osteon appears larger and more irregular compared to the inter-lamellar lines. In addition, the lamellae seem to contain collagen fibers which are oriented approximately perpendicularly to the cut plane, while the collagen fibers contained in the inter-lamellar space lie rather parallel to the section plane. The fiber density does not seem to differ much between two adjacent lamellae.

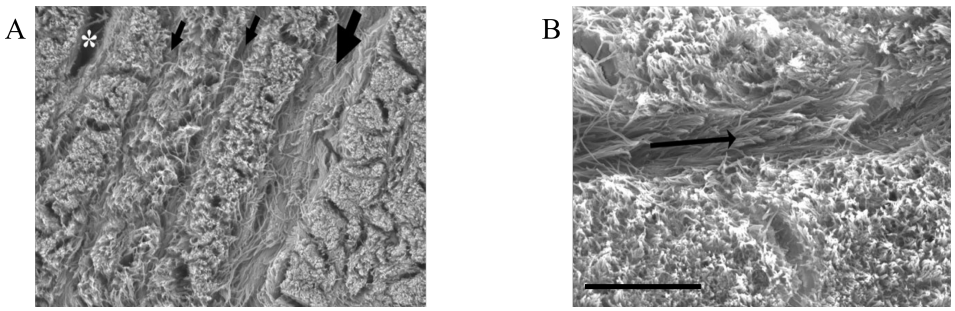


Figure 1.14: **A.** SEM image of the wall of an osteon, including lamellae, inter-lamellar lines (indicated by thin arrows), and the reversal line (indicated by a thick arrow), the asterisk highlights a lacuna. **B.** Image of an inter-lamellar line. The scale bar represents 5 µm. Images adapted from (Pazzaglia et al., 2012).

SEM, coupled with TEM, has also allowed to observe both the orthogonal plywood and the twisted plywood architectures, even in the same osteons of the same bone specimen (Giraud-Guille, 1988; Weiner et al., 1997). In addition, it highlighted the dense and loose lamellae, that refute the concept of uniform collagen fiber orientation (Marotti, 1993; Marotti et al., 2013). In such images, loose lamellae appeared to be thicker than dense lamellae.

A variant of SEM has been recently developed, called focused ion beam SEM (FIB-SEM). It involves milling a sample using a focused ion beam, followed by imaging the polished surface using conventional SEM (Hirashima et al., 2020).

C) Confocal laser scanning microscopy

Confocal laser scanning microscopy (CLSM) allows to perform 3D imaging of biological samples with high resolution. A striking feature is its ability to select specific planes within thick samples. Essentially, a laser source emits a beam of light that illuminates a pinhole. This ray then passes through a beam splitter and is focused by an objective lens onto a specific spot in the focal plane, where the sample is located. The light reflected from this spot is partially redirected by the beam splitter toward the pinhole positioned in front of the detector (Tata and Raj, 1998). The pinhole prevents some out-of-focus signals, which are emitted by the sample, from reaching the detector. Therefore, the latter measures only the light emitted from the focal plane, as this plane in the sample and the pinhole are at conjugate planes of focus, hence the name *confocal* (Blouin et al., 2018). The 3D image (stack of 2D images) can then be obtained by moving the sample in the z-direction, therefore detecting the signal emitted from a particular plane.

An additional feature of CLSM is that it enables the detection of different fluorochromes, which label specific components of the sample (Blouin et al., 2018). This is feasible by tuning the wavelength of the light that is sent to the specimen. Additionally, a staining solution must be used as a fluorescent dye. For instance, rhodamine allows visualization of the lacuno-canalicular network (Kerschnitzki, 2012) - as can be seen in 1.15B - since it rapidly diffuses throughout the sample, staining the internal surfaces of the tissue's pores (Tits, 2023).

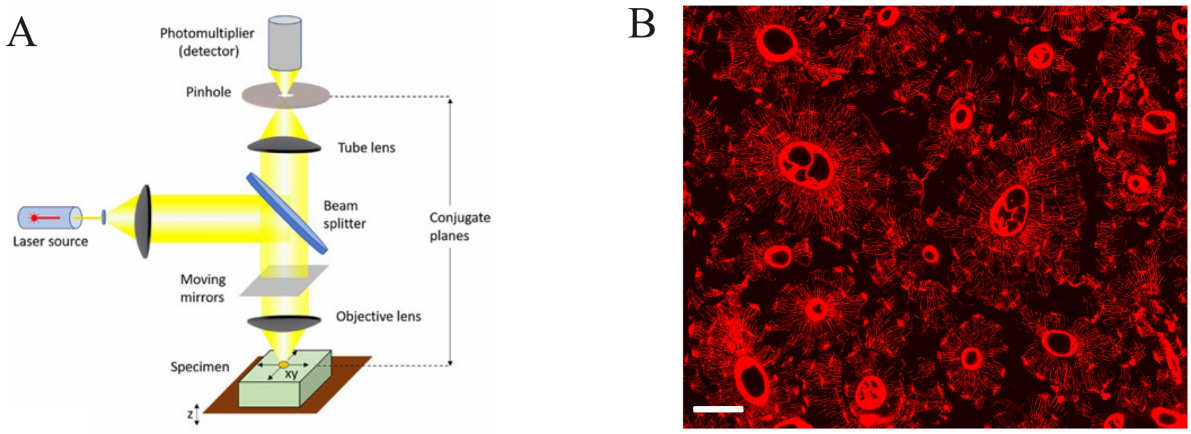


Figure 1.15: **A.** Schematic illustration of the components of the confocal laser scanning microscope. Image from (Blouin et al., 2018). **B.** Example of an image of the lacuno-canalicular network acquired using this technique (scale bar: 100 µm). Courtesy of Dr. Alexandra Tits.

D) Quantitative backscattered electron imaging

Quantitative backscattered electron imaging (qBEI) enables the bone mineral content evaluation by quantifying the distribution of calcium in a bone sample, as illustrated in Figure 1.16A-B.
This technique is based on the fact that the number of backscattered electrons (BEs) generated by an electron beam interacting with the sample depends on the local atomic number Z of the elements present on the sample surface (Hartmann et al., 2021). As calcium is a prevalent component of bone, it also

dominates the BE signal. Therefore, regions with higher calcium content produce stronger BE signals, appearing brighter in the image, while less mineralized areas appear darker, as shown in Figure 1.4B. This method provides high resolution images (sub-micrometer resolution for a penetration depth of approximately 1 µm (Tits, 2023)). qBEI allows to derive the frequency distribution of the calcium content of the sample, which was previously referred to as the BMDD (P. Roschger et al., 2008). A typical BMDD is displayed in Figure 1.16C. Unfortunately, this technique is limited to the acquisition of two-dimensional images, which requires milling the surface of the sample to collect the information from a specific depth.

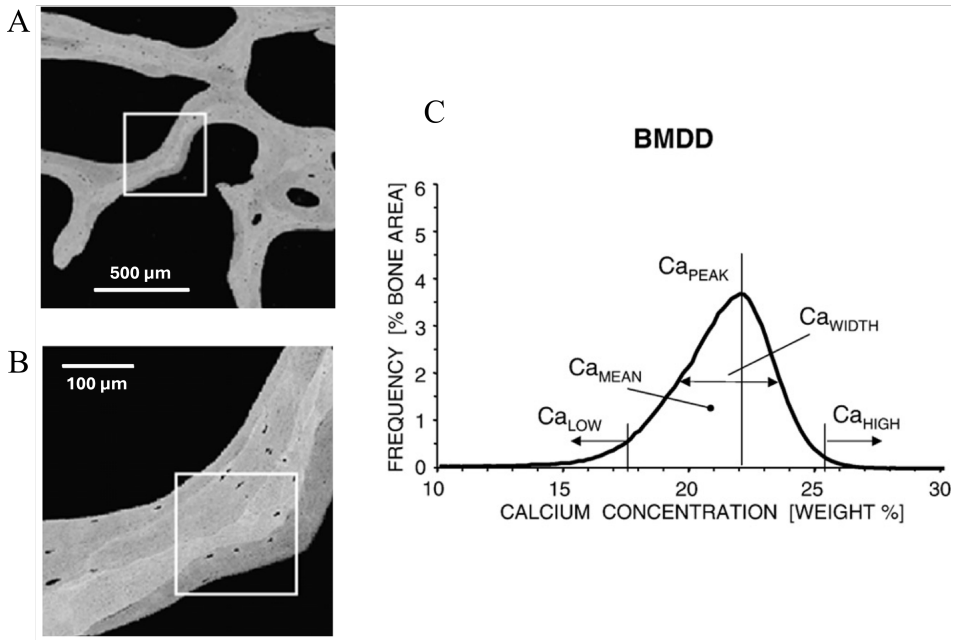


Figure 1.16: **A.** and **B.** qBEI images of trabecular bone showing the different mineralization levels of bone packets. **C.** Example of a typical bone mineral density distribution. Images adapted from (P. Roschger et al., 2008).

E) Polarized light microscopy

Light is a form of electromagnetic radiation which is composed of both an electric field and a magnetic field perpendicular to one another. Natural (or unpolarized) light is made of waves which have electric field vectors oriented in all directions. In contrast, (linearly) polarized light possesses electric field vectors that vibrate only in one direction (Oliviero and Punzi, 2022). One can go from unpolarized to polarized light using a polarizing lens, also called a polarizer. Another component, the analyzer (which is also a lens), is used to examine the light spectrum after the interaction with the sample, and therefore reconstruct the image. Polarized light is very interesting as it allows to detect birefringent materials. Birefringence is a typical optical property of anisotropic materials, that causes a light beam to split into two separate waves as it passes through, one is electric and one is magnetic (Nguyen, 2021). These waves propagate in the same direction, but perpendicular to one another and at different speeds. The analyzer then filters the rays, keeping only one, which will be picked up by the detector. This physical principle is illustrated in Figure 1.17.

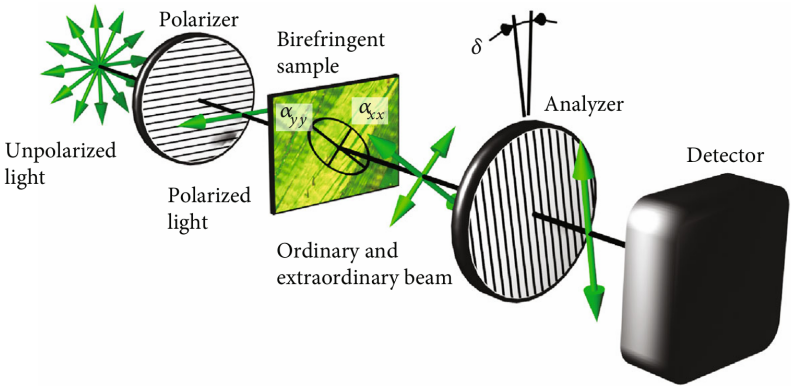


Figure 1.17: Schematized operating mechanism of polarized light microscopy and the physical principle behind. At the sample output, one of the two waves is called ordinary beam, and the other one is called the extraordinary beam. Image from (Turčanová et al., 2021).

Depending on the composition and orientation of the sample, the field vectors will have a different direction, leading to a different image. Therefore, two types of birefringence exist: intrinsic and form birefringence. While the first one is the result of the spatial arrangement of atomic groups and molecules in the sample, the second one is related to the spatial arrangement of objects (Wolman, 1975). Bone, mainly due to the collagen fibers organization, is an anisotropic and birefringent material, which explains why it can be imaged by polarized light microscopy, via form birefringence. As a recall, within the same sample, collagen fibers have the same orientation in the same (sub)lamellar unit, however, between two adjacent units, the orientation is different, although the material remains the same. Therefore, when collagen fibers are aligned perfectly transverse to the direction of the polarized light propagation, the linearly polarized light is split in two - in other words, refracted by the specimen - resulting in maximum brightness. When collagen fibers are, instead, aligned along the axis of light propagation, there is no refraction, and the fibers appear dark. Finally, collagen fibers oriented in other directions lead to intermediate brightness values (Bromage et al., 2003).

As mentioned before, along with the SEM method, polarized light microscopy allowed to reconsider the fact that one lamella is composed of a single layer of collagen fibers which have a common and unique orientation, as displayed in Figure 1.7B (Pazzaglia et al., 2012). In addition, polarized light microscopy has been used to further investigate how collagen fibers are oriented within osteon lamellae (Mitchell and Van Heteren, 2016; Bromage et al., 2003). As Figure 1.18 shows, depending on the resulting signals, there are multiple configurations that can be observed with polarized light microscopy:

- When the brightness alternates, forming successive dark and bright bands, it indicates an alternating pattern, as shown in Figure 1.18A. The collagen fibers of one band are parallel to the section plane, whereas the fibers of the following band are rather perpendicular to that plane. This is in line with what was referred to as the orthogonal plywood structure.
- When the brightness is more uniform, *i.e.* when all bands have the same intensity, it indicates that all the fibers of the osteon have a common orientation, which is either parallel to the section plane (if the bands are bright, as in Figure 1.18C, forming the so-called *bright osteons* (Stockhausen et al., 2021)) or perpendicular to it (if the bands are dark, as in Figure 1.18B, forming the so-called *dark osteons* (Stockhausen et al., 2021)). If the sample is rotated relative to the light source, and the bands remain dark, it would indicate that fibers are either unorganized, in the sense that they do not have a preferred orientation but rather random, or longitudinal to the section plane.

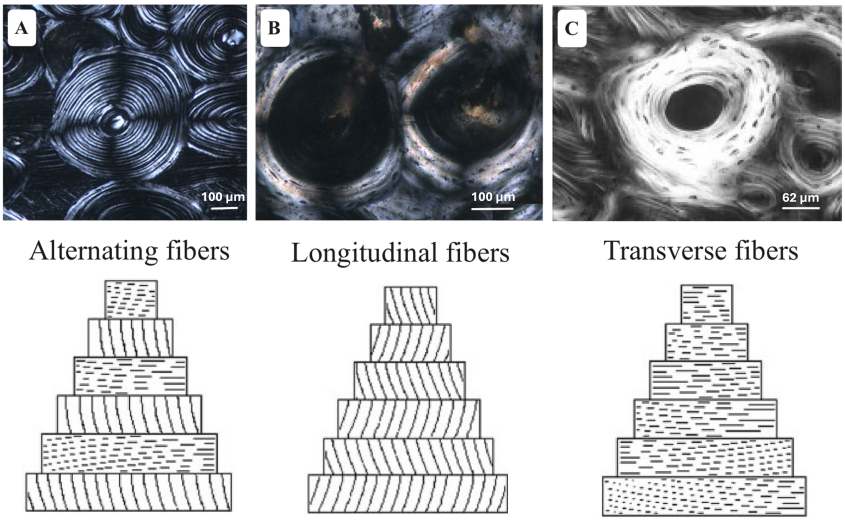


Figure 1.18: Polarized light microscopy images of lamellae within osteons. Three types of images can be observed, depending on the collagen fiber orientation. At the bottom, schematic illustrations of the collagen fibers arrangement are shown. Images adapted from (Mitchell and Van Heteren, 2016) and (Bromage et al., 2003).

Alternatively, if one considers the hypothesis that lamellae are heterogeneous, the dense lamellae correspond to the bright lamellae, whereas the loose ones correspond to the dark ones (Marotti, 1993). SEM studies term dense lamellae in lamellar bone as "inter-lamellar bone", and argue that it could be, in fact, what appears as dark lamellae in polarized light microscopy (Boyde and Riggs, 1990).

Although polarized light microscopy seems to be a great tool to assess collagen fiber orientation, it has a few limitations that must be pointed out. Indeed, the brightness level which is recorded may be affected by other factors besides the fiber orientation. Among these factors, section thickness is of particular importance. If this parameter changes, the optical path through which polarized light passes also changes, causing a different brightness, which is attributed to the thickness rather than the fiber orientation. It is thus important to have a ground uniform section thickness as a standard for the evaluation of collagen fiber orientation. Typically, a thickness of 100 ± 5 µm is taken (Boyde and Riggs, 1990; Portigliatti Barbos et al., 1984). For this reason, in the past, studies that evaluated collagen fiber orientation based on polarized light microscopy (Gebhardt, 1906) have been questioned (Boyde and Hobdell, 1968).

There remains an impressive technique that allows the evaluation of collagen fiber orientation, and which forms the basis of this work: second harmonic generation.

1.2.2 Second harmonic generation

Second harmonic generation (or SHG) is a powerful optical contrast technique which can be used in the imaging of biological structures (Campagnola and Dong, 2011). In fact, it relies on a second-order nonlinear optical process which takes place only in structures that possess a so-called non-centrosymmetry (meaning that they they do not have a center of inversion symmetry), as well as a high second-order nonlinear coefficient, meaning they can efficiently convert light into a higher frequency signal (Ambekar et al., 2012). It is a remarkable coincidence that the collagen molecule is a structure that fulfills these two requirements, which confers this optical property on it (Cox et al., 2003).

A) Physical principle

In an object, positive and negative charges exist in pairs, bound together, which makes the object electrically neutral. Under the influence of an external electric field, positive and negative charges are separated, which is a phenomenon known as polarization. Polarization results in a dipole moment; the greater the polarization strength, the greater the dipole moment. The polarization density $\mathbf{P}$ (in C/m^2)

of a material is a measure of how much an electric charge is displaced from its equilibrium position in response to the external electric field $\mathbf{E}$. The dipole moment is proportional to the polarization density (Matan, 2023).

When two light photons of the same wavelength (and therefore the same frequency) interact with an object that possesses a non-centrosymmetry, a dielectric polarization density $\mathbf{P}$ of the material is induced, due to the electric field $\mathbf{E}$ associated to light. That polarization density can be developed as a Taylor series (Repp, 2015):

$$\mathbf{P}(t) = \epsilon_0(\chi^{(1)}\mathbf{E}(t) + \chi^{(2)}\mathbf{E}^2(t) + \chi^{(3)}\mathbf{E}^3(t) + ...)$$

where $\chi^{(n)}$ is the n-th order susceptibility (which measures how much a material becomes magnetized when exposed to an external magnetic field) and ϵ_0 is the electric permittivity of vacuum. The first (linear) term

$$\mathbf{P}^{(1)} = \epsilon_0\chi^{(1)}\mathbf{E}$$

makes up for absorption, scattering and reflection of light (Cantamessa, 2025). On the other hand, the first nonlinear term

$$\mathbf{P}^{(2)} = \epsilon_0\chi^{(2)}\mathbf{E}^2$$

oscillates with twice the frequency (or half the wavelength) of the two incident photons (as illustrated in Figure 1.19). This new wave, generated by the material, is called the second harmonic. This signal has twice the energy of the two incident photons. The second-order nonlinear susceptibility $\chi^{(2)}$ of a medium characterizes its tendency to generate a second harmonic. For many materials $\chi^{(2)} \approx 0$. However, since collagen molecules do not have a center of inversion, they are associated with a non-zero value of $\chi^{(2)}$.



Figure 1.19: Schematic illustration of the physical principle behind second harmonic generation. On the right, the black wave corresponds to the first linear term, while the orange one corresponds to the nonlinear component, *i.e.* the second harmonic. To make this image, inspiration was taken from (Cantamessa, 2025) and (Tits, 2023).

B) Equipment and setup for SHG microscopy

Figure 1.20 shows a typical SHG microscopy setup (Aghigh et al., 2023). The light source is a Ti:sapphire laser which generates intense infrared light pulses at a tunable frequency. The power control module is made of two components: a half-wave plate and a polarizer. This module adjusts the power of the laser which is delivered to the microscope.

Then, the laser beam is directed towards a pair of galvanometric mirrors, which rapidly deflect the beam in both horizontal and vertical directions, directing it to a specific point of the sample. As the mirrors move, the angle of the reflected laser beam scans a new spot of the sample. Ultimately, this makes it possible to scan a complete 2D section. After scanning, the beam goes through a scan lens and a tube lens, which ensure that the focus and alignment of the beam are maintained as it enters the microscope objective.

A dichroic mirror is used to reflect the excitation light toward the sample, while allowing the generated SHG signal to pass in the opposite direction. In other words, it enables simultaneous delivery of the excitation beam and collection of the SHG signal. A high numerical aperture objective (or NA objective) focuses the laser tightly into the sample, to ensure both efficient activation and collection of the SHG signal.

The SHG signal can be collected via two paths: either in the forward direction or in the backward direction (therefore passing through the objective and then reflected by the dichroic mirror). In all cases, it is then filtered and detected by a photomultiplier tube (PMT).

A computer serves as an interface for the user in order to choose the parameters that will be used for imaging. It is also connected to all digital components that allow reconstructing the image from the PMT's and display it for analysis.

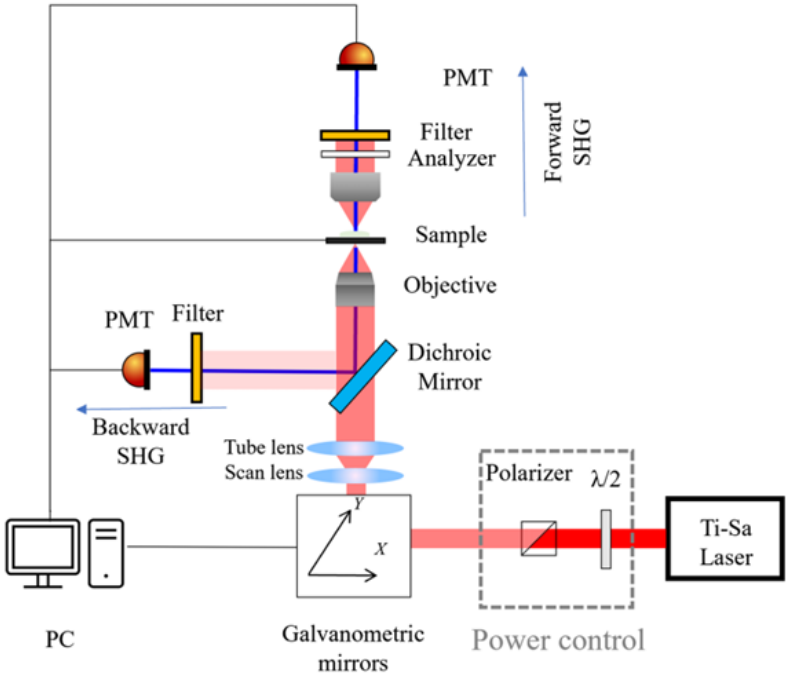


Figure 1.20: Schematic overview of a typical SHG microscopy setup. Image from (Aghigh et al., 2023).

C) SHG for assessing collagen fiber orientation

Type I and type II collagen are among the biological structures that can be imaged using second harmonic generation (SHG) microscopy (Aghigh et al., 2023; Cox, 2011). Imaging these two types of collagen is possible because the tropocollagen molecules spontaneously self-assemble to form a collagen fibril (Cox, 2011), which has an anisotropic rod-like structure. On the other hand, non-fibrillar collagen (*e.g.* type IV collagen) cannot be imaged because it forms sheets in the basal lamina (which is a thin layer of extracellular matrix secreted by epithelial cells). As type I collagen is particularly mineralized, the optical effect is even more efficient than that of type II, which is why it gives a much stronger SHG signal.

For a collagen fiber to be imaged, *i.e.* to emit a SHG signal, it must lay parallel to the imaging plane, so that the external electric field resulting from the photons is normal to that plane, as can be seen in Figure 1.21 (Ambekar et al., 2012).

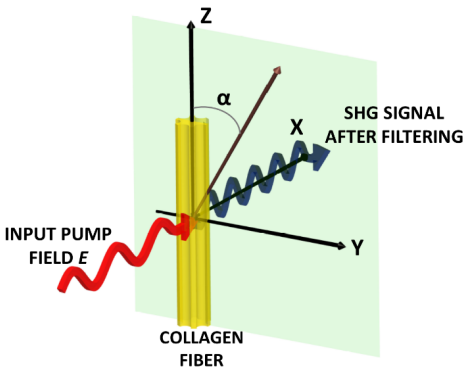


Figure 1.21: Schematic illustration of the geometric arrangement of a single collagen fiber with respect to an exerted electric field. The collagen fiber lays on the z-axis, while the electric field E is normal to the YZ-plane. Image from (Ambekar et al., 2012).

Thus, if the fiber is parallel to the incident light, no second harmonic is generated. The general principle of collagen fiber imaging is depicted in Figure 1.22. If collagen fibers are more longitudinal to the osteon, *i.e.* perpendicular to the imaging plane (or, equivalently, parallel to the incident light beam), no second harmonic is generated, and the layer of collagen fibers appear dark on the image. On the other hand, if fibers are more transverse to the osteon, *i.e.* parallel to the imaging plane (or, equivalently, perpendicular to the incident light beam), a second harmonic signal is generated by the fibers, and the layer containing these fibers appears bright on the image (Collins et al., 2020).

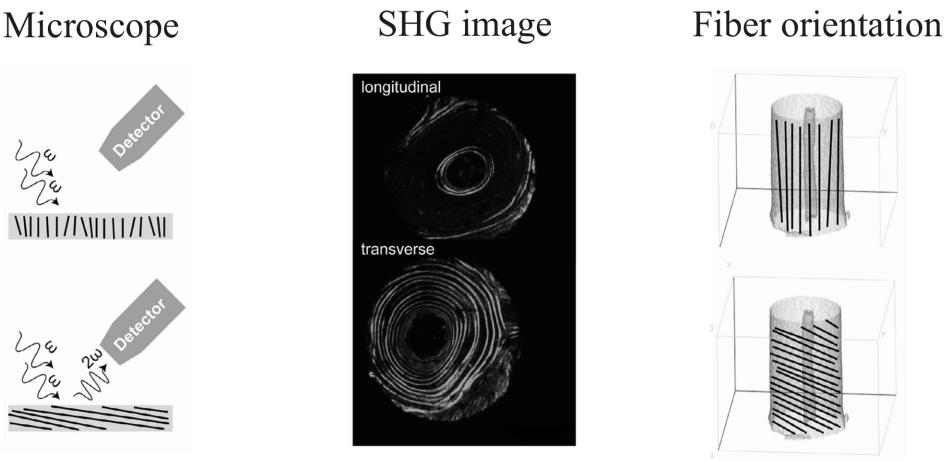


Figure 1.22: Schematic illustration of SHG microscopy and corresponding generated images along with the collagen fiber orientation. Image adapted from (Collins et al., 2020)

Figure 1.23 shows the kind of images of cortical bone that can be obtained by performing SHG. The reason why osteons appear as alternate bright and dark bands is due to the alternate change in the collagen fiber orientation. Therefore, they can be recognized as the assembly of successive bright and dark concentric "rings". In the middle of each osteon, there is a black hole which is easily identified as the Haversian canal. As can be seen, and as stated before, osteons come in various shapes.

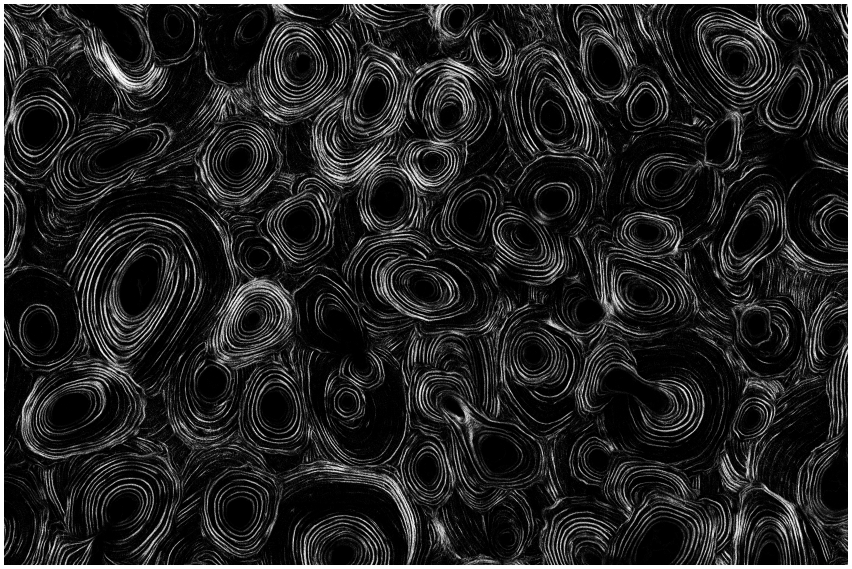


Figure 1.23: SHG image of cortical bone, courtesy of Alexandra Tits.

It is important to keep in mind that SHG images are not binary, although they might seem. Indeed, each pixel is associated with a gray-value intensity ranging from 0 (completely black) to 255 (completely white). This emphasizes that lamellae do not necessarily form an orthogonal plywood structure. In other words, a bright band does not automatically contain only collagen fibers that are perfectly parallel to the imaging plane. These fibers might be slightly tilted relative to that plane. This would suggest that intermediate gray-values could be linked with an intermediate orientation of collagen fibers, between transverse and longitudinal. Nevertheless, these in-between gray levels could also be simply due to noise, to the parameters set for the image acquisition, or to other intrinsic optical properties of the structure, which are discussed in greater detail later in this report.

D) Advantages and drawbacks of SHG

SHG is extremely powerful and presents many advantages. The following paragraphs summarize the main ones.

First and foremost, SHG microscopy provides imaging with superior resolution at the submicron scale, outperforming polarized light microscopy. As illustrated in Figure 1.23, it produces sharp-contrast images (Houle et al., 2015).

Moreover, unlike many other methods, including two-photon excited fluorescence (or TPF, which is another nonlinear optical technique), SHG microscopy does not rely on the presence of fluorescent dyes or staining (Gauderon et al., 2001), but rather simply on the endogenous contrast of the sample. This means that the signal is not likely to decay over time (which is referred to as photobleaching). Furthermore, it occurs instantaneously, as the second harmonic is generated as soon as the light beam hits the sample (Aghigh et al., 2023; Hoover and Squier, 2013).

Finally, conventional linear optic microscopes are subject to scattering and absorption effects, which restrict imaging to the surface only and prevent optical slicing in thick and complex samples (Helmchen and Denk, 2005). SHG overcomes these limitations, allowing deeper penetration through the specimen (up to approximately 50 microns), thereby enabling the scanning of specific depths within the sample (Aghigh et al., 2023).

However, despite these benefits, one should also acknowledge some drawbacks associated with SHG.

On the one hand, SHG requires a large input intensity of the light beam to induce a detectable second harmonic signal, which may pose a risk of photodamage, particularly in delicate biological specimens.

On the other hand, the mechanisms behind SHG are so complex that the signal does not depend only on the collagen fiber orientation with respect to the imaging plane. Indeed, it is also affected by other factors, including the packing density and the degree of alignment of collagen fibrils (Genthial et al., 2017), as well as their diameter (LaComb et al., 2008) and the amount of collagen cross-linking (Lutz et al., 2012). Another influencing parameter which is independent from the sample is the polarization of the incident light (Repp, 2015). Therefore, it becomes difficult to interpret the signal with confidence. Indeed, it is not easy to assess whether a bright signal corresponds to collagen fibers that are parallel to the image plane, or whether it is simply the result of a very dense layer of fibers, a layer made up of fibers with a large diameter, or a layer composed of highly aligned, and therefore well-ordered, collagen fibers. Similarly, a dark signal could very well correspond to disorganized collagen fibers, fibers with a smaller diameter, or simply a layer with lower fiber density. This ties into the idea that several models can be used to describe how collagen fibers are organized within the lamellae. As a reminder, some hypotheses suggest that the difference between two successive lamellar units lies not in the orientation of the collagen fibers, but rather in their composition — particularly in terms of fibrillar packing density.

In the context of this work, we simply consider that a bright band corresponds to a layer made up of collagen fibers that are, for the most part, laying in the image plane, (*i.e.* perpendicular to the incident beam), while the opposite holds for dark layers.

1.3 Main aims of the thesis

The concept of bone quality is of major clinical importance. A bone qualified as being of "good quality" possesses characteristics (whether intrinsic, architectural, or mechanical) that allow it to minimize, as much as possible, the risk of fracture. It is well known that some diseases, such as osteoporosis, tend to reduce bone quality by increasing the risk of bone fracture (Kanis, 2002). Therefore, in order to understand what makes a bone of "good quality," it is important to evaluate, one by one, the various aspects that are closely linked to the concept of bone quality. As previously mentioned, four main factors underlie bone quality: composition, structure, microarchitecture and remodeling. In the research field, particular attention is often given to bone composition, in spite of the other aspects (Burr, n.d.). Indeed, fracture risk is often assessed solely based on bone mineral density (BMD) although it has already been pointed out, for example, that the fracture risk of a 75-year-old woman is 4 to 7 times higher than that of a 45-year-old woman, despite having the same bone mineral density (Burr, n.d.). This is explained by the fact that BMD only accounts for 80 to 90% of bone strength (Mazess, 1982). Among the remaining fraction is the contribution of microarchitecture, which remains relatively underexplored.

By understanding how bone is organized at the micrometer scale, one gains additional tools to assess bone quality. Certainly, bone structure has been described many times at this scale using a variety of techniques and mathematical models. However, there is still room for new discoveries. This is the purpose of this thesis: to offer a new description of cortical bone at the micrometer scale. Based on SHG images of osteons acquired along the depth of a bone sample, the goal is to extract new information about the morphology of lamellae, information that has been poorly investigated in the past, and to simplify this information by transforming the osteon into a mathematical object that is easy to handle and interpret.

This thesis is organized into two main parts. The first aims to investigate and characterize the morphology of osteons based on raw SHG images. More specifically, it focuses on understanding how bright lamellae are spatially arranged within the osteon.

The second part focuses on reconstructing an osteon as a mathematical object. This involves creating a geometrical model to simplify the complexity of the osteon and enable its characterization. Indeed, when the real world appears complex, engineers aim to simplify it, to abstract away complicated aspects, and to reduce them into a representation that can be more easily interpreted and further manipulated.

Chapter 2

Experimental part

This brief chapter outlines the experimental protocol that was conducted to collect the SHG images which form the basis of this work.

Sample preparation and sample imaging were performed by Dr. Alexandra Tits and Dr. Maximiliam Rummler, two post-doctoral researchers, in the Max Planck Institute of Colloids and Interfaces, in Golm (Germany). Nevertheless, both procedures are highly relevant in the context of this project and are therefore described in this chapter to ensure clarity for the reader.

2.1 Sample preparation

A bone necropsy was extracted from the femur midshaft of a 56-year-old woman without any bone-related condition. The bone sample was provided by the Department of Anatomy of the Medical University of Vienna. Immediately after extraction, the bone was frozen and preserved at -20°C. Following defrosting, soft tissue was removed, and a 1 cm-thick piece of the diaphysis was cut perpendicularly to the long axis of the femur. The lateral portion of this piece was specifically selected for subsequent analysis.

Figure 2.1 shows how the sample looks like, once the successive steps described below are applied to the specimen for its preparation. First, the sample was dehydrated using ethanol. It was then immersed in diethylene glycol, notably to prevent water exposure. After that, the sample was stained using rhodamine-6G in ethanol (0.02%wt), hence its red appearance. In the context of this work, this is not particularly relevant; it is simply important to note that the same sample was imaged using confocal imaging in order to visualize the lacunocanalicular network. As mentioned in the previous chapter, this technique requires staining the biological tissue with a fluorescent dye. In order to optimize the quality of the images acquired by CLSM, the sample was embedded in polymethylmethacrylate (PMMA), a polymer resin which provides the specimen with a smooth surface. Finally, the embedded sample was sectioned to obtain parallel surfaces, sanded with a succession of different grades of abrasive paper, and ultimately polished using diamond powder (van Tol et al., 2020).

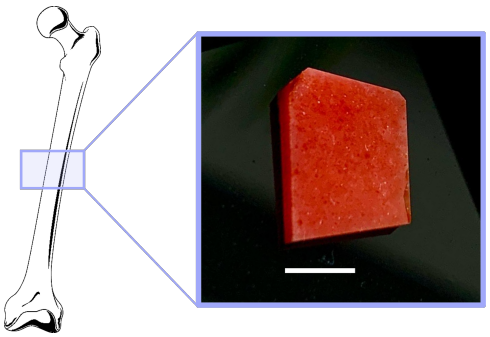


Figure 2.1: Picture of the sample from which the SHG images have been acquired (scale bar: 4 mm). The specimen was extracted from the midshaft of a human femur. Image on the left is from Servier Medical Art, image on the right is courtesy of Dr. Alexandra Tits.

First, a glass holder intended for the sample is disinfected using an AHD 1000 alcohol-based solution. A few drops of ethylene glycol are then applied to the glass surface. This liquid prevents the formation of air gaps between the sample and the glass. It is worth noting that ethylene glycol and glass share the same refractive index, allowing the incident light beam to pass through smoothly and without significant reflection.

The drops of ethylene glycol merge to form a single large droplet, into which the sample can be meticulously placed. To avoid the formation of trapping air bubbles, the sample can be introduced from the edge of the droplet, rather than from the top. It is essential to ensure consistent sample orientation during imaging (to avoid imaging different objects), *i.e.*, to have a reliable reference. In this case, the side of the sample that must face upwards can be easily identified, as it is coated with a small amount of glue. Moreover, the sample is positioned so that the most visibly trimmed (or cut) corner is at the top left.

2.2 Second harmonic imaging

Once the sample is prepared, the glass holder is placed inside the Leica TCS SP8 confocal microscope (Wetzlar, Germany). To ensure that the laser beam travels through a continuous medium, a large drop of immersion oil is applied to the objective lens (HC PL APO CS2 40x/1.30 OIL) located beneath the sample. The final setup is illustrated in Figure 2.2.

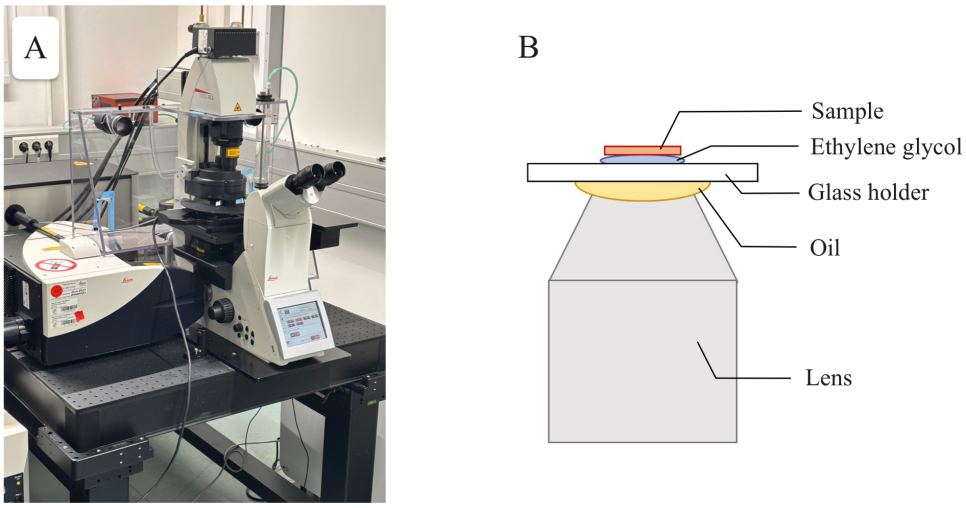


Figure 2.2: Experimental setup for the sample imaging. **A.** Real picture. **B.** Schematic representation. Courtesy of Dr. Alexandra Tits.

The user interacts with the Leica software to adjust the various settings for SHG imaging and to visualize the scan. The wavelength of the multi-photon laser (Mai-Tai high performance Ti:Sa Laser, Spectra-Physics, Milpitas, CA, USA) used to excite the sample was set to 910 nm, with an output power of 0.056 W - which represents 10% of the maximum power delivered to the microscope. A HyD SMD detector was used, with a detection spectral window defined between 450 and 460 nm, to ensure capturing half of the excitation wavelength (namely 455 nm).

Unlike micro-CT, SHG imaging does not require the use of a pinhole. Consequently, the pinhole was fully opened to maximize signal collection, leading to a nominal isotropic pixel size of 379 nm.

Once the setup is complete, imaging can begin. When the cortical bone is scanned, one can observe the type of image illustrated in Figure 1.23. A zoom-in can then be performed to isolate and capture a single osteon. With a zoom factor of 0.75, the osteon is imaged within a field of view of 1024 pixels $\times$ 1024 pixels. Each pixel corresponds to a resolution of 379 nm (*i.e.*, 0.379 µm) in both the horizontal and vertical directions of the image plane. This means that the image has a size of 388.096 µm by 388.096 µm.

As previously mentioned, SHG microscopy enables optical sectioning, allowing the visualization of structures in depth by selectively exciting a specific plane within the sample. In this case, each osteon was imaged over a depth of approximately 50 µm, beyond which the signal becomes too weak to be

detected. At the end, each image stack consists of 136 slices, each measuring 1024 × 1024 pixels. The spatial resolution is 0.379 µm along the x-axis (horizontal), 0.379 µm along the y-axis (vertical), and 0.4 µm along the depth (z-axis). Figure 2.3 shows a visual representation of the acquired stack of images.

Among all osteons contained within the cortical bone of the sample, approximately ten were isolated. From this subset, three were specifically selected for use in the context of this work. These osteons were selected based on the following two criteria:

- their shape should be as circular as possible; in other words, they should not exhibit an elliptical or irregular geometry;
- their Haversian canal should be relatively centered within the osteon (*i.e.*, not located near one side of the reversal line) and, most importantly, it should remain stable across slices, showing minimal displacement within the image plane. In other words, over the scanned depth, the osteon should remain approximately perpendicular to the surface of the sample.

These selection conditions were adopted mainly to simplify the subsequent analysis. Given that the methods introduced in this study are quite new, it is reasonable that they be initially applied to relatively simple cases to avoid immediately dealing with more complex situations that would require a deeper and more advanced approach.

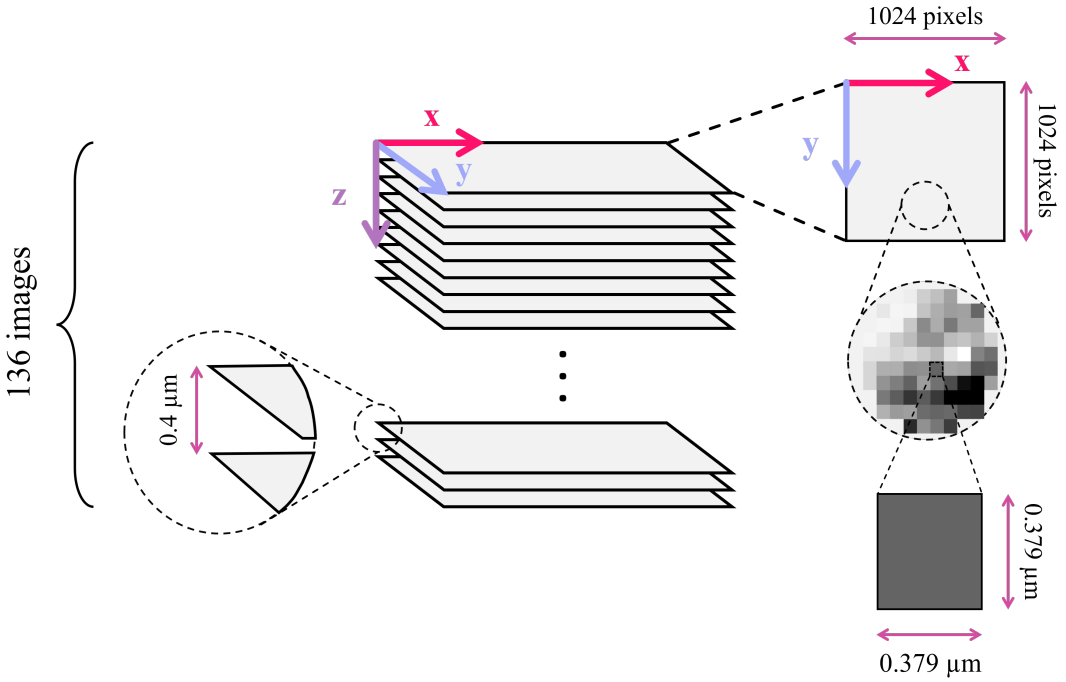


Figure 2.3: Illustrative diagram showing the format of the images acquired from the osteons.

The images in Figure 2.4 indicate the positions of the three osteons of interest within the cortical bone, while Figure 2.5 includes the three isolated osteons (*i.e.*, the 1024×1024-sized images) to which the methods described in this work are applied. From here on, they will be referred to as osteon no. 1, osteon no. 2, and osteon no. 3, respectively. In this Figure, slice 68 is shown in each case, which is the middle slice of the 136-image stack.

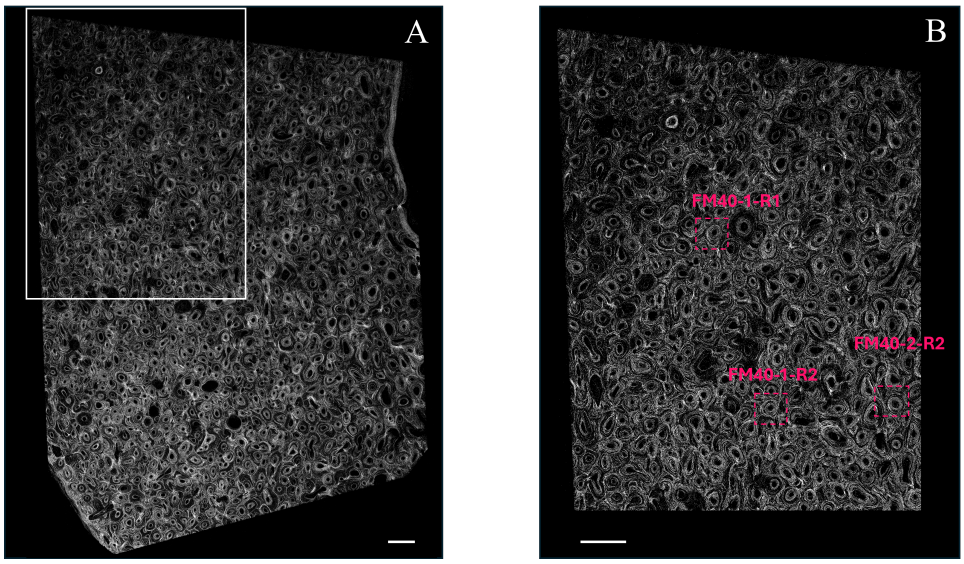


Figure 2.4: Image showing where the three osteons of interest are located within the imaged cortical bone. **A.** SHG image of the entire sample. **B.** Magnification of the white rectangular box in **A.**, showing the location of the three analyzed osteons. Scale bars: 500 µm Courtesy of Dr. Alexandra Tits.

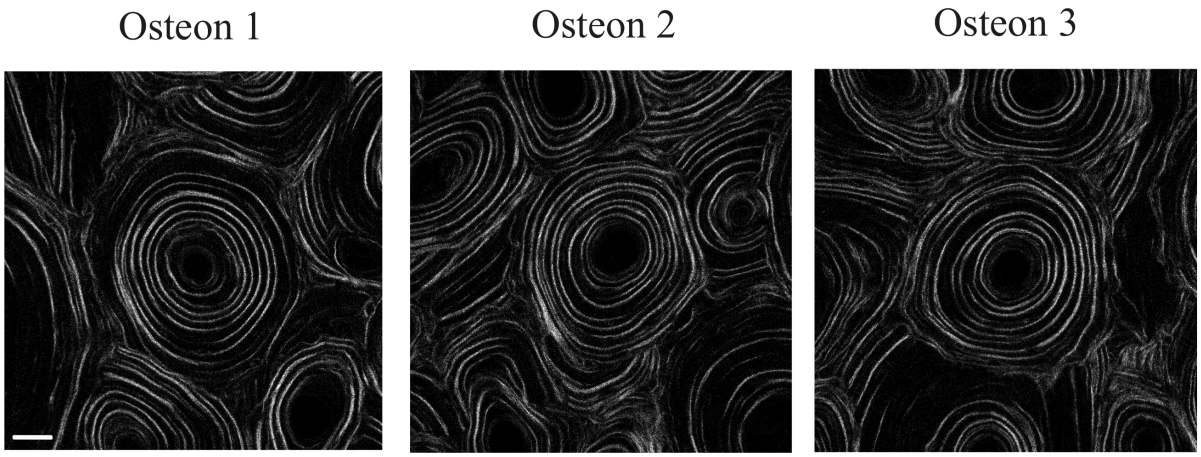


Figure 2.5: The three osteons of interest, analyzed as part of this work. Scale bar: 40 µm.

As previously explained, each pixel contains a grayscale value that ranges between 0 and 255. This value presumably reflects the orientation of the collagen fibers. A high value (and thus a relatively bright pixel) is assumed to be associated with a longitudinal fiber orientation in the plane of the image, whereas a low grayscale value (and thus a relatively dark pixel) would be associated with a different orientation.

Chapter 3

Structural analysis of lamellae

3.1 Introduction

This first part of the project aims to describe the organization of lamellae within osteons. It differs from the second part mainly because the results are extracted solely based on raw images, that is, unprocessed images. Since the construction of a mathematical model is not the objective at this stage, there is no need to modify the images. It will become apparent, however, that this will prove necessary when the objective is to simplify the osteon, in order to reduce it to a mathematical object (which is, in fact, the focus of the second part of the project). Here, on the other hand, the objective is to understand how the bright rings, let them be called as such, visible in the SHG images of osteons (see Figure 2.5), are arranged in space. Obviously, altering the images is not desirable, in order to preserve the information and the signal as they were acquired. In other words, there is no reason to simplify reality.

To carry out this study, two well-known image analysis software were used: Dragonfly and Fiji (also called ImageJ). In addition, all quantitative evaluations of the lamellar morphology were carried out using Python-written programs.

The goal of this first part is to investigate the morphology of the lamellae in the longitudinal plane of the osteon, and the link with the characteristics of the transverse plane.

Before presenting these results, the chapter first introduces the binarization of the images through segmentation. Then, the reslicing of the osteon will be explained, which will enable the transition from the transverse plane to the longitudinal plane. Finally, the various quantitative features of interest will be detailed.

3.2 Simplifying hypothesis

When the use of SHG microscopy for the evaluation of collagen fiber orientation was introduced (see Subsection 1.2.2 C), it was pointed out that, due to the dependence of the signal on factors other than orientation (particularly the packing density of the fibers (Genthial et al., 2017)) it was difficult to interpret the signal with confidence. Moreover, all the models introduced in the literature regarding the organization of the lamellae (see Subsection 1.1.4 D) do not make things easier.

It is therefore appropriate to make a choice and clearly define what is referred to as a lamella. One could, for instance, assume that the alternating bright and dark bands observed in SHG images form an orthogonal plywood structure. In other words, there is a succession of bright bands, containing fibers perfectly longitudinal to the image plane, and dark bands, containing fibers perfectly transverse to the image plane. This would then imply that no intermediate orientations are considered. A lamella would, in that case, be defined by a single band, regardless of its brightness. A schematic visualization of this configuration can be seen in Figure 3.1A.

Alternatively, one could consider a model of a twisted plywood structure, in which the orientation of the fibers changes continuously and in a monotonic direction (either clockwise or counterclockwise, but not both). In the image, a lamella would then be defined as the region between two consecutive SHG signal peaks (that is, between the midlines of two successive bright bands). Between the two peaks, the fiber orientation changes gradually (forming what were referred to as sub-lamellae), with the signal decreasing progressively until it becomes dark (in the midline of a dark band), where the fibers are purely transverse to the image plane. A schematic visualization of this configuration can be seen in Figure 3.1B.

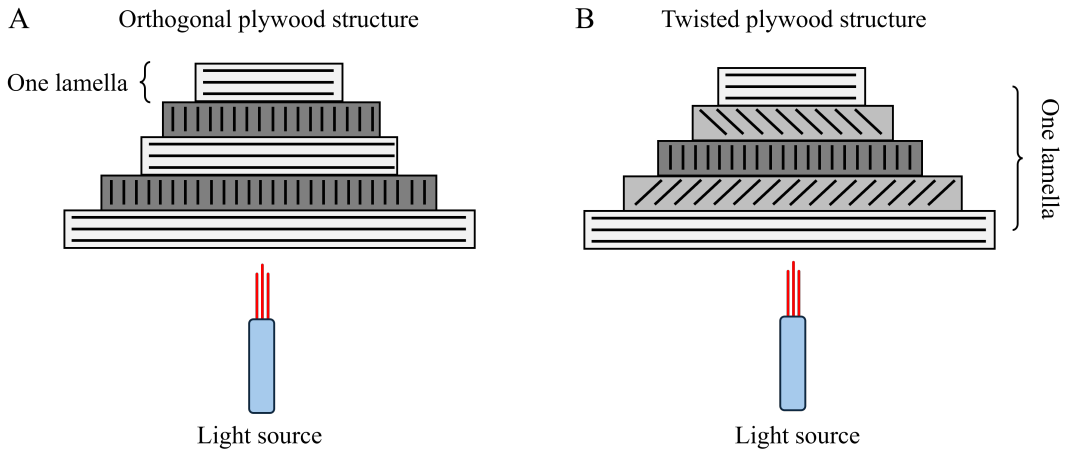


Figure 3.1: Schematic illustration of how lamellar layers appear under the SHG microscopy, depending on the configurational model. **A.** Orthogonal plywood structure. **B.** Twisted plywood structure. Layers appear dark when the fibers they contain are parallel to the light beam, bright if they are perpendicular to it, and of intermediate gray scale if otherwise.

However, none of these assumptions - both of which are far too strong - is adopted. In order to avoid over-interpreting the images, it is simply considered that a lamella corresponds to a bright band, that is, where a SHG signal is measured. Within such a lamella, the collagen fibers are more or less longitudinal to the image plane. As for the dark bands, which lie between each pair of bright bands, no particular characterization is assigned to them. They certainly contain collagen fibers, but it will simply be assumed that their orientation is not close to the longitudinal axis of the image plane.

For this reason - and for the sake of simplicity - what will be referred to as "lamellae" in the context of this work are in fact only periodic bright patterns that appear in the SHG images.

3.3 Image segmentation

The process of segmentation, in image processing, consists in dividing an image into different meaningful regions or objects. The objective is to isolate the relevant parts of the image, such as biological structures, objects, or regions of interest, from each other. Each entity is then assigned to a class. A priori, there is no limit to the number of classes that can be defined. In the context of this work, we will limit ourselves to two groups: the bright bands and the dark bands. In the end, the segmentation is reduced to a simple binarization of the image: the pixels considered as belonging to a bright band become white, and those belonging to a dark band become black.

In principle, the segmentation of osteons is not directly part of this first section of the project. As explained previously, the work will be carried out on raw images. However, it is necessary to introduce this binarization operation already at this stage, as it will be used in the initial phase. Further explanations will be provided in due course.

A) Image post-processing

Before performing the segmentation, it seems appropriate to slightly modify the SHG images of the osteons in order to increase the contrast between the bright and dark regions. Indeed, since the binarization will be carried out using a Deep Learning model, based on a number of images that were manually binarized beforehand, it is important to make the task easier for both the person responsible for the manual segmentation and the model that will be trained. In short, the post-processing of the acquired images aims to improve their interpretability at the pixel level.

First, the osteons were cropped in order to isolate them from neighboring osteons and interstitial lamellae. Their images can be seen in Figure 3.2.

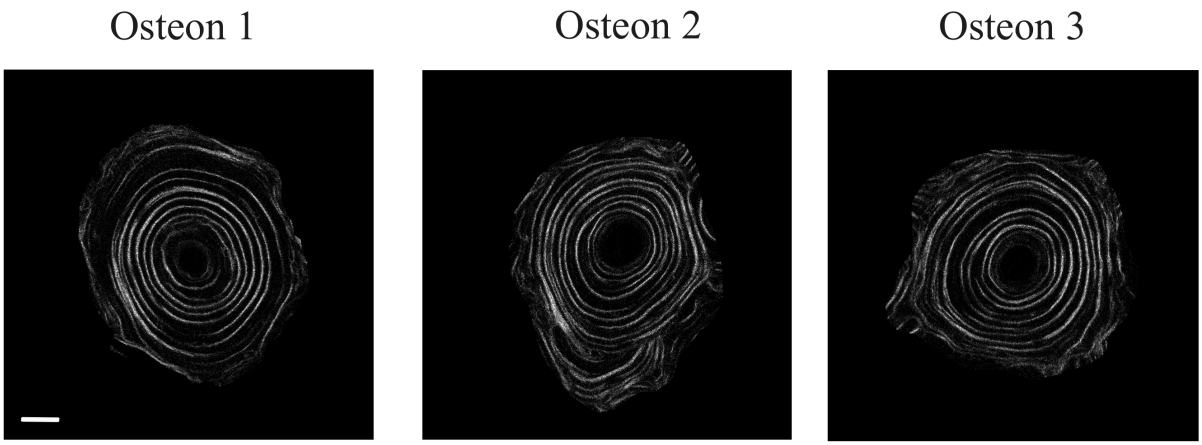


Figure 3.2: Cropped osteons. Scale bar: 40 µm.

Among all the image filtering operations available on Dragonfly, only one proved to be of interest, it is the **CLAHE** (Contrast Limited Adaptive Histogram Equalization) algorithm.

The graph that displays the frequency of the pixel intensities contained in an image is called an intensity histogram (or simply image histogram). **Histogram equalization** (H.E.) is a technique that stretches the image histogram to expand the information, thereby covering all values from 0 to 255.

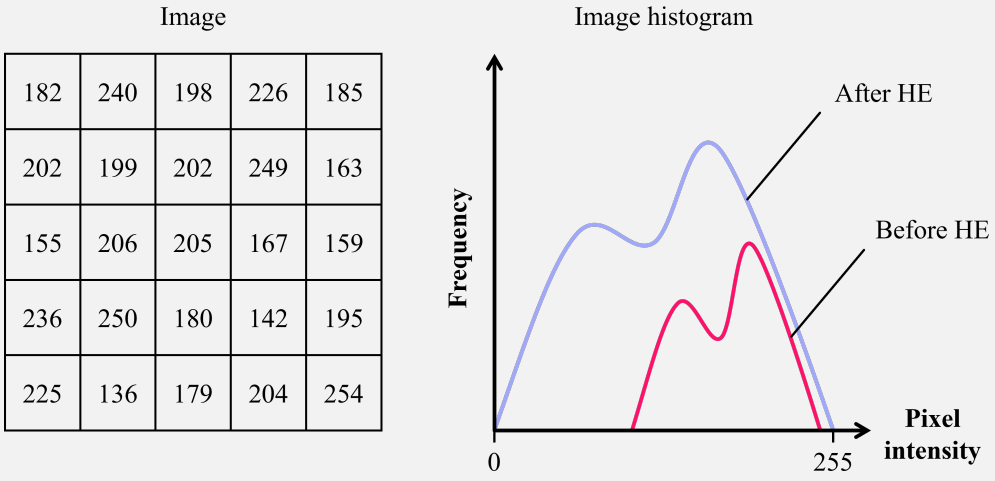


Figure 3.3: Principle of histogram equalization.

The issue with this method is that it leads to regions that are either too bright or too dark, since the pixel intensity is forced to tend towards 0 or 255, respectively.

As a solution, **adaptive histogram equalization** (A.H.E.) operates locally. This algorithm divides the pixels of an image into groups, called tiles, and performs histogram equalization on each tile.

Finally, to prevent the amplification of potential noise present in the image, the contrast is limited below a specific value, hence the name of the algorithm: **contrast limited adaptive histogram equalization** (CLAHE).

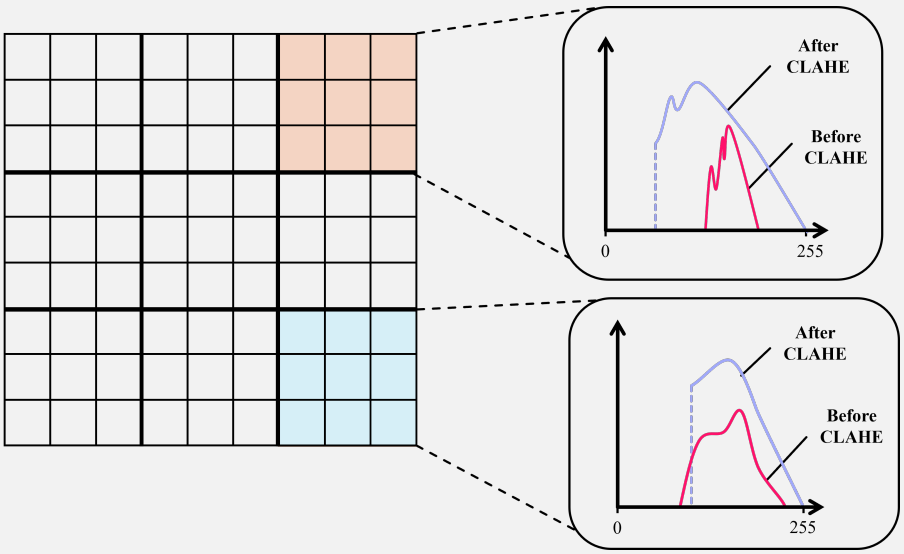


Figure 3.4: Principle of contrast limited adaptive histogram equalization.

This technique relies on three adjustable parameters:

- *Clip* defines the threshold used to limit contrast enhancement. Its value typically ranges from 0 to 4. A value of 0 implies minimal contrast limitation, thereby allowing strong contrast.
- *Kernel size* specifies the dimensions of the tiles (in pixels) on which local histogram is equalized. If set to n, each tile will have dimensions of $n \times n$ pixels.
- *Bins* refers to the number of gray levels used to construct the histogram, and can be set between 2 and 256.

Following an exploration of various parameter combinations, and proceeding by a trial-and-error approach, the values reported in Table 1 were selected.

Parameter	Value
Clip	0.01
Kernel size	8
Bins	100

Table 1: Selected parameters for the CLAHE algorithm

The resulting images were then processed on Fiji. Only the **background subtraction filter** was used. It is a technique complementary to the CLAHE algorithm, which allows to correct the shading of an image, thus improving the contrast. Following an empirical approach, the only adjustable parameter, namely the rolling ball radius, was set to 8 pixels.

Background subtraction is the process of distinguishing the "foreground" from the "background", eventually keeping only the foreground. For the images considered in this study, the background can be seen as the weak signal, potentially associated with noise. Several algorithms can be used, but Fiji uses a filter called the **rolling ball algorithm**.

To understand this algorithm, the image can be represented as a three-dimensional surface, where the height at each point corresponds to the intensity of the associated pixel. To estimate the background, one can imagine a ball of a given radius (called the ball radius, which is measured in pixels) rising from beneath this surface, as illustrated in Figure 3.5. Its center is aligned vertically with the pixel of interest. The ball is then raised until it touches the surface without penetrating it; the height reached by the top of the ball corresponds to the estimated background value for that pixel. Repetition of this process for every pixel — as if the ball was rolling underneath the entire surface — allows a complete estimation of the background. Finally, the processed image is obtained by subtracting the background from the initial input.

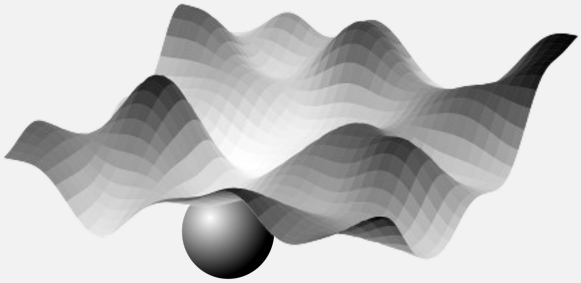


Figure 3.5: Principle of the rolling ball algorithm.

B) Image binarization

To carry out the segmentation of the processed images, a Deep Learning model based on a U-Net was used. This model is already implemented in the Dragonfly software, and is simply meant to be used by the user. Briefly, once the image stack is loaded, the user is required to perform a manual segmentation of the bands in multiple selected frames (in this work, five frames were used). As mentioned before, segmentation is performed into two classes: dark bands and bright bands. The regions selected for manual segmentation are diverse in terms of complexity. Here, two windows with easily distinguishable bands were selected. On the other hand, the other windows included bands where segmentation was more challenging, with the aim of enabling the model to handle a variety of scenarios and thereby optimize the binarization process. Based on these frames, a U-Net model is trained. The training was performed on the images of osteon no. 2. Finally, this model is applied to all the slices of the stack to get the binarized version of all three osteons.

3.4 Osteon centering

In order to ensure correct reslicing, the osteons must be centered so that the center of the Haversian canal coincides with the center of the image. It is this step of the first part of the project that requires the use of the binary images of the osteon.

It is important to note that the SHG signal appears relatively weak in the initial slices of the image stack, as the surface of the sample has not yet been reached. A similar decrease in signal intensity is observed at greater depths, as one approaches 50 µm, as it becomes harder to excite the tissue section, which leads to reduced SHG signal generation. For this reason, the initial and final slices of the binarized image stack were excluded from the image sequence, after a visual inspection. Only the slices in which the osteon was clearly visible were retained. Here are the selected slices for each osteon:

- Osteon 1: from slice 8 to slice 121 (out of 136)
- Osteon 2: from slice 8 to slice 125 (out of 136)
- Osteon 3: from slice 11 to slice 116 (out of 136)

The selected slices are not identical across the three osteons, as the starting position of the z-stack is manually - and thus arbitrarily - chosen by the user before proceeding to the sample imaging throughout its depth. Consequently, since the selected position varies from one osteon to another, it is expected that the corresponding retained slices are different.

Then, for each osteon, the first clearly visible bright band closest to the Haversian canal — defined as a continuous, uninterrupted ring that is easily distinguishable from adjacent bands — was manually isolated using Fiji. Let n be the number of retained slices. This operation, aimed at isolating the first clearly visible ring, was repeated on slices number 1, $\frac{n}{2}$, n, $\frac{n}{4}$ and $\frac{3n}{4}$ — corresponding to the first, middle, last, and two intermediate slices, respectively. Otherwise, segmenting the rings throughout the entire stack would be too time consuming.

An example of an isolated ring is shown in Figure 3.6.

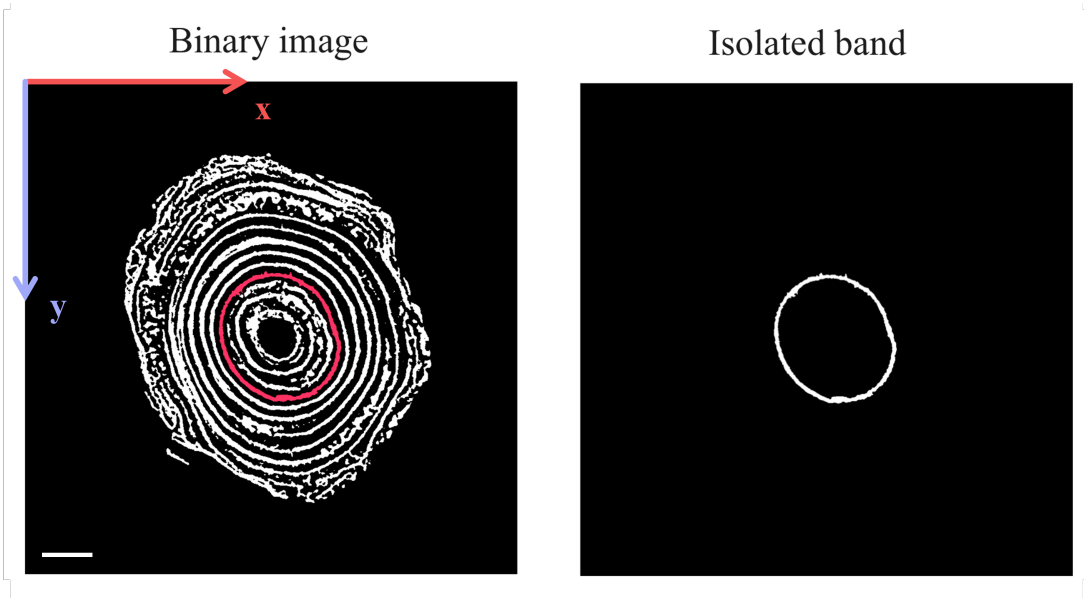


Figure 3.6: Binarized image of osteon 1 (slice 64 out of 136) on the left, with the first clearly visible bright band highlighted in red. The isolated band is shown on the right. Scale bar: 40 µm.

Based on such a binary ring, the center of mass of the osteon can be estimated. It was hypothesized that, at a given slice, the center of mass of the first clearly distinguishable bright band, closest to the Haversian canal, provides an approximation of the center of mass of the canal itself, and therefore of the entire Haversian system.

To center the osteon, it is sufficient to translate its center of mass so that it coincides with the center of the image, located at position (512, 512) - in pixels - for all values of z, given the image dimensions (1024×1024 pixels). However, since the Haversian canal is not perfectly perpendicular to the imaging plane, the osteon center of mass is varying throughout the depth. For such a reason, and to ensure an identical translation for all slices within a stack, it is more appropriate to define a global center of mass for the osteon. If (x_i, y_i, z_i) denotes the position, in space, of the center of mass of the first clearly visible ring at slice number i (out of n slices), then the global center of mass of the Haversian system is

given by the point with the following coordinates:

$$(x_{COM,osteon};\ y_{COM,osteon};\ z) = \left(\frac{1}{5}\sum_i x_i\ ;\ \frac{1}{5}\sum_i y_i\ ;\ z\right) \forall z, \quad \text{for } i \in \{1, \frac{n}{4}, \frac{n}{2}, \frac{3n}{4}, n\}$$

In other words, each coordinate, except for the depth z, is computed as the average of the respective coordinate of the center of mass of the first clearly visible ring, computed over the five slices in which this ring was segmented.

Finally, translating the osteon within each slice is equivalent to applying an affine transformation to the SHG signal within that cross-section, using the following transformation matrix:

$$T = \begin{bmatrix} 1 & 0 & (512 - x_{COM,osteon}) \\ 0 & 1 & (512 - y_{COM,osteon}) \end{bmatrix}$$

3.5 Osteon reslicing

The reslicing of a 2D image sequence is an operation that consists in reconstructing a section along a plane different from the acquisition plane. In this case, the acquisition plane is parallel to the XY-plane. Consequently, the reslicing aims to extract sections in the XZ or YZ-plane, similar to a cake being cut with a knife to reveal its composition in the cutting plane. This process allows visualization of the lamellar structure from a perspective different from that of the initially acquired SHG images. This is particularly useful and interesting given the geometry of the osteons - made up of concentric lamellae. It is important to note that if each osteon had been imaged directly along these new planes, the resulting images would appear very different from the reslices, due to the change in the orientation of collagen fibers relative to the light source.

Figure 3.7A illustrates a conceptual diagram of the reslicing (according to the blue section). The window on the right displays the resulting section (*i.e.* the reslice), which allows the content of the osteon, *i.e.* the lamellae, to be visualized in the longitudinal plane.

The osteon can also be rotated within the acquisition plane (*i.e.*, the XY-plane), while maintaining the same reslicing plane (that is the blue plane illustrated in Figure 3.7A). This process would be equivalent to performing a reslicing along an arbitrary plane (as long as it is parallel to the z-axis and goes through the center of the image stack), allowing the lamellae to be visualized in this specific longitudinal section of the osteon.

It is now relevant to highlight the importance of centering the osteon with respect to the center of the acquisition plane. To ensure that the lamellae which appear in different reslicing planes remain comparable, the line parallel to the z-axis that passes through the middle of the reslicing plane must closely follow the trajectory of the Haversian canal's center throughout the depth of the osteon — regardless of the rotation applied.

For this reason, the center of the Haversian system was aligned with the point located in (512, 512) in the image plane (the coordinates are expressed in pixels). Thus, the reslicing plane is parallel to the XZ-plane and can be defined at $y = 512$ pixels. Note that the format of the slices remains unchanged, and so is the coordinate system. Only the osteon (that is, the nonzero pixels) undergoes rotation.

Figure 3.7B shows the same concept as Figure 3.7A, but with a rotated osteon.

Reslicing was performed by rotating the osteon every 30°. As a result, for each of the three osteons, six reslices are obtained, one for each of the following rotation angles: 0°, 30°, 60°, 90°, 120°, and 150°. A rotation of 180° would simply yield a mirror image of the original reslice, due to orthogonal symmetry.

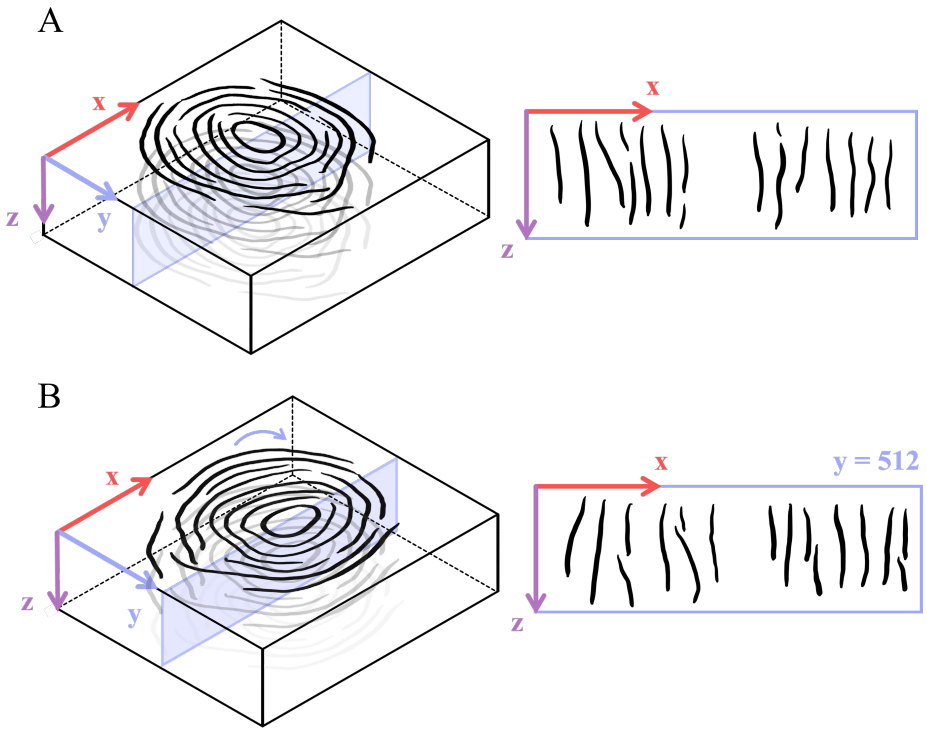


Figure 3.7: **A.** Schematic visualization of how reslicing works (on the left) and corresponding reslice (on the right). The dark lines correspond to lamellae seen in the longitudinal plane, which appear as concentric rings in the transverse plane. **B.** Same principle, except the osteon has been rotated around its global center of mass.

3.6 Linear regression fit

One way to quantitatively characterize lamellae is to represent them as mathematical objects. In the longitudinal plane of the osteon, that has been obtained thanks to reslicing, the lamellae appear as nearly straight lines, making it reasonable to approximate them with linear segments. To this end, weighted linear regressions were fitted to each lamella. The data are defined as the (x, z) coordinates of the non-zero pixels of the lamella within the reslice, while the corresponding weights are given by their intensity, since brighter signals are considered to be more reliable.

Figure 3.8 shows a schematic overview of the linear fit.

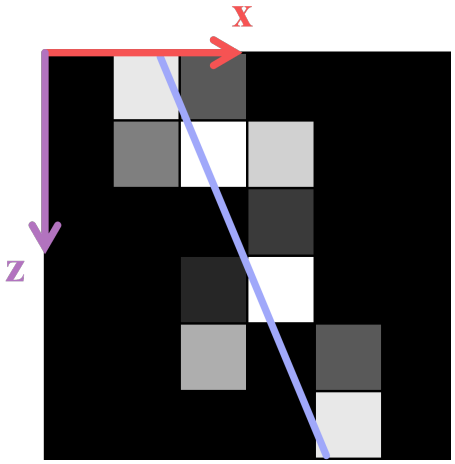


Figure 3.8: Schematic visualization of how a weighted linear regression (blue straight line) is fitted on a cloud of points that define one lamella in the reslice (non-black pixels).

From each regression line, and thus each lamella, one parameter was extracted: the absolute slope - computed after rotating the XZ-plane 90° counterclockwise to obtain a slope close to 0, given that the lamellae are vertically oriented.

3.7 Relative slopes

In the longitudinal plane of the osteon, that is in the reslice, it is often possible to visualize two segments of the same lamella, located on either side of the Haversian canal. To treat each pair of regression lines as a single lamella and to characterize it as such, the relative slope between the two lines was computed.

Let us consider a pair of regression lines. The intermediate line is defined as the set of points equidistant from both lines. This intermediate line is characterized by its own slope and intercept, referred to as the *intermediate slope* and *intermediate intercept*. Consequently, the regression lines have the same slope - but with opposite sign - relative to this intermediate line. From a mathematical point of view, if the two regression lines are described by the following equations:

$$x = a_1 z + b_1 \quad \text{and} \quad x = a_2 z + b_2$$

Then, the intermediate line is described by the following expression:

$$x = \left(\frac{a_1 + a_2}{2}\right) z + \left(\frac{b_1 + b_2}{2}\right) = \bar{a} z + \bar{b}$$

To compute the relative slope between the two lines, one must first determine the orientation angle of the intermediate line, denoted $\alpha = \arctan(\bar{a})$. If $\alpha_1 = \arctan(a_1)$ and $\alpha_2 = \arctan(a_2)$ are the angles of the two regression lines, then the relative slopes of these lines with respect to the intermediate line are given by:

$$a_{rel,1} = \tan(\alpha_1 - \alpha) \quad \text{and} \quad a_{rel,2} = \tan(\alpha_2 - \alpha)$$

This concept is illustrated schematically in Figure 3.9. The intermediate line, shown as a dashed pink line, enables the computation of a single common slope (up to a sign) for the lamella under consideration.

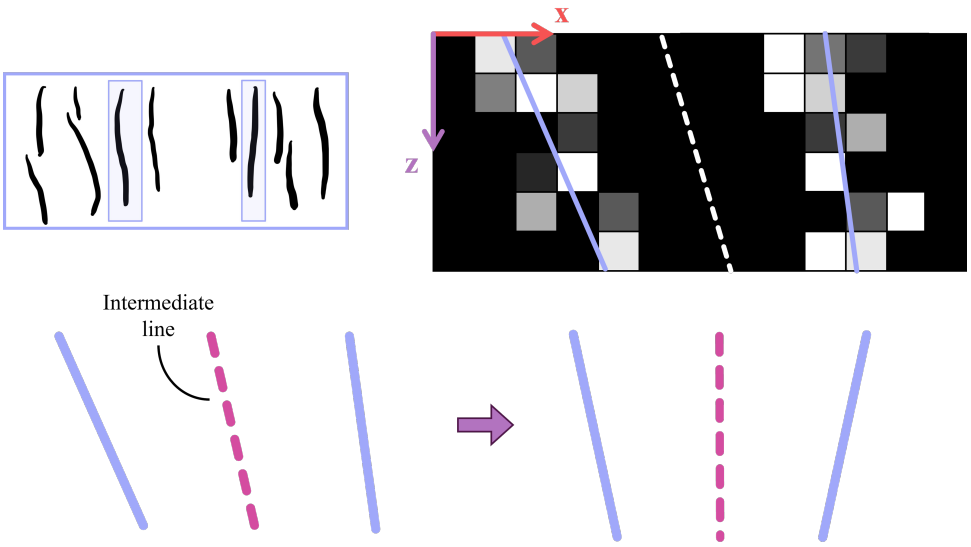


Figure 3.9: Schematic visualization of how the intermediate and relative slopes are defined. The blue lines depict the weighed linear regressions fitted on the two segments of the lamella highlighted in the blue frame within the reslice. The dashed white line represents the trajectory of the center of the Haversian canal through the depth of the osteon. Finally, the dashed pink line represents the intermediate line.

The main motivation behind the analysis of the relative slope of the linear regressions stems from the fact that the Haversian canal is not perfectly perpendicular to the surface of the sample, whereas the reslicing plane is. To account for this misalignment between the trajectory of the osteon's center of mass and the reslicing plane, introducing a reference line — namely the intermediate line — independent of the reslicing plane orientation is a relevant and appropriate approach.

3.8 Lamellar absolute angle vs. osteon rotation angle

From this step onward, the extent of the reslicing plane was divided by two. In other words, referring to Figure 3.7, this plane is defined only between $x = 512$ pixels and $x = 1024$ pixels. It is easily conceivable that, by rotating the osteon with respect to the center of the image, it is possible to follow the evolution around the Haversian canal of the same lamella in the longitudinal plane. In particular, it is possible to plot the lamellar angle μ — that is, the absolute angle of the observed segment of the lamella in the reslicing plane, with respect to the z-axis — as a function of the osteon rotation angle θ which spans from 0 to 360°, increasing by 30° each time. Figure 3.10 illustrates this concept.

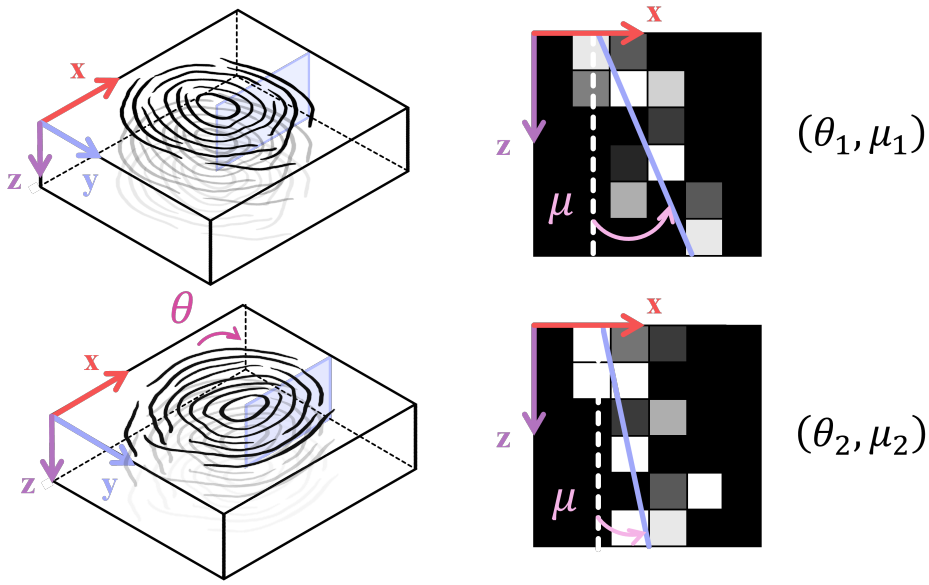


Figure 3.10: Schematic visualization of how the lamellar angle μ is defined and reported as a function of the osteon rotation angle θ. The concept is applied to only one lamella.

This process was ultimately applied not to a lamella, but to the trajectory of the osteon's center of mass (*i.e.* that of the Haversian canal) — which was assumed to coincide with that of the first clearly visible ring. To achieve this, a regression line was fitted to the five "centers of mass" determined and described in Subsection 3.4, in 3D. This line can be seen as an approximation of the trajectory of the osteon's center of mass, allowing it to be defined at any position along the z-axis. However, since the Haversian canal is not perfectly perpendicular to the imaging plane, the resulting trajectory is tilted with respect to this plane. Therefore, as the osteon rotates, the trajectory rotates as well. To correct for this rotation and compute the angle between the trajectory and the vertical z-axis, it is appropriate to project the trajectory onto the reslicing plane. This concept is schematized in Figure 3.11.

To fit a regression line to a cloud of points in space, the following approach was taken. First, the slope a_{xz} and x-intercept b_{xz} of a plane parallel to the y-axis which best fits the data are determined (allowing to disregard the y coordinate). Then, the same is performed for a plane parallel to the x-axis, providing a_{yz} and b_{yz}. The intersection of these two planes is the regression line that best fits the data. It is defined

by the following equations:

$$z = a_{xz}x + b_{xz} \quad \text{and} \quad z = a_{yz}y + b_{yz}$$

To derive a single expression that associates a pair (x, y) to a given value of z, one simply needs to isolate the variables x and y from the equations above, which gives:

$$x(z) = \frac{z - b_{xz}}{a_{xz}} \quad \text{and} \quad y(z) = \frac{z - b_{yz}}{a_{yz}}$$

Figure 3.11 illustrates how the trajectory of the osteon's center of mass is projected onto the reslicing plane. From a mathematical point of view, let L be the trajectory of the osteon's center of mass. This line is described by the following parametric equation:

$$L \equiv \begin{bmatrix} x \\ y \\ z \end{bmatrix} = \begin{bmatrix} x_0 \\ y_0 \\ z_0 \end{bmatrix} + \begin{bmatrix} a \\ b \\ c \end{bmatrix} t$$

Where $\begin{bmatrix} x_0 \\ y_0 \\ z_0 \end{bmatrix}$ represents any point of the line and $\begin{bmatrix} a \\ b \\ c \end{bmatrix}$ is its direction vector.

As the reslicing plane is defined at $y = 512$, the projected line L' is described by the following parametric equation:

$$L' \equiv \begin{bmatrix} x \\ y = 512 \\ z \end{bmatrix} = \begin{bmatrix} x_0 \\ y_0 = 512 \\ z_0 \end{bmatrix} + \begin{bmatrix} a \\ 0 \\ c \end{bmatrix} t$$

Since the components x and z remain unchanged after the projection, the a and c components of the direction vector remain the same as well. From this equation, two points of the projected line L' can be computed, from which the slope can be determined.

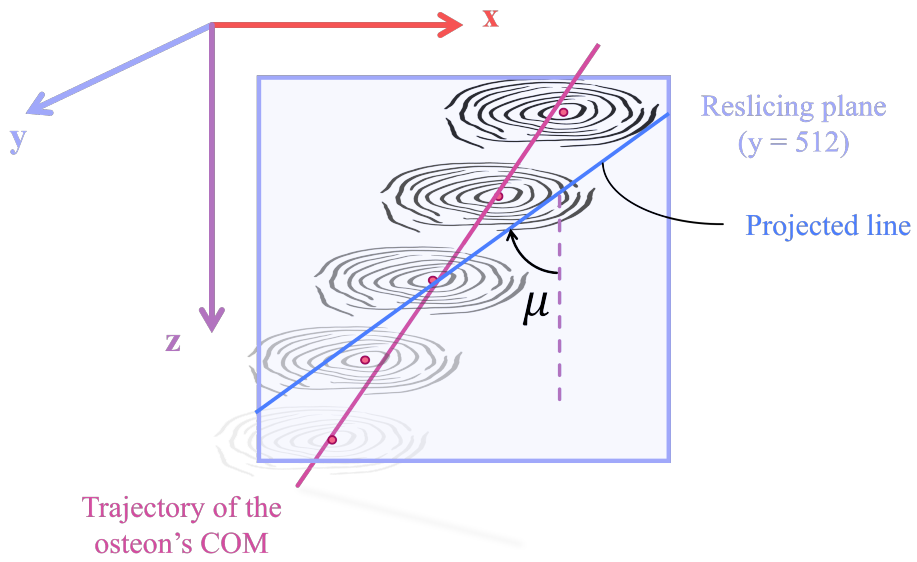


Figure 3.11: Schematic visualization of how the trajectory of the osteon's center of mass is determined, and how it is projected onto the reslicing plane.

3.9 Results and discussion

A) Qualitative inspection of osteon images

The first elements that we can analyze are the raw SHG images of the osteons. Figure 3.12 illustrates the first, middle and last slices from the entire stack of images of osteon 1.

As can be seen, when the osteon is imaged at depths close to 50 µm, the signal is quite weak and the image is barely visible. On the other hand, the signal is clearly visible at intermediate depths. It is rather clear that the weakness of the SHG signal generated at a high depth is due to the limitations of excitability. In other words, exciting deeper cross-sections becomes progressively more difficult at some point.

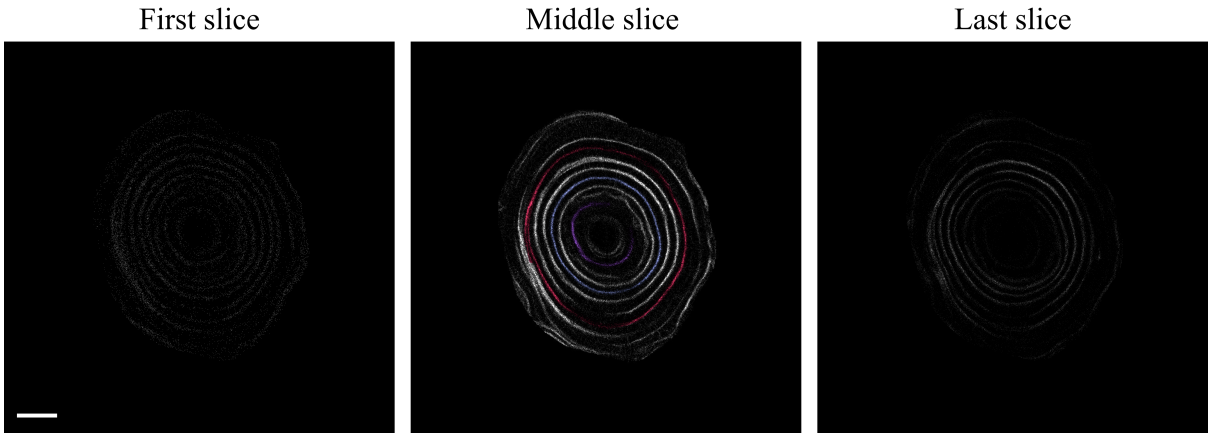


Figure 3.12: First, middle and last slices of the stack of images of osteon 1. In the middle slice, three particular configurations of bright bands (lamellae) are highlighted in colors. Scale bar: 40 µm.

In addition, we can note that the lamellae located closest to the Haversian canal appear darker and more irregular, with a weaker signal. As these are the 'younger' lamellae (*i.e.* they were deposited most recently), it is likely that collagen fibers are relatively disorganized or simply less densely packed. The rate of bone matrix apposition has been reported to decrease significantly as one approaches the Haversian canal (Buenzli et al., 2014), as osteoblasts tend to differentiate into bone lining cells or undergo apoptosis (Doube, 2022).

Far from the Haversian canal, near the interstitial lamellae, lamellae appear irregular as well. Two hypotheses may explain this observation. First, these lamellae were the first to have been deposited. Therefore, they do not reflect the same morphological characteristics as those located closer to the Haversian canal. Second, given their proximity to a neighboring osteon, their shape may be influenced by the presence of this adjacent Haversian system.

In the middle slice, three distinct lamellae were highlighted by coloring them. Typically, the structure of an osteon is described as a series of concentric rings, that are the lamellae (Doube, 2022). The lamella shown in blue represent a typical ring, concentric with its neighboring lamellae. However, we emphasize here the presence of two additional lamellar shapes: crescent-shaped lamellae (the one highlighted in purple) and spiral-shaped lamellae (the one colored in red).

In the literature, these three lamellar configurations have been reported, even within the same osteon (as is the case in this work). In a particular study (Pazzaglia et al., 2012), SEM images enabled the identification of what the authors refer to as *crescent-shaped lamellae* and *helicoidal lamellae*, although these structures appeared much less frequently than "classical" circular lamellae. These atypical structures are thought to be the result of a less "conventional" activity of osteoblasts. These cells typically work together, forming a functional pool (Pazzaglia et al., 2010). In principle, their activity is synchronized and phasic, which leads to the formation of a circular lamella. However, if their activity becomes de-

synchronized or irregular, the rate of osteoid deposition is not the same for all osteoblasts anymore. As a result, some osteoblasts deposit more osteoid than others, leading to the formation of other lamellar patterns. Figure 3.13 illustrates a schematic overview of how lamellae are formed depending on whether the osteoblast activity is synchronized or not.

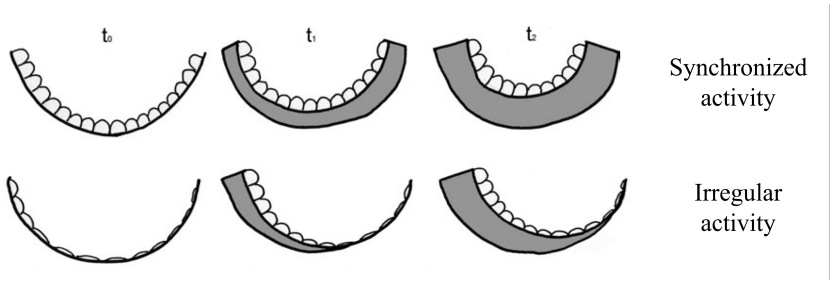


Figure 3.13: Schematic representation of how lamellae are formed, depending on whether the osteoblast activity is synchronized or not. A synchronized activity will lead to a circular lamella, while an irregular activity will lead to another shape. Figure from (Pazzaglia et al., 2012).

An irregular activity may be triggered by inhibitory signals emitted by osteoclasts (Pazzaglia et al., 2012).

It is also important to note that the rate of matrix deposition depends on several factors, including the surface density of active osteoblasts and their secretory activity. Local variations in these parameters may also explain the presence of these spiral- and crescent-shaped lamellae. Nevertheless, these observed patterns may simply result from signal loss, whether due to limitations of the imaging technique (described in details in Subsection 1.2.2 D), local optical properties of the collagen fibers, or other unknown factors. Imaging the osteons using another technique, such as FIB-SEM, could provide additional insights and enlighten our interpretation.

The three lamellar forms were also observed in the two other osteons (see Appendix A).

B) Osteon binarization

Comparisons between the raw image and the binarized image, obtained after segmenting the stack, can be observed in Figure 3.14. As can be seen, the image processing and segmentation appear effective, as they allow for a clear distinction between bright and dark bands, enhance SHG signals barely visible to the naked eye (as indicated by the red arrows), and improve the separation between two adjacent lamellae that eventually merge together (as highlighted by the blue arrow).

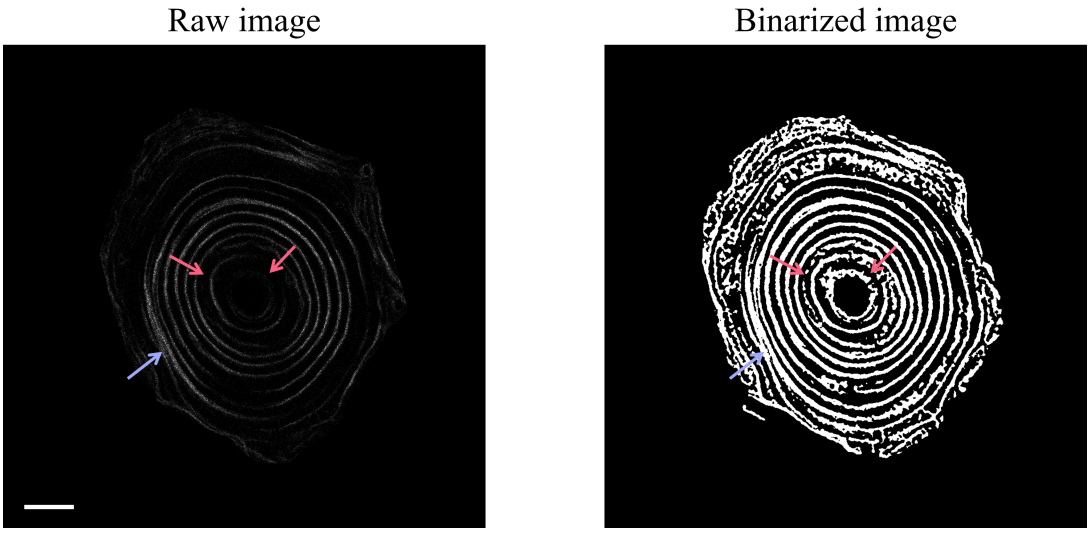


Figure 3.14: Comparison between the raw image and the binarized image for Osteon 1 (slice 68 out of 136). The red arrows indicate regions where the signal, barely visible to the naked eye, is enhanced and clearly appears on the segmented image. The blue arrow indicates a region where two adjacent lamellae are about to intersect. In the binarized version, these lamellae are separated as much as possible. Scale bar: 40 µm.

The observation that two distinct lamellae merge into a single bright band (as indicated by the blue arrow in Figure 3.14) has been previously noted in the literature (Hegarty-Cremer et al., 2024). This phenomenon could be explained by a localized delay in bone matrix apposition along part of the surface of the Haversian canal. As a result, a succession of deposition fronts formed at different times intersect in specific regions.

The binarized image confirms that, once again, the signal near the Haversian canal is weak, as the white pixels fail to form well-defined lamellae. Although one can guess that the pixels aim to form circular arrangements, these are incomplete and fragmented. This aligns with the discussion provided in the previous subsection. Even at the periphery of the osteon, the signal remains somewhat diffuse, with many areas where the lamellae do not form continuous structures. We assume that these observations are associated with a disordered arrangement of collagen fibers in these regions of the osteon.

One can find the comparison between raw and binary images of osteons 2 and 3 in Appendix B.

C) Osteon reslicing

Before presenting the results of osteon reslicing, it is essential to verify that the presumed global center of mass of the osteon (defined in Section 3.4) remains within the boundaries of the Haversian canal. If this is not the case, reslicing the osteon may result in cuts performed outside the canal, which is undesirable.

Figure 3.15 illustrates the position of the global center of mass in the binary images of the first and last slices, along with the three equally spaced intermediate slices. As can be seen, the global center of mass is always located within the Haversian canal. In cases where the center appears close to the innermost lamella, a magnified view is provided for clarification. Nevertheless, the center remains contained within the canal in all cases.

The same was true for the two other osteons (see Appendix C).

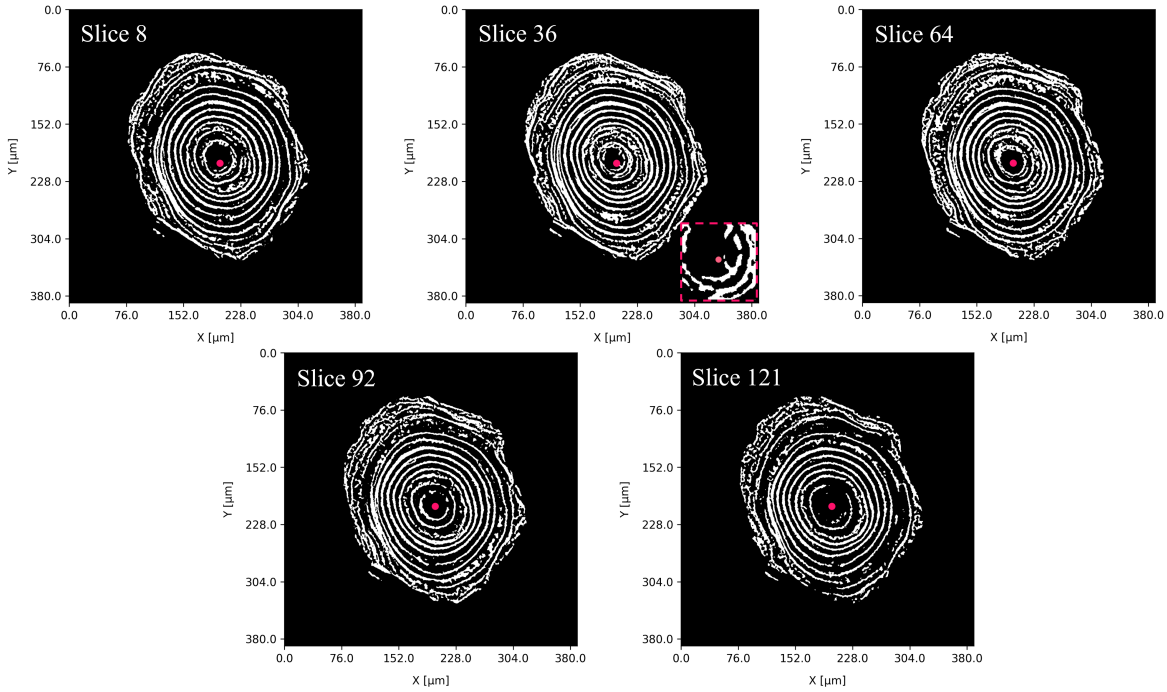


Figure 3.15: Specific slices of the binarized stack of images of osteon 1. For each slice, the global center of mass of the osteon is displayed as a red point. A magnified view is illustrated when the point is close to the innermost lamella. In all slices, the global center of the osteon remains within the Haversian canal. The number of each slice is indicated (out of 136).

To help navigate between the transverse plane (*i.e.*, the XY-plane) and the longitudinal plane (XZ-plane), each lamella has been labeled with a specific color. Figure 3.16 illustrates the osteon in the imaging plane along with the reslices performed every 30°, from 0° to 150°.

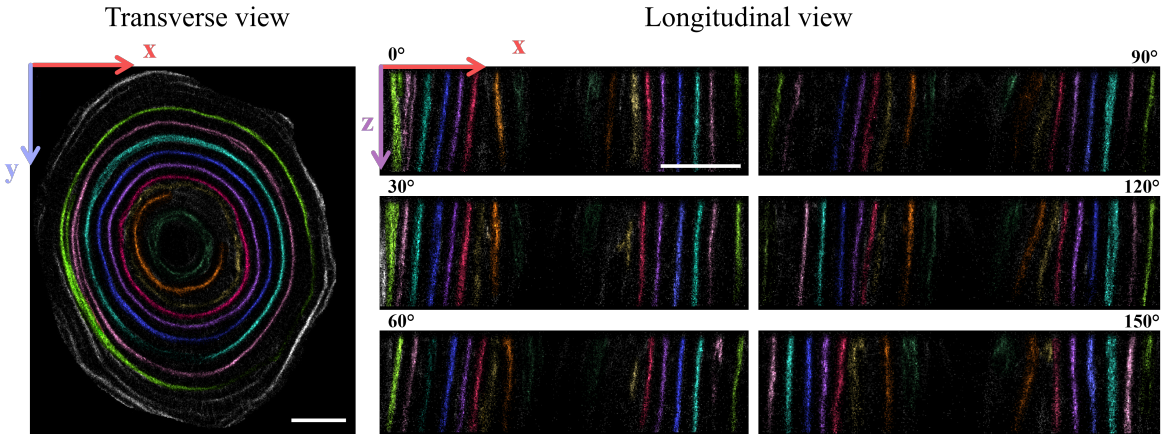


Figure 3.16: Reslices of osteon 1. The lamellae have been labeled through coloring to facilitate their identification from one cut to another, and their matching with respect to the the transverse plane. Scale bars: 40 µm.

Several observations can be made:

- Crescent-shaped lamellae (such as the orange one) are, unsurprisingly, not visible on both sides of the Haversian canal in all reslices. For example, at 60°, the orange lamella is only visible on the left side of the canal. This suggests that the lamella maintains its crescent shape throughout the osteon.

- Spiral-shaped lamellae (like the pink one) appear at certain angles as two distinct, closely positioned segments (see the pink segments at 0°, on the left side).
- Lamellae located close to the Haversian canal, notably the dark green and yellow lamellae, are not clearly visible, whether in the transverse plane or in the longitudinal plane. They appear as very thick clouds of pixels. This aligns with the idea presented in previous sections, that these lamellae might be composed of disorganized collagen fibers. As one moves away from the canal (starting from the red lamella), the bands and segments appear more clearly defined and "compact".

The same results for the two other osteons can be seen in Appendix D.

D) Linear regression fit

Figure 3.17 shows an example of a reslice with linear regressions fitted to each lamella. The reference reslice, in which lamellae are color-coded, is also illustrated. The regression lines have been labeled to facilitate the identification of individual lamellae. As shown in the dashed purple frame, the regression lines provide a good fit to the lamellar pixel distributions. We deliberately chose not to report R^2 values, for reasons that are discussed in detail at the end of this chapter.

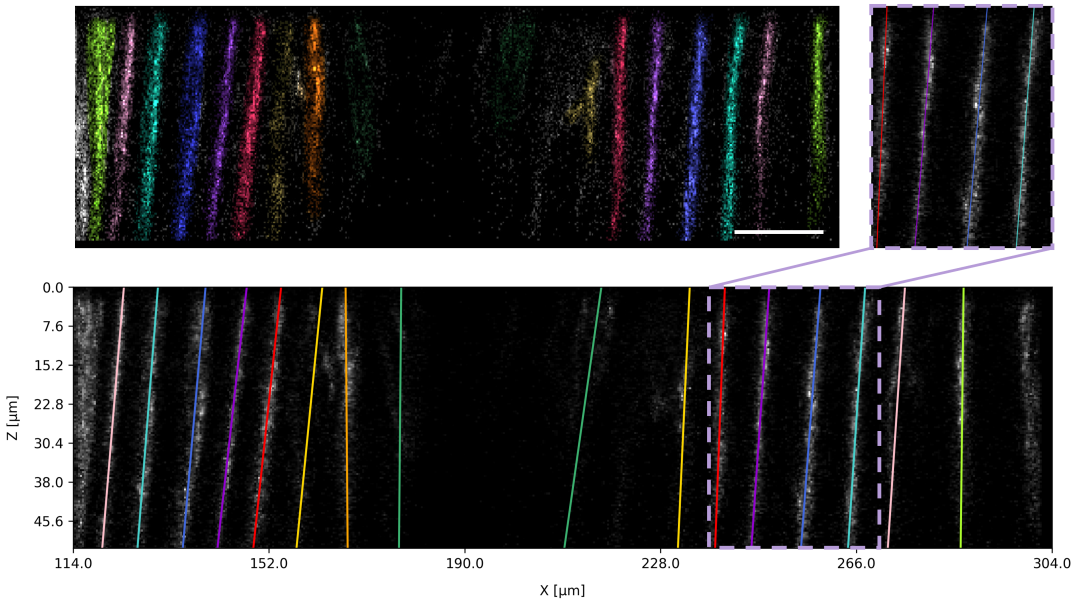


Figure 3.17: Regression lines fitted to the lamellae visible in a reslice obtained after rotating the osteon by 30°. The top-left image serves as a reference. Both the lamellae and the corresponding regression lines are color-coded to facilitate identification. As shown in the dashed purple frame on the top right, the regression lines closely follow the cloud of lamellar pixels. Scale bar: 20 µm.

By rotating the osteon, one can track the evolution of the linear regressions across different reslices of the osteon. This is illustrated in Figure 3.18.

Several elements can be observed. First, the regression lines are not perfectly vertical. Instead, they exhibit an oblique orientation.

Furthermore, when we examine the same side of the reslice (either to the left or to the right of the Haversian canal), all regression lines do not exhibit the same orientation. Some point towards the bottom right corner, while others point towards the bottom left corner. This is particularly evident when we compare the two innermost lamellae (*i.e.* the dark green and orange lamellae) with the others.

Finally, for certain lamellae - such as the two innermost ones - one can easily guess that the two corresponding segments seem to point towards the same point, suggesting that the lamella has a conical

shape. However, this is more difficult to assess for the other lamellae. Therefore, it becomes necessary to provide quantitative measures to rigorously assess the linear regressions.

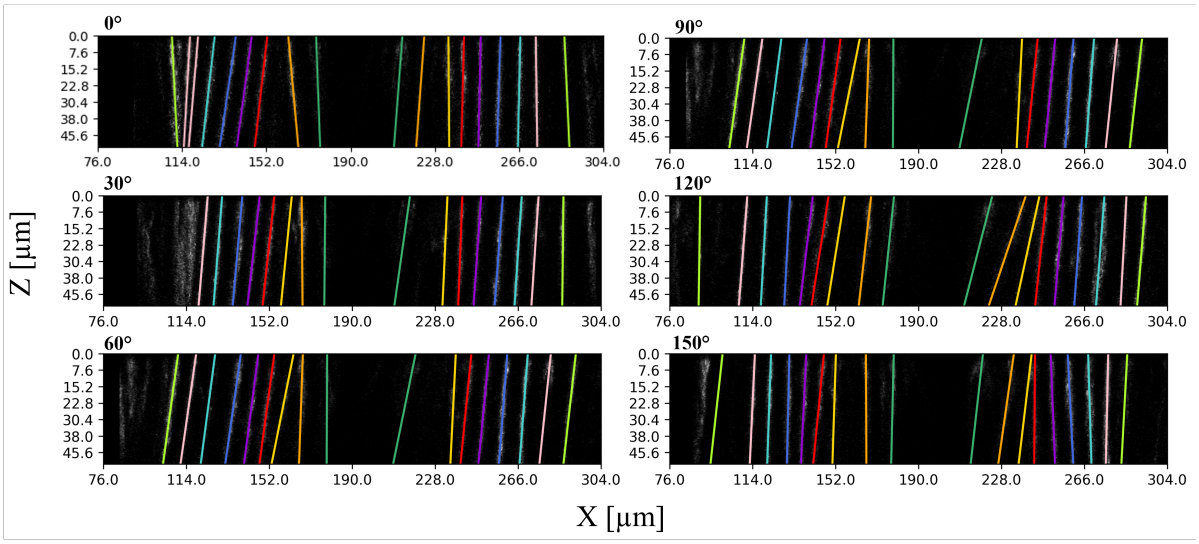


Figure 3.18: Regression lines fitted to the lamellae visible in all reslices, obtained after rotating osteon 1 every 30°. The same results for the two other osteons are shown in Appendix E.

As a first step, the regressions have been color-coded according to their slope value, similar to a heatmap representation. The results are presented in Figure 3.19.

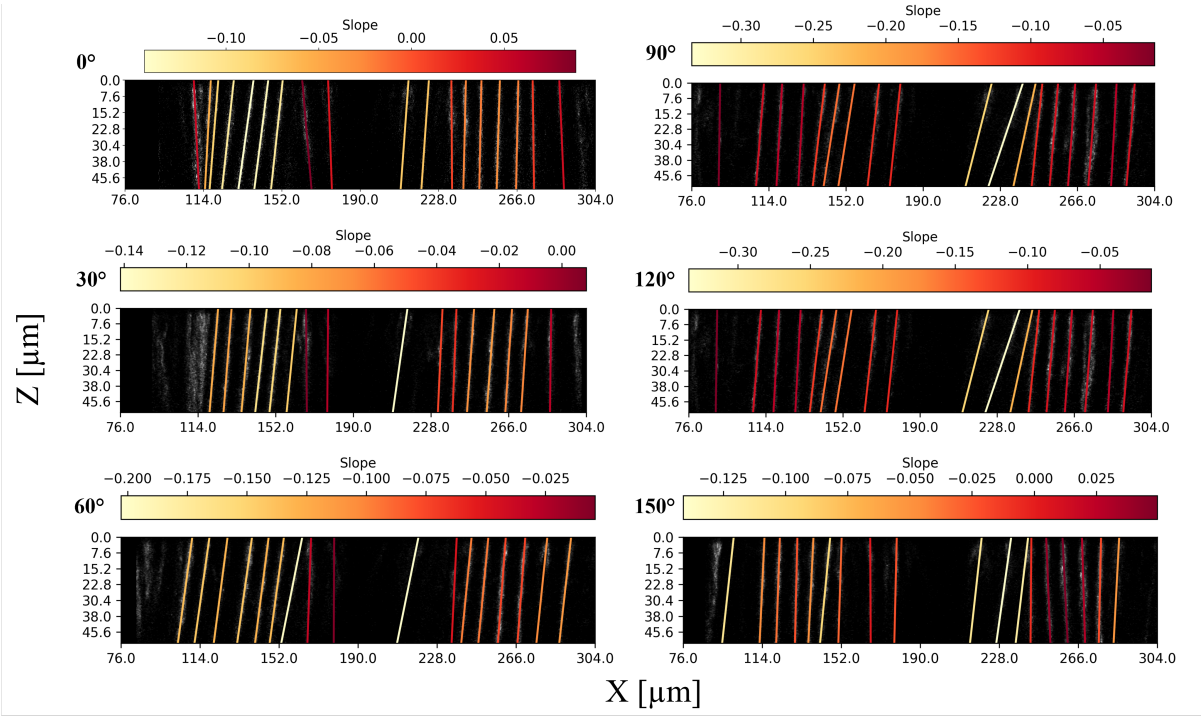


Figure 3.19: Color-coded regression lines according to slope values. All reslices of osteon 1 are shown. The same can be seen for the two other osteons in Appendix E. The limits of the color bars are not the same for all reslices, in order to highlight the observations mentioned in the results subsection.

Alternatively, these slopes can be presented in the form of a histogram, providing the same information displayed differently. The y-axis has been inverted so that the bars are mainly oriented upwards, as the

lamellar slopes generally take a negative value.

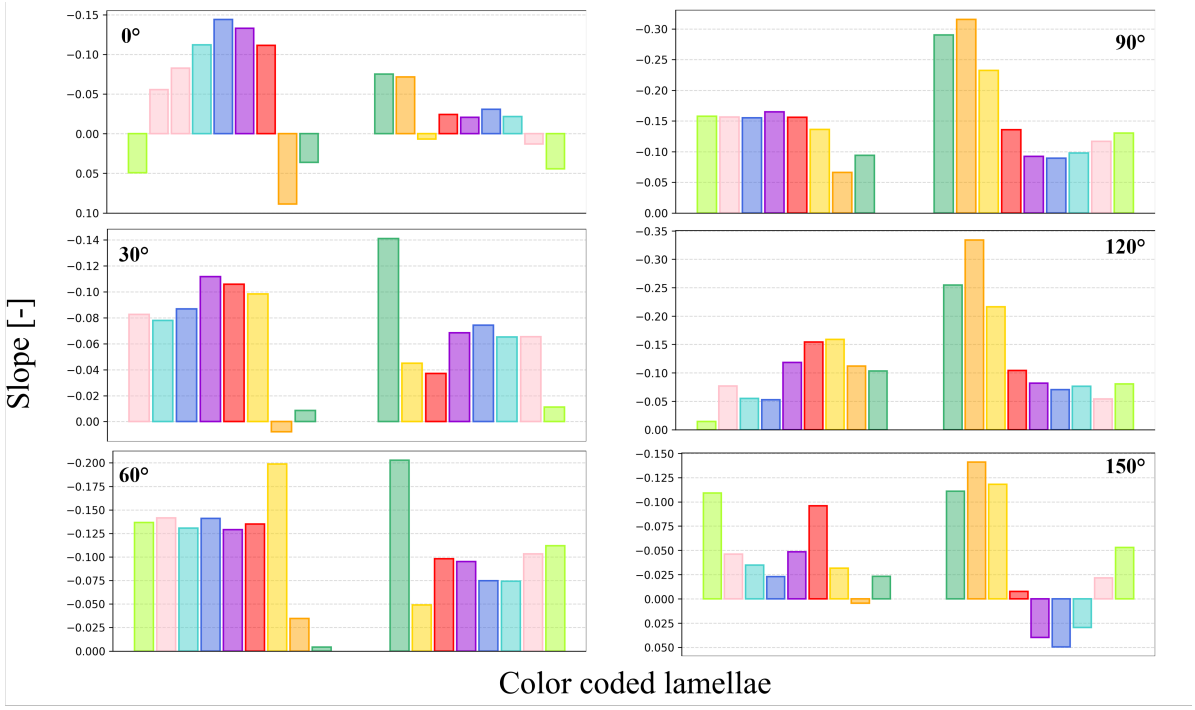


Figure 3.20: Histograms displaying the slope of each linear regression. Each bar corresponds to a lamellar segment and shares its respective color. The lamellae are arranged in the same way as in Figure 3.18, with the gap representing the Haversian canal. These images are related to osteon 1. For the two other osteons, refer to Appendix E.

Figures 3.19 and 3.20 provide several key insights.

First, on the same side of a given reslice, lamellae exhibiting opposite orientations can be observed. In fact, some point towards the Haversian canal, while others point towards the lateral periphery of the osteon. In the heatmap, this this is reflected by lamellae displaying the extreme ends of the color bar (*i.e.* dark red and light yellow). In the histograms, this is indicated by the presence of both positive and negative slopes - although negative most of the time. A clear example can be visualized on the left side of the 0° reslice. This suggests a certain degree of independence between lamellae.

On the other hand, it can also be observed that neighboring lamellae sometimes exhibit similar slopes. In the heatmap, this is reflected in nearby lamellae that have the same color. In the histogram, this is indicated by bars of similar height. Adjacent lamellae may exhibit such similarity in pairs (*e.g.*, the turquoise and dark blue lamellae on the left side of the 120° reslice), in triplets (*e.g.*, the purple, dark blue, and turquoise lamellae on the right side of the 150° reslice), in quadruplets (*e.g.*, the red, purple, blue, and turquoise lamellae on the right side of the 0° reslice), or even in larger groups (*e.g.*, all lamellae between the red and the light green ones on the left side of the 60° reslice). This observation suggests, in contrast with the previous paragraph, that there may be a certain degree of interdependency between lamellae, especially if they are located close to each other. Notice how this tendency occurs clearly between the red, purple, blue, and turquoise lamellae, which are located neither too close to the Haversian canal nor near the interstitial lamellae. One could infer that in this intermediate region, lamellae are relatively well organized and have a fairly similar structure. In addition, recall that these lamellae are the ones that appear most clearly in the binarized images, suggesting that they are readily distinguishable from adjacent lamellae, lacking the ambiguity that may arise with the SHG signal associated with other lamellae of the osteon.

We can also notice that the innermost lamellae - that is, the green and orange ones - have similar structural characteristics that conversely differ from those of other lamellae. In each reslice, these lamellae tend to show a significantly steeper slope on the right side and a shallower slope on the left side, compared to the surrounding lamellae. As these internal lamellae were the most recently deposited, it may be that they are still in an early stage of bone remodeling, which means their structure is still disorganized. This interpretation is further supported by the fact that the pixel clouds corresponding to these lamellae appear relatively thick and diffuse in the longitudinal plane of the osteon.

Finally, a particularly noteworthy observation lies in the fact that, within any given reslice, bars of the same color never exhibit the same height in the histograms. Since this holds for all reslices, it suggests that lamellae do not form cylindrical structures around the Haversian canal, but rather conical ones. This was already obvious for the green and orange lamellae in Figure 3.18, but the current analysis confirms that it applies to all lamellae. If these layers were perfect cylinders - even if tilted relative to the imaging plane - one would expect very similar slopes, resulting in bars of the same color having almost equal heights.

The hypothesis that lamellae are arranged in a cylindrical fashion has been widely suggested in the literature (Dempster, 2017; Andronowski and Cole, 2021; Parfitt, 1994). On the other hand, our observations strongly align with the findings of Doube et al. (Doube, 2022), who explain that a secondary osteon is indeed made up of concentric cone-shaped lamellae. To understand why this statement makes sense, one must first visualize the resorption and formation fronts formed by osteoclasts and osteoblasts, respectively (see Figure 3.21).

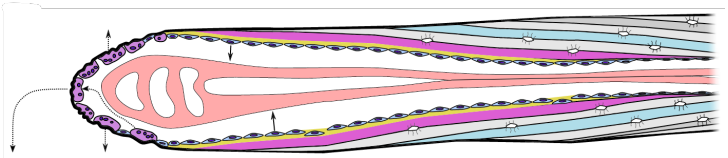


Figure 3.21: Schematic illustration of bone remodeling in an osteon. The purple cells, which are osteoclasts, form the resorption front and the cutting cone. The blue cells, representing osteoblasts, constitute the formation front and the closing cone. Arrows show the movement of these cells as they take action. Image from (Doube, 2022).

There are two main reasons that explain the plausibility of a conical lamellar model:

- First, if lamellae were cylindrical (as illustrated in Figure 3.22A), osteoblasts would have to deposit osteoids simultaneously on several layers, which is not biologically plausible. In contrast, a conical configuration (as can be seen in Figure 3.22B) allows for the formation of one lamella at a time, as osteoblasts are coordinated to deposit collagen fibers with a common orientation. Consequently, it makes sense that lamellae are parallel to the formation front, and thus to the closing cone.
- Second, this model provides explanation for the ability of lamellae to deflect cracks either towards the Haversian canal or towards the cement line (Doube, 2022).

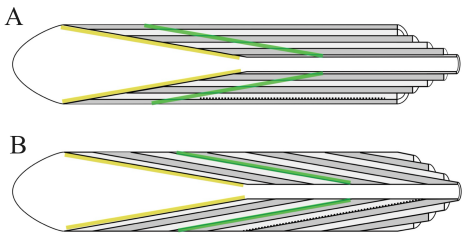


Figure 3.22: Schematic illustration of two lamellar models. **A.** Cylindrical arrangement of lamellae. **B.** Conical arrangement of lamellae. The yellow lines depict the formation front. Image from (Doube, 2022).

This conicity was also observed in the two other osteons (see Appendix E).

E) Relative slopes

Given that most lamellar slopes are negative, we found it appropriate to introduce the concept of intermediate lines, which can be seen as median lines between two segments of the same lamella, and to compute the relative slope of these segments with respect to the line. Consequently, we can fully characterize the lamellar conicity. Figure 3.23 displays three histograms: one for the slopes of the intermediate lines, one for their x-intercepts, and one for the resulting relative slopes of the lamellae. To avoid cluttering the report with redundant information, only the characteristics related to the 120° reslice for osteon 1 are presented.

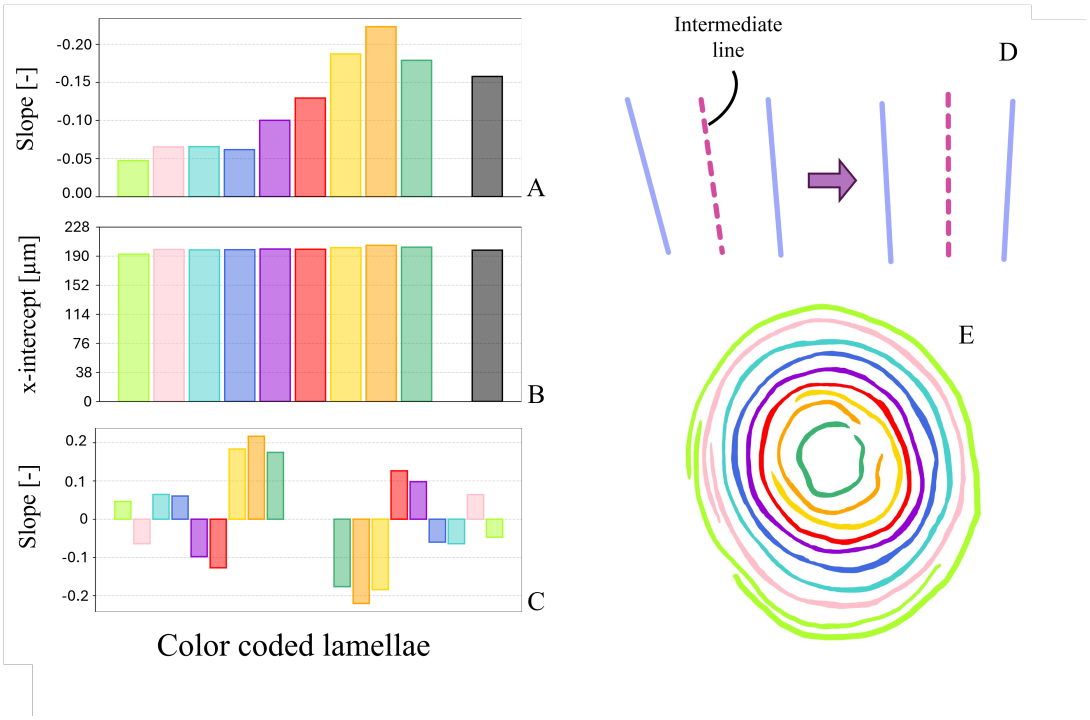


Figure 3.23: Histograms associated with the intermediate lines. **A.** Slope of the intermediate lines. **B.** x-intercept of the intermediate lines. **C.** Relative slope of the linear regressions, with respect to the corresponding intermediate lines. For the intermediate slope and intercept, one bar is displayed per pair of segments of the lamella that shares the same color. The black bar corresponds to the projection of the center of mass trajectory of the osteon. **D.** Reminder of how the relative slopes are defined with respect to the intermediate line (in pink). **E.** Color coded lamellae, for reference. These plots are associated with the 120° reslice of osteon 1.

For each of the three histograms, a few comments can be made:

- The slope of the intermediate lines (see Figure 3.23A) varies depending on the lamella under consideration. However, it can be noted that the three innermost lamellae (*i.e.* dark green, orange, and yellow) exhibit intermediate lines with relatively steep and comparable slopes. Similarly, the four outermost lamellae (*i.e.* dark blue, turquoise, pink, and light green), have intermediate lines with similar but rather small slopes - indicating that the line is more perpendicular to the imaging plane. The lamellae located between these two groups are characterized by intermediate slopes with moderate magnitude. Finally, the black bar exhibits a height comparable to that of the innermost lamellae. This makes sense since the Haversian canal is delimited by the dark green lamella. Therefore, it is expected that their intermediate lines share similar characteristics.
- The fact that the x-intercepts of the intermediate lines (see Figure 3.23B) are almost identical - centered near $x = 195$ µm, which is the x position of the center of the image - simply indicated that these lines originate from a common point, with only their slopes varying along the depth of

the osteon. This would suggest that, as the surface of the cortical bone is approached, the centers of mass of the different lamellae progressively align.

- As expected, the relative slopes of the segments of the same lamella exhibit the same magnitude with opposite signs. What is remarkable is that these slopes do not share the same sign when positioned on the same side of the reslice relative to the Haversian canal. This suggests that, in this particular reslice, the dark green, orange, yellow, blue, turquoise, and light green lamellae appear to be narrowing, like a cone whose apex is oriented downward. In contrast, the remaining lamellae appear to be widening, akin to a cone whose apex is oriented upward. This indicates that lamellae do not evolve in the same way. However, one must note that this is only valid for a specific cut of the osteon. Had the rotation angle of the osteon been different, it is likely that all lamellae would appear to be narrowing in the corresponding reslice. The diagrams displayed in Figure 3.24 illustrate the spatial implication of this observation: if one imagines that the lamella is viewed from above (see Figure 3.24A) - forming a ring in the transverse plane - the blue reslice (see Figure 3.24B) would make the lamella appear to narrow, whereas the pink reslice (see Figure 3.24C) would make it appear to widen.

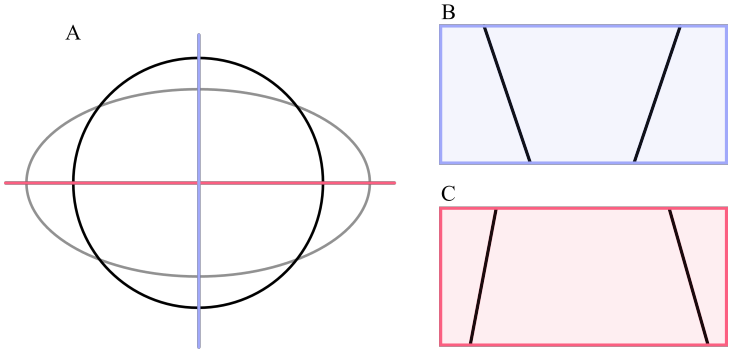


Figure 3.24: Schematic representation of a lamella exhibiting narrowing in one reslice and widening in another. **A.** Top view of the lamella. The circle represents a cross-section near the surface of the cortical bone, while the ellipse corresponds to a deeper cross-section. **B.** Longitudinal view of the lamella in a specific reslice. The lamella appears to narrow. **C.** Longitudinal view of the lamella in another perpendicular reslice. The lamella appears to widen.

F) Lamellar absolute angle vs. osteon rotation angle

In this analysis, the reslicing plane is reduced by half, and each lamella of the osteon is tracked throughout a full 360° rotation. The angle between the regression line and the z-axis is recorded at 30° intervals. In short, the only difference from the previous analysis lies in the fact that, here, only one segment of the lamella is considered at a time.

Before presenting the results, we briefly illustrate the regression line fitted to the the center of mass of the osteon at several slice levels (see Section 3.4), as can be seen in Figure 3.25. Panel A shows that the regression line (blue) provides a good fit to the points (red), especially when viewed at the scale of the entire image stack. This suggests that, on a global scale, the centers of mass are relatively aligned.

However, when we project these points and the regression line onto the XZ-plane and zoom in, small deviations from a perfect alignment can be seen (as shown in Figure 3.25B). Although the line captures the trend quite well, the centers of mass do not lie along a straight path. This indicates that the osteon - and in particular the Haversian canal - is not a perfectly straight structure. The projected trajectory reveals that the osteon shifts laterally by approximately 3 µm. This observation is supported by qBEI images of osteons that were longitudinally sectioned (Doube, 2022). In simple words, the center of the Haversian canal does not seem to describe a straight trajectory. However, it is possible that our findings are simply the result of binarization, which may introduce variability, especially given that the lateral

shift is not pronounced.

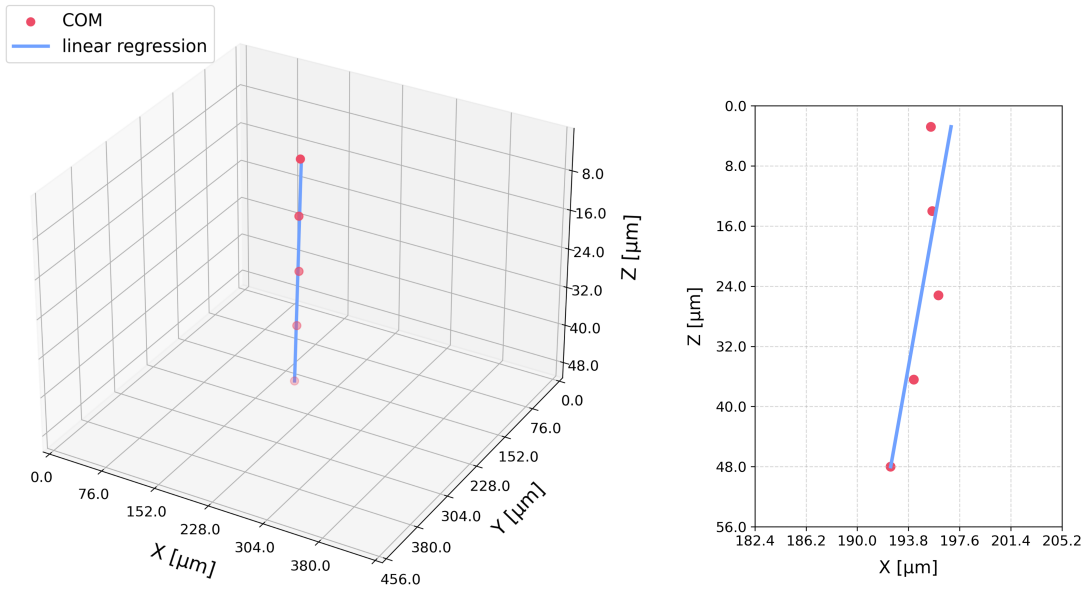


Figure 3.25: **A.** Linear regression (blue line) fitted to the center of mass of osteon 1 measured at different depths (red points). The same plots for the two other osteons can be seen in Appendix F. **B.** Projection onto the XZ-plane with increased magnification. The fact that points are not aligned suggests a possible lateral deviation of the Haversian canal throughout the depth.

Now that the trajectory of the osteon's center of mass has been fully described, we can illustrate the evolution of the inclination of each lamella as a function of the osteon rotation prior to reslicing. This is depicted in Figure 3.26. When a lamella exhibits a spiral shape, the slope of each individual segment of the reslice is displayed as a point – which explains why two (or more) points of the same color can appear for a single value of θ. However, only the average slope is used to make connections between points.

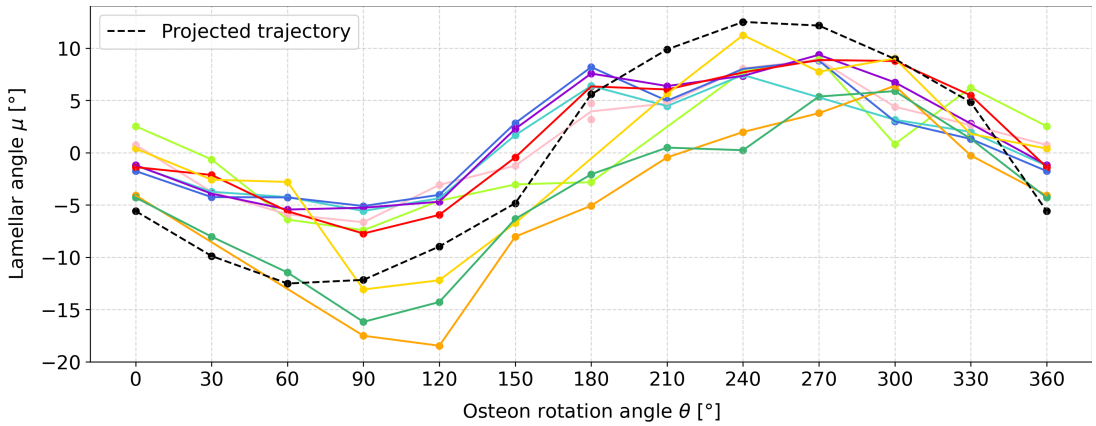


Figure 3.26: Lamellar absolute angle as a function of the osteon rotation angle. The angle is computed relative to the z-axis. The black dashed line corresponds to the orthogonal projection of the osteon's center of mass trajectory onto the reslicing plane.

First, it is important to understand that this graph provides essential information about the three-dimensional structure of the lamellae, although in an implicit manner. The most striking observation is that all the curves exhibit a smooth sinewave shape, which is relatively symmetrical around $\theta \approx 180°$. This suggests that lamellae share a three-dimensional pattern that evolves in a similar way along the angular

coordinate θ. However, the fact that these curves do not perfectly overlap indicates that this pattern is not identical across all lamellae.

Based on this pattern, it is theoretically possible to infer the three-dimensional structure of a lamella. This could be achieved by designing several idealized and simplified models of one lamella and applying the protocol described in this chapter to each of them. For instance, if the lamella is a perfect hollow cylinder, parallel to the z-axis, the resulting curve $\mu(\theta)$ would be constant, with $\mu = 0°$. If it were a truncated cone, $\mu(\theta)$ would be constant as well, but equal to a fixed value corresponding to half of the cone's opening angle within the reslicing plane. This is illustrated in Figure 3.27. To produce a sinewave, we would likely need to slightly tilt the cone. Although these models were not tested in this work, it is evident that the three-dimensional structure of the lamellae can, in principle, be inferred from Figure 3.26.

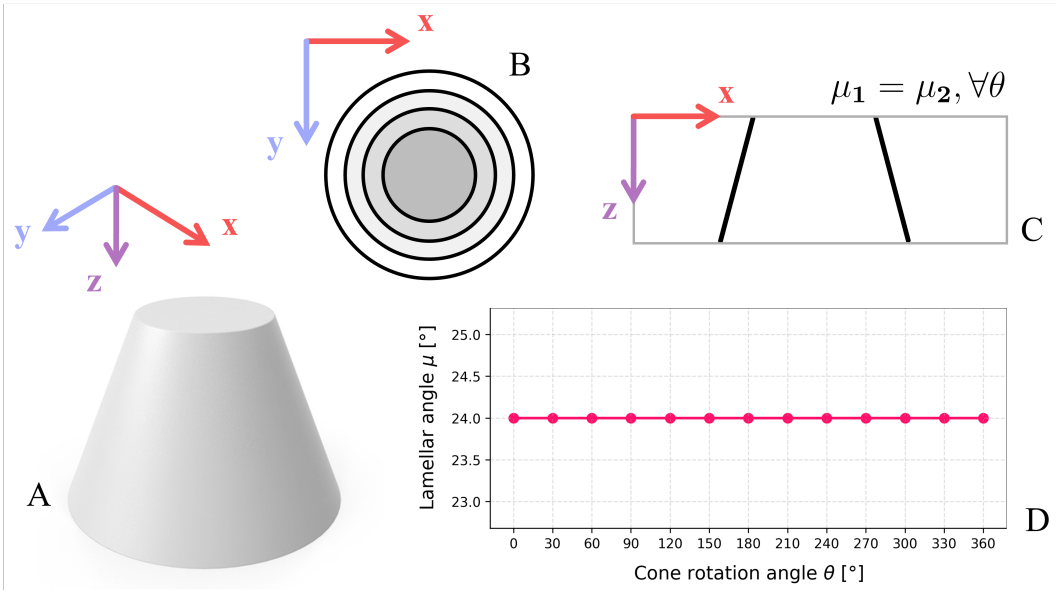


Figure 3.27: Idealized model of the lamella as a truncated cone. **A.** Visual representation of the conical model. **B.** Cross-sectional view of the model in the transverse plane, where each disc represents a slice of the cone. **C.** Reslice of the model. The lamella appears as two lines that exhibit the same absolute angle μ with respect to the z-axis, regardless of the rotation angle θ of the cone. **D.** Plot of the lamellar angle as a function of the rotation angle of the idealized model. The lamellar angle remains constant and corresponds to half of the cone's opening angle within the reslice plane.

Even more remarkably, this sinewave pattern is consistently observed for the two other osteons as well (as can be seen in Figure 3.28). This suggests that the osteons – and more specifically lamellae – exhibit a three-dimensional structure which evolves similarly across the angular position θ.

These curves offer an alternative way of representing the results of Figure 3.20, where the lamellar slopes were illustrated in the form of histograms. Accordingly, the same observations remain valid here. In particular, one can notice that some lamellae appear not only to evolve in a comparable way as the osteon rotates – given the sinewave pattern – but also to exhibit a very similar structure. This is reflected in curves that are proximal to each other and almost overlap. We are referring to the red, blue, turquoise, and purple lamellae of osteon 1. This is a plausible observation, since these lamellae are located at intermediate radial positions within the osteon. It had been previously hypothesized that this region is characterized by a relatively high degree of lamellar organization, which may account for their structural similarity.

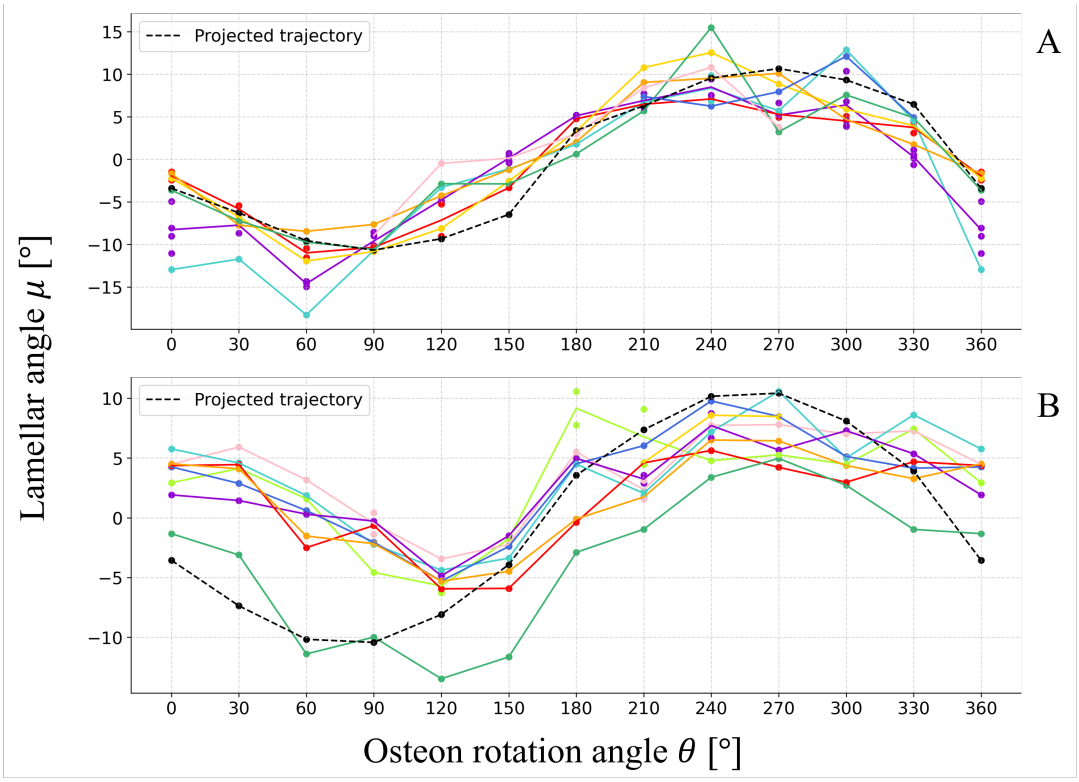


Figure 3.28: Lamellar absolute angle as a function of the osteon rotation angle. The angle is computed relative to the z-axis. The black dashed line corresponds to the orthogonal projection of the osteon's center of mass trajectory onto the reslicing plane. **A.** Osteon 2 and **B.** Osteon 3.

The black dashed line - which corresponds to the projection of the linear regression fitted to the osteon's centers of mass onto the reslicing plane - also exhibits a sine-wave-like profile. However, we expected it to display an intermediate amplitude compared to that of the lamellae. This does not seem to hold true within the angular ranges of 0°-60° and 190°-300° (for osteon 1). In these regions, this would simply suggest that the trajectory of the center of mass is much more inclined than the lamellae.

Another observation is that the green and orange curves - for osteon 1 - do not appear to be centered around $\mu = 0°$. Instead, they are slightly shifted towards negative μ values. This simply provides further insight into their orientation. These lamellae not only have one segment that is noticeably more inclined than the other, but are also characterized by a conical shape oriented towards the lower left corner. Figure 3.18 clearly supports this interpretation. In contrast, the remaining lamellae exhibit two segments with more comparable slopes.

Similarly, the x-intercept of each lamella can be plotted as a function of the osteon rotation angle θ. It should be noted that the coordinate system was centered at $x = 512$ pixels to align with the center of the image. As illustrated in Figure 3.29, the intercept evolves in a similar manner across the different lamellae, suggesting that, at least at the level of the first slice, lamellae have a similar shape. This observation is consistent with the transverse view of the osteon (as can be seen in Figure 3.16). Moreover, one can notice that the spacing between adjacent lamellae in the first slice – given by the distance between successive curves – appears to remain relatively constant with respect to θ. Similar observations can be made in osteons 2 and 3 (see Appendix F).

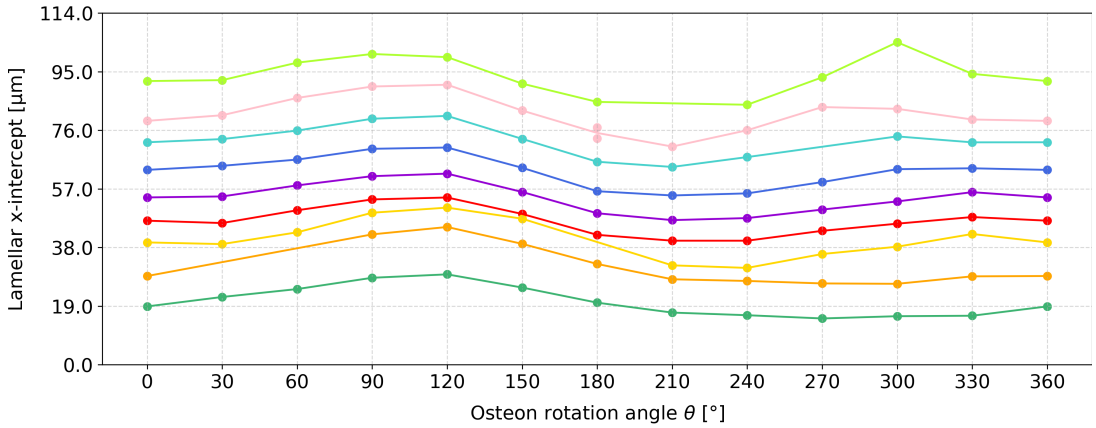


Figure 3.29: Lamellar x-intercept as a function of the osteon rotation angle. The coordinate system was shifted to align with the center of the image, to have consistent values.

Before closing this chapter, we would like to emphasize one final point. When linear regressions were fitted to the different lamellae, we did not report any R^2 value - or any other metric that evaluates the goodness of fit. In fact, R^2 values were computed, but they consistently remained close to zero. This may seem counterintuitive given that, as illustrated in Figure 3.17, the fitted lines appear to closely follow the lamellae. This inconsistency stems from the way R^2 is calculated:

$$R^2 = 1 - \frac{\sum_i w_i (x_i - \hat{x}_i)^2}{\sum_i w_i (x_i - \bar{x}_w)^2}$$

where:

- x_i denotes the actual x-position of a pixel,
- $\hat{x}_i$ is the corresponding value predicted by the linear model,
- w_i represents the weight associated with pixel i, that is, its intensity,
- $\bar{x}_w = \dfrac{\sum_i w_i x_i}{\sum_i w_i}$ is the weighted mean of x.

Since the regression lines are nearly vertical - as can be observed in Figure 3.16 - the x-coordinate does not change significantly between pixels, making $\bar{x}_w \approx x_i$ for all i. This leads to a small denominator in the formula, driving the R^2 metric towards 0, despite the regression lines closely match the pixels.

Alternative metrics used for assessing the goodness of fit do exist, such as the Pearson's correlation coefficient. However, they do not have a well-establish formulation that accounts for the weight factors. Consequently, we limit our assessment to qualitative and visual inspection, from which it is evident that the regressions capture the lamellar orientation quite accurately (as shown in Figure 3.17).

Chapter 4

Three-dimensional modeling of lamellae

4.1 Introduction

This second part of the project aims to outline the implementation of a methodology for generating a mathematical representation of the osteon. As previously observed, osteons' SHG images appear as grayscale pixel clouds which, in general, exhibit periodic, ring-like structures. Despite the high level of contrast, these images remain complex and nontrivial to interpret. To enable further analysis, understanding and manipulation, it is appropriate to treat osteons - and more specifically their constituent lamellae - as individual, well-defined objects. This can be achieved by approximating these complex biological structures with simplified mathematical representations, such as idealized and simple geometric forms.

When processing binary images which contain relatively elongated elements - characterized by a very small thickness compared to their other characteristic dimensions, as for lamellae - skeletonization is an effective method that is commonly used to simplify such images. However, as will be demonstrated, this approach alone is not sufficient. Therefore, a more advanced protocol is developed to achieve a simplified representation of the osteon. Nevertheless, this part of the project is not entirely independent from the first one. Indeed, certain elements will reappear here to serve as a bridge between these two sections, which, although distinct, remain conceptually connected.

This chapter begins by introducing the skeletonization of binary images and the extraction of a specific feature, namely the lamellar surface. Subsequently, the protocol developed to reconstruct the osteon as a mathematical object is described in detail, followed by the presentation and discussion of the results.

It is important to understand that the term "mathematical" is not intended in the analytical sense, but rather in a figurative way, referring to a simplified geometric representation of a complex object.

4.2 Image skeletonization

In image processing, skeletonization refers to the process of iteratively thinning binary objects until a minimally connected, one-pixel-wide structure is obtained, hence referred to as the skeleton of the image.

Skeletonization can be performed using two methods: the Zhang-Suen method and the Lee method. In this project, the Zhang algorithm is used.

This method is carried out in two steps, applied iteratively until the image no longer changes. For each white pixel (*i.e.* which is assigned a value of 1), denoted as P_1, its eight neighboring pixels are analyzed - arranged as illustrated in Figure 4.1B.

Two key parameters are associated to each pixel: $N(P_1)$ represents the number of neighboring pixels with a value of 1, and $S(P_1)$ denotes the number of 0-to-1 transitions observed while iterating through the sequence of neighboring pixels in the following clockwise order: P_2, P_3, P_4, P_5, P_6, P_7, P_8, P_9, P_2.

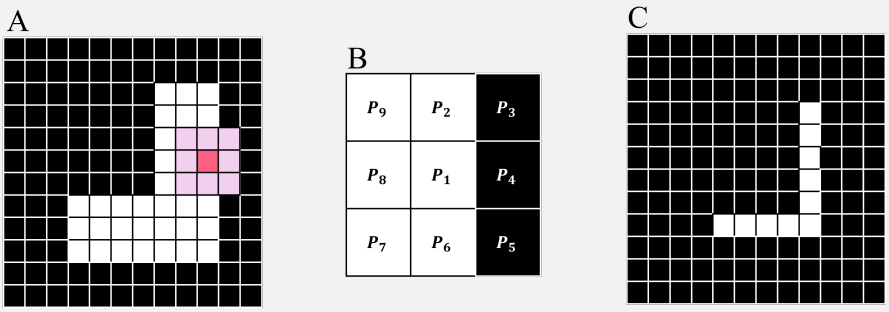


Figure 4.1: Principle of image skeletonization. **A.** Image before skeletonization. A non-zero pixel is highlighted in dark pink, with its eight neighboring pixels indicated in light pink. **B.** Magnified image of the 9 pixels of interest along with their assigned labels. **C.** Skeletonized image.

Step 1 - All non-zero pixels which have 8 neighbors are tested. Each pixel is marked if it satisfies all of the following conditions:

- $2 \leq N(P_1) \leq 6$
- $S(P_1) = 1$
- $P_2 \times P_4 \times P_8 = 0$ (*i.e.*, if at least one of these pixels is equal to 0)
- $P_4 \times P_6 \times P_8 = 0$, (*i.e.*, if at least one of these pixels is equal to 0)

After all pixels have been evaluated, the marked ones are simultaneously set to zero.

Step 2 - The remaining non-zero pixels are re-evaluated using a slightly different set of conditions. A pixel is marked if it satisfies the following:

- $2 \leq N(P_1) \leq 6$
- $S(P_1) = 1$
- $P_2 \times P_4 \times P_8 = 0$
- $P_2 \times P_6 \times P_8 = 0$

Again, the marked pixels are removed simultaneously once the entire image has been assessed.

Steps 1 and 2 are repeated iteratively until no further pixels are marked for deletion.

Skeletonization was performed exclusively to three representative slices of each osteon - namely the first, middle, and last slices of the binary image stack (from which the initial and final slices that were barely visible were discarded, as explained in Section 3.4). This choice is motivated by the fact that, in the first place, the reconstruction will be performed only on these three slices, due to the time-consuming nature of the protocol outlined below.

Exceptionally, the results of the skeletonization are presented at this stage, as the extracted skeletons of the osteons will play a central role in the following steps of this work. Figure 4.2 shows the skeleton of osteon 1 overlaid on both the raw and binarized images.

As can be observed, especially when superimposed on the binarized image (see Figure 4.2B), the skeleton closely follows the centerline of each bright band of the osteon. Consequently, the skeleton also provides a good fit to the raw image of the osteon (as shown in Figure 4.2A), making it a good morphological approximation of the osteon structure. Furthermore, the fact that the skeleton aligns well with the SHG signal suggests that both the post-processing and image segmentation yield reliable results.

The skeletons of the two other osteons are illustrated in Figures 4.3 and 4.4.

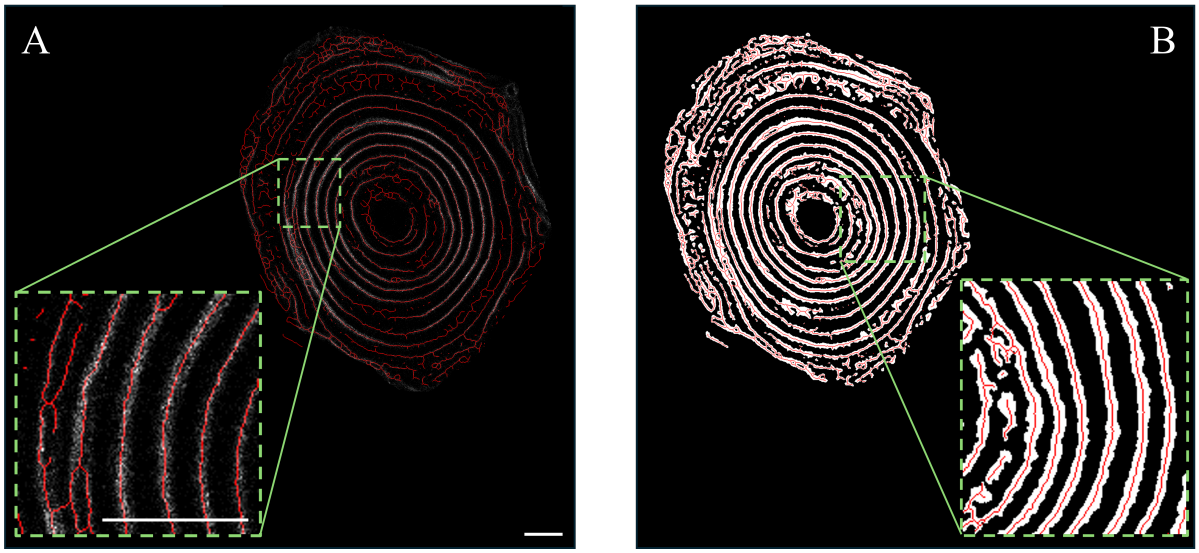


Figure 4.2: Skeleton of osteon 1 (more specifically, slice 64 out of 136). **A.** Skeleton overlaid on the raw image. **B.** Skeleton overlaid on the binarized image. Scale bars: 30 µm.

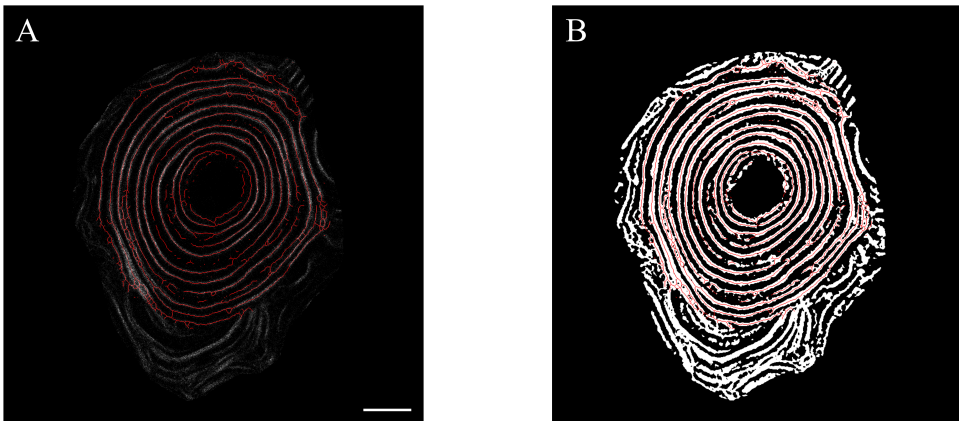


Figure 4.3: Skeleton of osteon 2 (more specifically, slice 66 out of 136). **A.** Skeleton overlaid on the raw image. **B.** Skeleton overlaid on the binarized image. Scale bar: 40 µm.

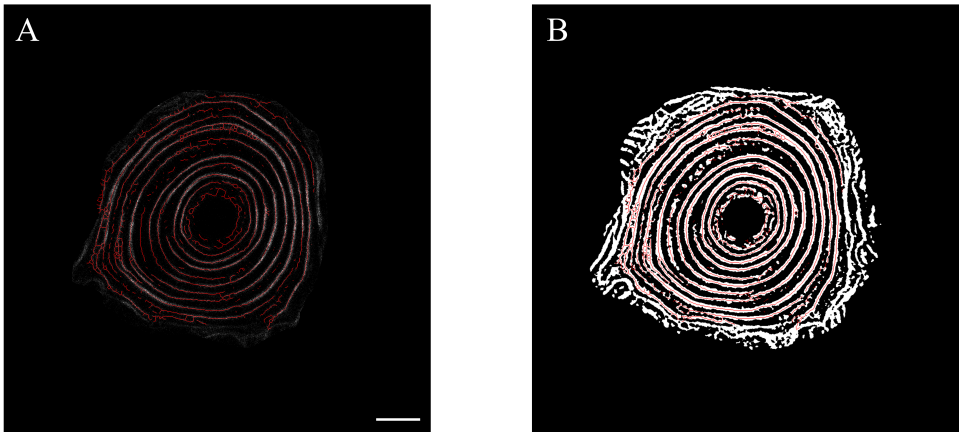


Figure 4.4: Skeleton of osteon 3 (more specifically, slice 63 out of 136). **A.** Skeleton overlaid on the raw image. **B.** Skeleton overlaid on the binarized image. Scale bar: 40 µm.

4.3 Lamellar surface area

For each osteon, the three most clearly visible innermost lamellae – defined as those exhibiting a continuous signal and a clear distinction from adjacent lamellae – were identified in the first, middle, and last slices of the binary image stack. Figure 4.5A illustrates the selected lamellae for osteon 1. In cases where a lamella forms a spiral, the lowest point of its innermost part is first identified; one full turn is then followed along the lamella, and the segment is isolated (as illustrated in Figure 4.5B). Ultimately, the two ends of the extracted lamella are manually connected with the brush tool in Fiji. Care was taken to ensure that the same lamellae were consistently selected across the three slices. Finally, the lamellae were skeletonized, and the surface area – given by the number of pixels contained within the skeleton, multiplied by the pixel area – was computed for each. These results were then analyzed and compared to extract information about the three-dimensional organization of the lamellae.

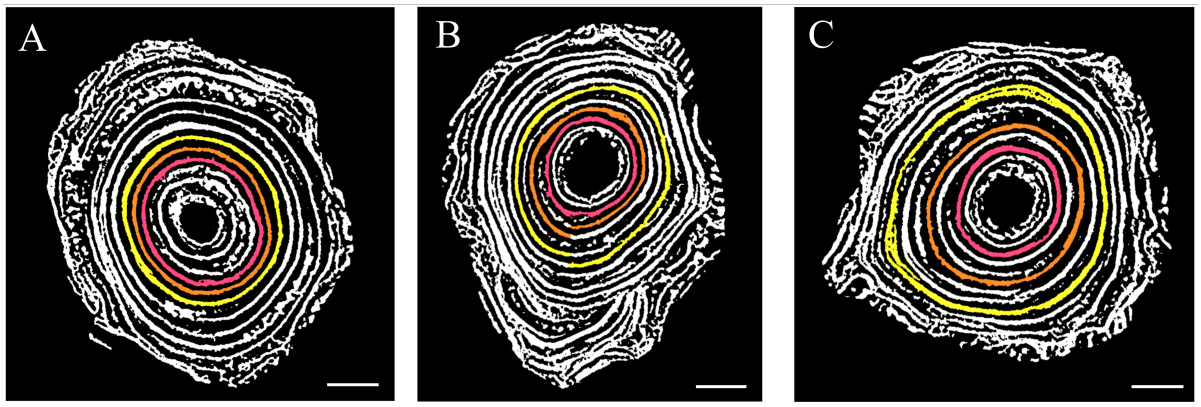


Figure 4.5: Lamellae selected for the surface calculation. For each osteon, the three most clearly visible innermost lamellae were identified. **A.** Osteon 1, **B.** Osteon 2 and **C.** Osteon 3. Scale bars: 40 µm.

4.4 Reconstruction of an osteon at specific slices

As previously mentioned, only the skeletons from the first, middle, and last slices were extracted. As was done with the raw images - both in the transverse and longitudinal planes of the osteon - the lamellae in these skeletons were, to some extent, labeled. To achieve this, the regression lines fitted to the lamellae were used. In the longitudinal plane, these lines are defined across the entire z-axis (see Figure 4.6A). Consequently, they can be evaluated at the z-positions of the slices where the skeletons were extracted, thus yielding points in the transverse plane. As six reslices of the osteon were taken, the regressions generate six lines of points - one per reslice. Each point is labeled according to its associated lamella, and because points of the same color closely follow the corresponding skeletonized lamella, this approach effectively enables their labeling (as can be observed in Figure 4.6B).

The unlabeled lamellae were removed from each skeleton, as they are not used for the reconstruction of the osteon. Subsequently, each skeleton was represented in a polar coordinate system. That means, rather than describing each pixel by its position (x, y) in the transverse plane, it was expressed in terms of polar coordinates (r, θ), where $r = \sqrt{x'^2 + y'^2}$ denotes the radial distance of the pixel from the center of the image - which defines a coordinate system (x', y') whose axes are parallel to those of (x, y). θ represents the angle between the radius and the horizontal axis. This approach is well-suited to osteons, as their circular structure suggests a simplified architectural organization, once the transformation is applied. In fact, the lamellae then appear as relatively horizontal curves, as Figure 4.6C shows. Conceptually, this can be visualized as if the osteon were cut at $\theta = 0°$ (on the right side) and then unwrapped — much like a circular elastic band that is cut and stretched out to form a straight line.

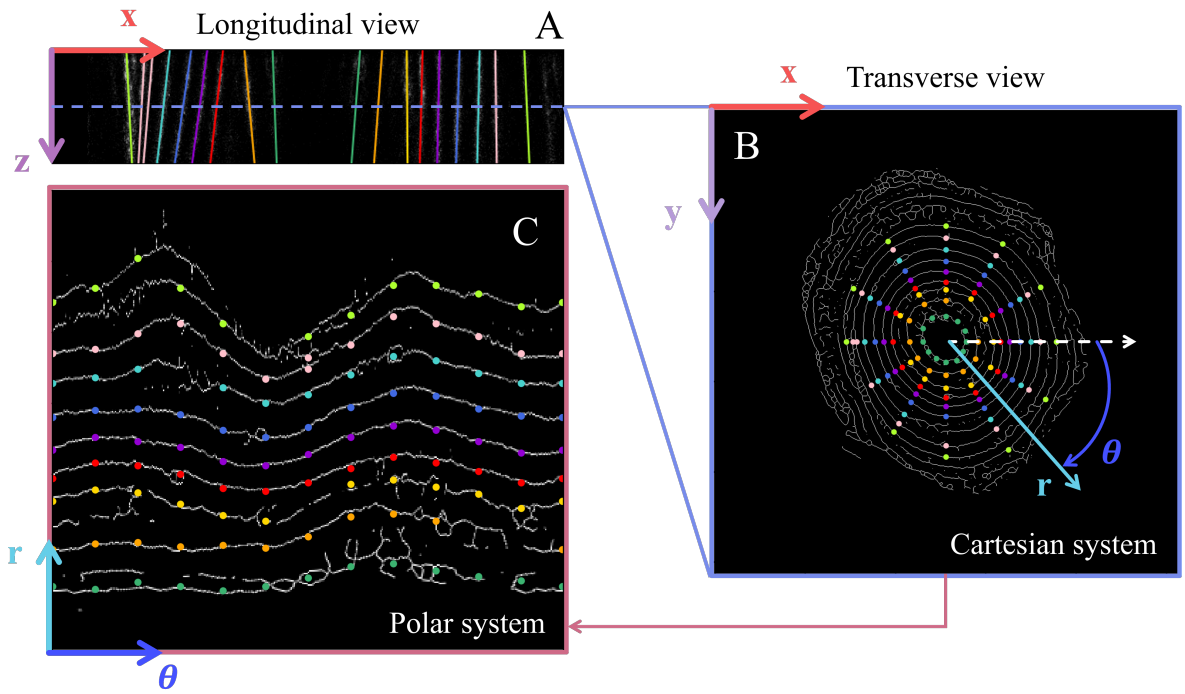


Figure 4.6: Labeling of the lamellae in the skeleton extracted at $z = 63$ pixels (middle slice) for osteon 1, and transformation from the cartesian to the polar coordinate system. **A.** Longitudinal view of the osteon (reslice at 0°) with the regression lines fitted to the lamellae. **B.** Transverse view at $z = 63$ pixels. The linear regressions - evaluated at $z = 63$ pixels - become points, enabling the labeling of lamellae within the skeleton. **C.** Image of the osteon obtained after applying the polar transformation.

From this point, the idea is to fit a smoothing spline to each lamella within the polar image of the skeleton. This process would provide a simplified representation of the osteon. To begin, the process is tried on a single lamella (see Figure 4.7A). On the one hand, due to the nature of the polar transformation, a one-to-one correspondence between pixels in the cartesian plot and those in the polar plot is not preserved. As a result, the signal becomes somehow "stretched" in the polar domain, meaning that multiple radial values r are associated with a single angular coordinate θ, for a given lamella (as shown in Figure 4.7C). However, fitting a curve to a cloud of points requires that each value of θ corresponds to a single value of r. To ensure this, only one pixel is retained per θ, with its radius defined as the average of all radii associated with that angular coordinate (as illustrated in Figure 4.7D-E).

On the other hand, it can reasonably be expected that, after fitting a smoothing spline, the pixels located at $\theta = 0°$ and $\theta = 359°$ may no longer share the same radial value, although this was the case before fitting the spline. This is due to the inherently approximate nature of a smoothing spline. To address this issue and ensure continuity, pixels defined at $\theta \in [0°, 10°]$ and $\theta \in [349°, 359°]$ were constrained to share a common radius r, defined as that of the pixel located at $\theta = 0°$ (as can be seen in Figure 4.7B). This choice is justified by the fact that this particular pixel is considered the most reliable, as it is the only one that is not distorted by the polar transformation — being the only value of θ for which exactly one pixel is defined per lamella. Finally, after empirical testing, a smoothing factor of $s = 500$ was selected to best capture the overall shape of the lamella (see the splined lamella in Figure 4.7F).

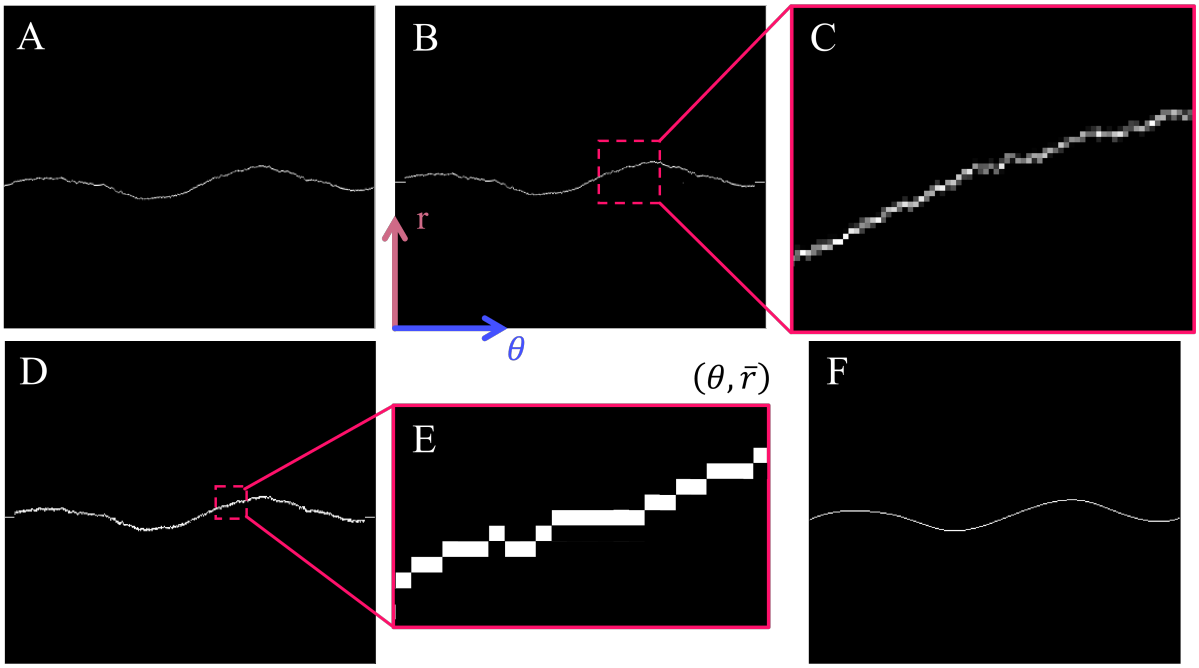


Figure 4.7: Visual representation of the steps involved in fitting a smoothing spline to an isolated lamella. **A.** Skeleton of the lamella in the polar coordinate system. **B.** Skeleton after setting equal radial values for the few first and last pixels, to ensure continuity between the starting point of a lamelle and its ending point. **C.** Magnified view showing that multiple non-zero pixels may exist for a single angular value θ. **D.** Skeleton after computing a mean radial value for each angular coordinate θ. **E.** Magnified view of **D.**. **F.** Smoothing spline fitted to the lamella.

A new challenge emerged from the fact that a single skeleton of an osteon contains multiple lamellae, and thus several datasets requiring individual spline fitting. To address this, a Python-based interface was implemented to allow the user to efficiently select lamellae. Briefly, the user clicks on a few points of the lamella of interest (as illustrated in Figure 4.8B). Based on these points, a window of predefined thickness is constructed around the selected region (see Figure 4.8C). All pixels lying outside this window are then set to 0, effectively isolating the targeted lamella (as can be seen in Figure 4.8D). Subsequently, a smoothing spline is fitted to the lamella, following the procedure previously described (as shown in Figure 4.7). To avoid confusion for the remaining lamellae, and thus facilitate the work, the approximated lamella is removed from the original skeleton (see Figure 4.8F).

Once all lamellae were processed, the last step consisted in an inverse transformation - from the polar to the cartesian coordinates - to reconstruct the osteon in its circularity at the specific slice. As a reminder, this operation was carried out for the first, middle, and last slices. Figure 4.9 illustrates the comparison between the original skeleton and its splined-approximated version of osteon 1.

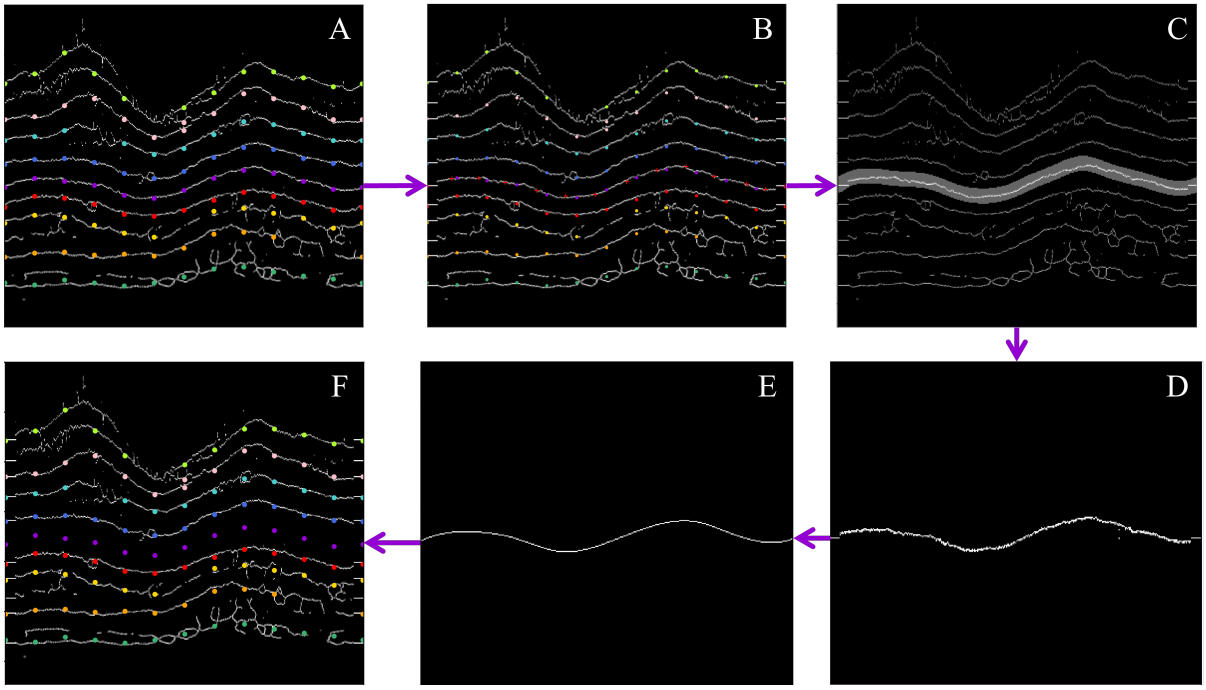


Figure 4.8: Visual representation of the steps involved in fitting a smoothing spline to each lamella of a skeleton. The process is detailed for the purple lamella. **A.** Skeleton of the lamellae in the polar coordinate system, with the points resulting from the regression lines. **B.** Points selected by the user on the lamella of interest (depicted by the red crosses). **C.** Window constructed around these points. **D.** Isolated lamella. **E.** Splined lamella. **F.** Original skeleton of the osteon without the processed lamella.

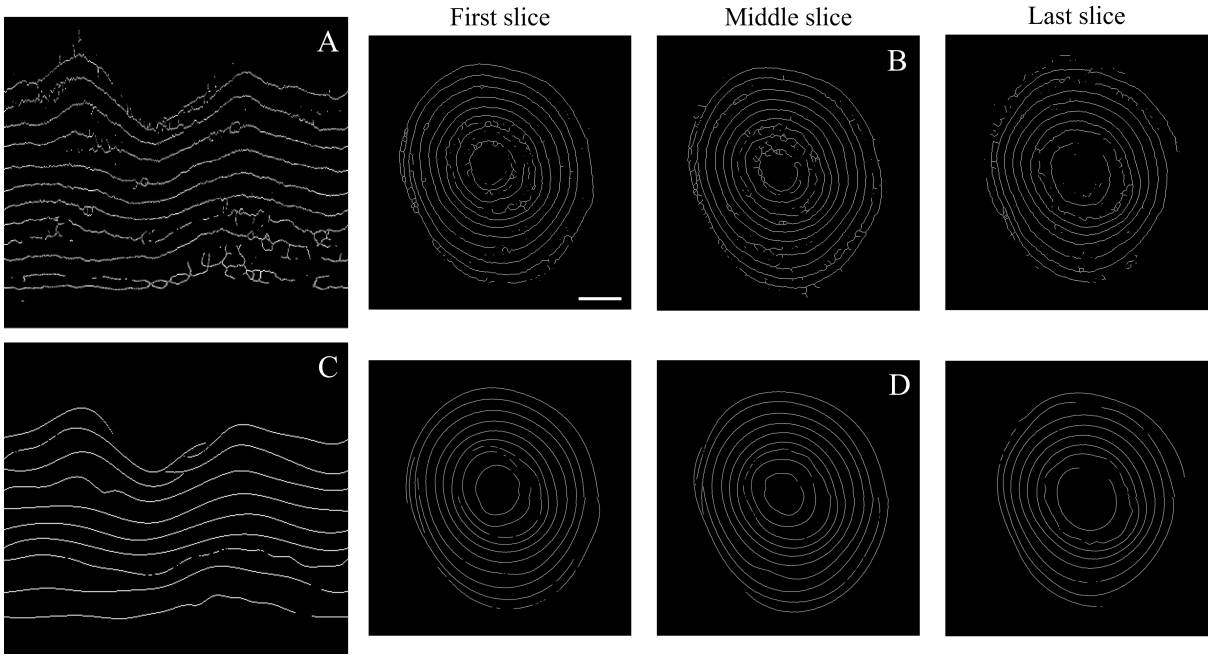


Figure 4.9: Comparison between the original skeletons of osteon 1 (first, middle and last slices) and their splined versions in both the polar and cartesian coordinate systems. **A.** Polar plot of the skeleton of the middle slice. **B.** Cartesian plot of the skeleton. **C.** Polar plot of the spline of the middle slice. **D.** Cartesian plot of the spline. Scale bar: 40 µm

4.5 Reconstruction of an entire osteon

At this stage, the objective is to fully reconstruct the osteon by leveraging all the information that was previously collected. More precisely, this involves determining the lamellar structure across all transverse slices located between the first and last ones.

As a reminder, six longitudinal reslices of the osteon were acquired, corresponding to angular orientations of the osteon ranging from 0° to 150°, in increments of 30°. These reslices allow visualization of the inner structure of the osteon along different longitudinal planes. Linear regressions were fitted to each lamella in these reslices, yielding a mathematical approximation of the lamellar architecture throughout the entire depth (z-axis), but only at discrete angular positions θ - namely 0°, 30°, 60°, 90°, 120°, and 150°. In parallel, the osteon was reconstructed as a mathematical object at three specific transverse slices of the image stack, corresponding to three distinct values of the z-coordinate. At these positions, however, the lamellar arrangement is known across all angular positions θ.

This context raises the following key question: is it possible to merge both of these information in order to predict the entire lamellar structure at any transverse slice located between the first and the last? Fundamentally, the main aim of this second part of the work is to develop a methodology that allows a comprehensive reconstruction of an osteon by combining angularly-discrete, depth-resolved data with spatially continuous, slice-specific reconstructions. This concept is further understood when visualizing Figure 4.10

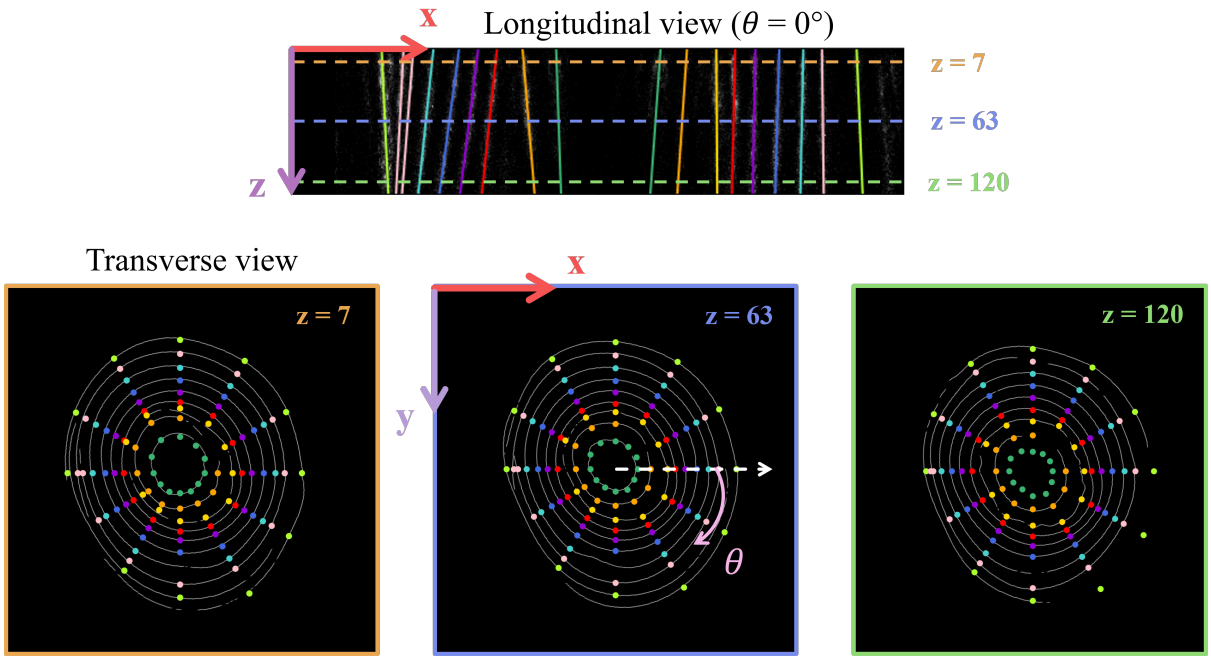


Figure 4.10: Schematic representation of the information available for osteon reconstruction. On one hand, the linear regressions provide information continuously along the z-axis, but only at discrete angular positions θ. On the other hand, the splines offer information for all values of θ, but only at three specific depths along the z-axis. The z-position are expressed in pixels.

In order to reconstruct an osteon, a systematic protocol was developed. The initial information involves the polar plots of the splines of slices between which the lamellar structure is to be predicted – namely, either the first and middle slices, or the middle and last slices. For the sake of simplicity, these two slices are hereafter referred to as the reference slices. In both, the osteon has already been reconstructed as a mathematical objet. A schematic representation of the procedure is illustrated in Figure 4.11

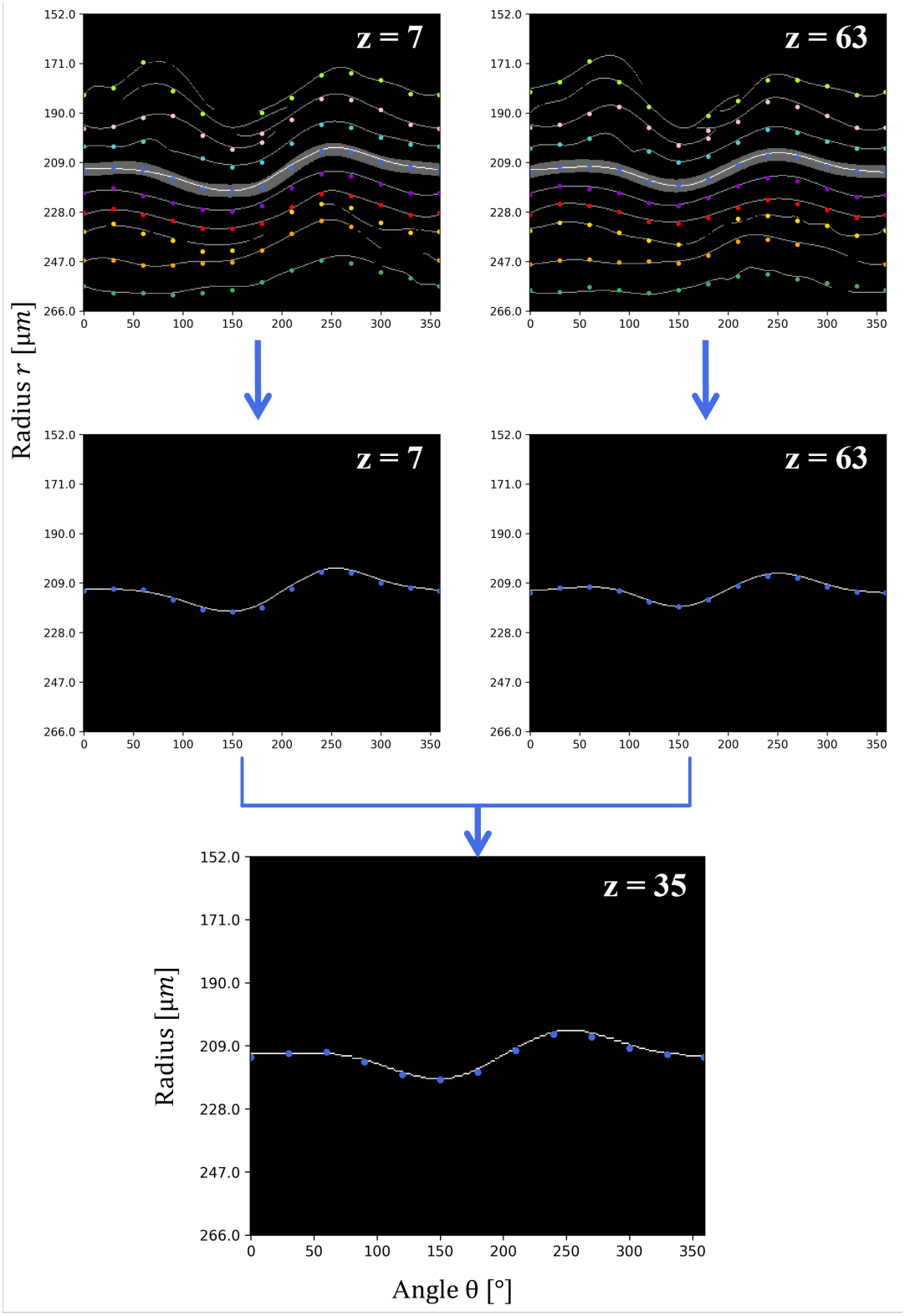


Figure 4.11: Schematic representation of the protocol implemented to reconstruct a lamella in an intermediate slice (here, $z = 35$ pixels), based on two reference slices — namely, the first slice ($z_i = 7$ pixels) and the middle one ($z_f = 63$ pixels). Starting from the polar plots of the spline-fitted versions of these slices, the blue lamella is isolated by building a window of thickness 24 pixels around the blue points, which result from the linear regressions fitted to the lamella. The intermediate lamella is then computed using Equation 1.

For each of the two reference slices, a lamella of interest is isolated. This is achieved by constructing

a window of fixed thickness (here, 24 pixels) around the lamella, based on the points - that, as a recall, result from the evaluation of linear regressions at the z-positions - which exhibit the color of the lamella. All pixels outside this window are set to zero, thereby retaining only the lamella of interest.

If the lamella is not properly isolated after this automatic isolation - for whatever reason - the user can either arbitrarily adjust the thickness of the window or proceed with manual isolation by clicking on several points of the lamella, following the approach described in Section 4.4. This manual method is particularly useful for handling spiraling lamellae, as several segments of the lamella must be isolated. In such cases, it is important to identify, in the first place, the same segment on both reference slices and isolate them individually. Only the segments present in both slices were retained for the reconstruction process. The reasoning underlying this statement will become clear as the next step of the protocol is explained.

Once the same lamella – or the same segment of a spiraling lamella – has been isolated in both reference slices, the reconstruction of that lamella at an intermediate slice can be performed. Let z denote the position in which the lamella is to be estimated. For each value of θ ranging from 0° to 359°, if a non-zero pixel is present in both reference slices – meaning the information is available in both the reference slices – the radial position r of that pixel in the intermediate slice is calculated using the following weighted sum:

$$r_z(\theta) = r_{z=z_i}(\theta) \cdot w_z + r_{z=z_f}(\theta) \cdot (1 - w_z) \tag{1}$$

where:

- $r_{z=z_i}(\theta)$ denotes the position (or radial value) of the pixel at θ in the first slice where the osteon has already been reconstructed.
- $r_{z=z_f}(\theta)$ denotes the position (or radial value) of the pixel at θ in the second slice where the osteon has already been reconstructed.
- w_z is a weight factor defined by the affine expression $w_z = \frac{z_f - z}{z_f - z_i}$. Conceptually, this weight can be understood as a similarity factor: the closer z is to z_i, the more w_z tends to 1, thus forcing the interpolated lamella to resemble that of the first slice. In contrast, as z approaches z_f, the interpolated lamella increasingly resembles that of the second slice.

However, at this stage, the information derived from the linear regressions has not yet been explicitly incorporated into the reconstruction of the lamella. According to the example illustrated in Figure 4.11, the blue points (which can be seen close to the intermediate lamella in Figure 4.12A) remain unused. To ensure a balanced contribution from the intermediate lamella (depicted by the white line, reconstructed at $z = 35$ pixels) and the blue points, a simple approach consists in sampling the intermediate lamella at intermediate angular positions θ that lie between those of the blue points. In other words, the intermediate lamella is sampled at $\theta \in \{15°, 45°, 75°, 105°, ..., 315°, 345°\}$. These samples are illustrated as red points in Figure 4.12B, which are therefore simply points that belong to the white spline.

The combination of the red points sampled from the intermediate lamella and the blue points resulting from the linear regressions forms a new dataset onto which a final smoothing spline was fitted. To prevent overfitting of the curve on the data points - which could lead to abrupt and inconsistent variations of the spline - a low smoothing factor of 50 was used. The resulting lamella, which is the final version of the intermediate lamella, can be visualized in Figure 4.12C.

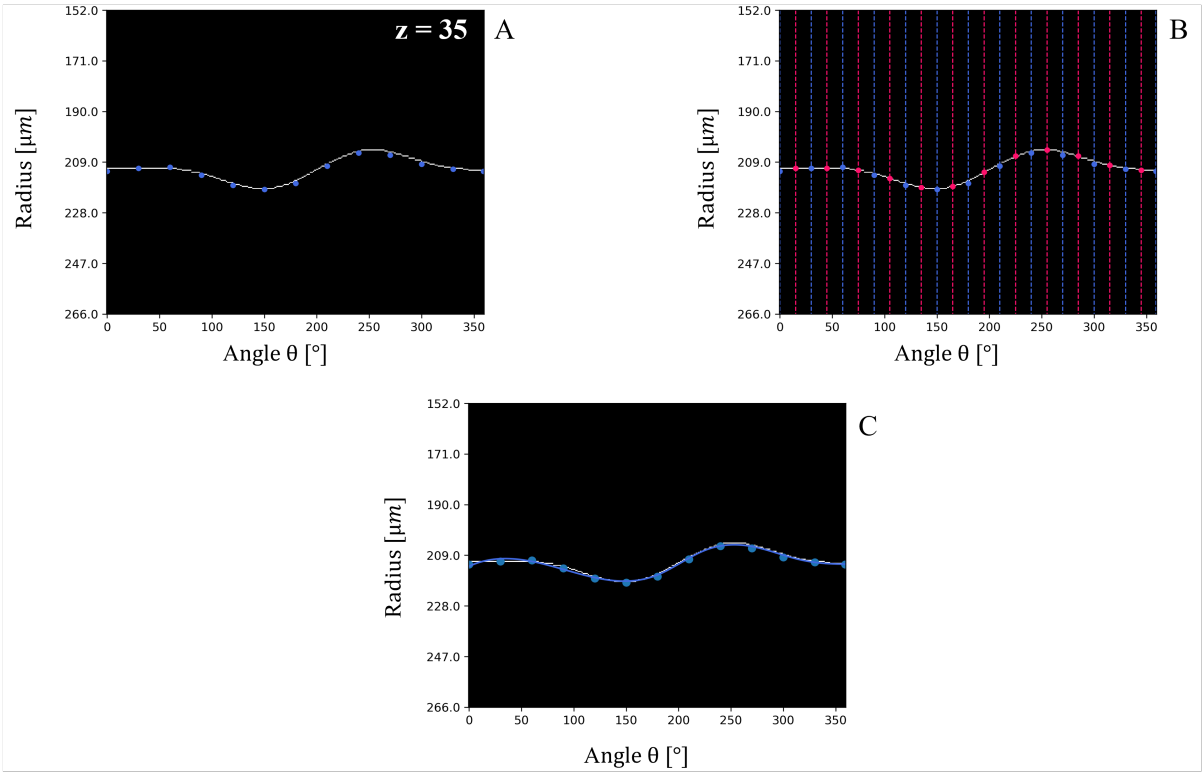


Figure 4.12: Schematic representation of the protocol implemented to reconstruct the final lamella in an intermediate slice (here, $z = 35$ pixels), using the information resulting from the linear regressions (blue points). **A.** Intermediate lamella computed using Equation 1 and points resulting from the evaluation of the regression lines in the longitudinal view, at $z = 35$ pixels. **B.** Red points are sampled from the intermediate lamella (reconstructed through the weighted sum) at intermediate angular positions. **C.** The blue curve depicts the final lamella, obtained by fitting a smoothing spline on the dataset composed of the blue and red points.

Ultimately, this protocol was iteratively applied to each lamella of the osteon. Once all intermediate slices had been reconstructed, an inverse transformation — from the polar to the cartesian coordinate system — was performed, yielding the complete reconstruction of the osteon.

4.6 Interlamellar thickness

An additional morphological characteristic of the osteon, referred to as the interlamellar thickness, was computed and analyzed. This thickness is defined as the distance between the midlines of two consecutive bright lamellar bands of the osteon. In the context of this work, it was approximated by the distance between two successive splines within the same slice of the osteon. This method is applied only to the three reference slices - namely the first, middle and last slices of the binary image stack - which were manually reconstructed.

Figure 4.13 illustrates how this thickness was defined and computed. At each value of θ, the interlamellar thickness corresponds to the difference in radial position r between the two lamellae (depicted by the violet double-arrows). Two important considerations apply:

- If, for a given θ, one of the two lamellae is not defined, the thickness is not computed. It is the case in the region delimited by the dashed red lines.
- If the lamella forms a spiral, the interlamellar thickness is given by the distance between one lamella and the nearest segment of the spiraling lamella. Moreover, an additional thickness is computed between a given lamellar segment and its adjacent counterpart (as illustrated by the

blue dashed double-arrow). In the figures presented in the results section, this additional thickness is visually distinguished from the primary one.

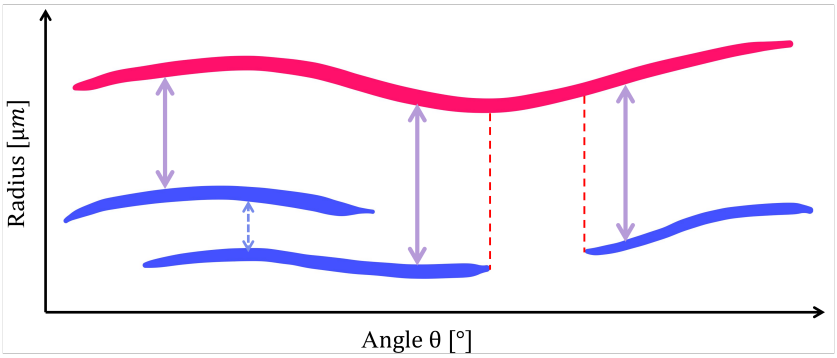


Figure 4.13: Schematic representation of how the interlamellar thickness is computed between two lamellae (here, illustrated by the red and blue splines - with the blue one corresponding to a spiraling lamella), in the polar coordinate system.

4.7 Results and discussion

A) Lamellar surface area

The histogram shown in Figure 4.14 displays the lamellar area of the three most clearly visible innermost lamellae of osteon 1. For each lamella, three bars exhibiting the same color can be observed, corresponding respectively to the first, middle, and last slices where the surface area was computed - refer to Figure 4.5A.

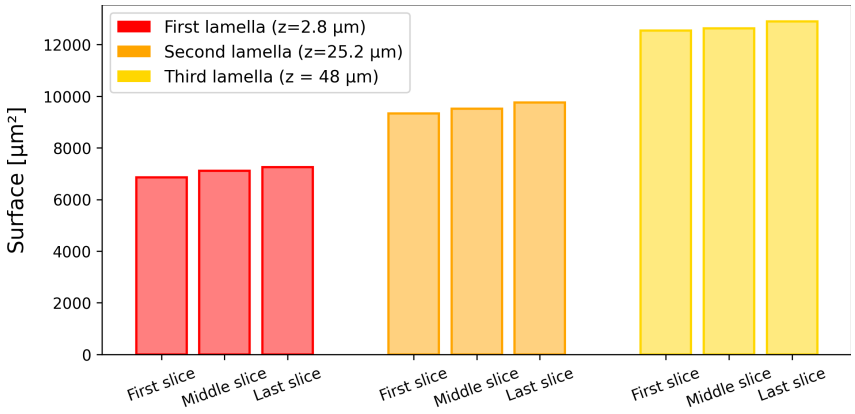


Figure 4.14: Histograms displaying the lamellar surface areas of the three most distinguishable innermost lamellae of osteon 1. Each group of three bars corresponds to one lamella, with its associated color indicated in Figure 4.5A.

Firstly, as expected, the lamellar surface increases from the red lamella to the orange one, and from the orange to the yellow one, as one progressively moves towards the periphery of the osteon. Table 2 reports the percentage increase in lamellar surface from the innermost lamella to the outermost, in the three different slices. In this osteon, the radial increase in surface area between adjacent lamellae appears to be consistent, with an approximate increase of 33% observed regardless of the slice of interest. We can also note that these lamellae belong to the intermediate region located between the Haversian canal and the cement line – specifically the red, purple and blue lamellae visible in the transverse view of Figure 3.16. As stated before, this consistency in lamellar surface growth may be due to a higher degree of structural organization in this region, suggesting that adjacent lamellae are regularly arranged and morphologically similar.

	From first to second lamella	From second to third lamella
First slice	35.92%	34.37%
Middle slice	33.81%	32.59%
Last slice	34.41%	32.24%

Table 2: Percentage increase in lamellar surface area from the innermost to the outermost lamella, within a given slice of osteon 1.

Similarly, the evolution of the surface area of a given lamella across the different slices can be investigated, to have insights about osteon's conicity. In the histogram, this corresponds to comparing bars of the same color. We can easily observe that the surface area of a given lamella increases gradually with depth within the osteon. This supports the hypothesis of lamellar conicity, which was introduced in the first part of this project (see Subsection 3.9 D), where these specific lamellae exhibit a widening pattern along the osteon's longitudinal axis. Table 3 summarizes the percentage increase of each considered lamella in between the different slices. Although the magnitude of this increase remains comparable for all lamellae, it does not exhibit the same level of consistency as in Table 2.

It is important to note that a single reslice, does not allow to predict the global evolution of the lamellar structure. Depending on the reslicing plane, a lamella may appear to widen or shrink, as illustrated in Figure 3.24. In contrast, our analysis provides a comprehensive evaluation of the lamellar evolution along the depth of the osteon.

	From first to middle slice	From middle to last slice
First lamella	3.68%	1.98%
Second lamella	2.07%	2.44%
Third lamella	0.71%	2.17%

Table 3: Percentage increase in surface area of a given lamella, over the different slices of osteon 1.

The histograms associated with the other two osteons can be visualized in Figures 4.15 and 4.16. While osteon 3 displays similar results as for osteon 1, the results for osteon 2 appear more unexpected. First, the surface areas of the red and orange lamellae appear to decrease before increasing. However, given that these variations are close to 1%, they may result from the processes involved in the transformation of raw images into their skeletonized version. These minor fluctuations may therefore be either too small and not reflect actual morphological changes, or stem from inherent biological variability. In contrast, the yellow lamella exhibits a steadily decreasing surface area. Yet, since all osteons were imaged in the same orientation, these observations suggest that lamellae are conical in shape, with their apex oriented either toward the cortical surface which is imaged, or toward the other direction. This hypothesis, however, is based on the assumption that the Haversian canal is approximately perpendicular to the cortical surface - which has been adopted throughout this study. Furthermore, the directionality of the cone could indicate the direction of lamellar formation. As illustrated in Figure 1.11, lamellae are believed to form in the direction corresponding to an increasing cross-sectional lamellar surface, formed by the closing cone.

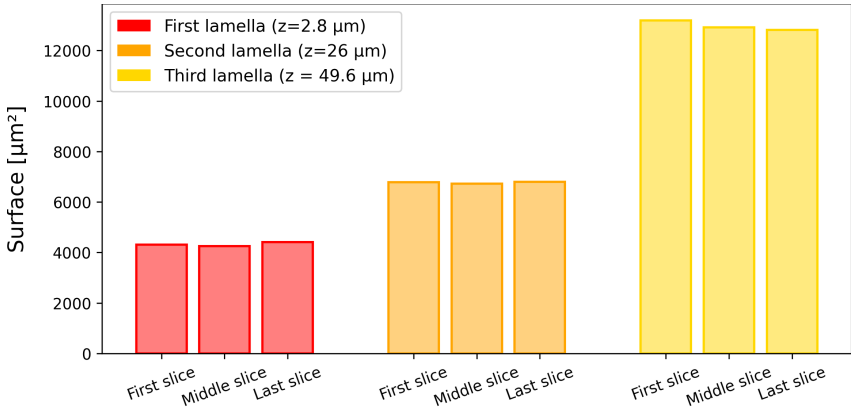


Figure 4.15: Histograms displaying the lamellar surface areas of the three most distinguishable innermost lamellae of osteon 2. Each group of three bars corresponds to one lamella, with its associated color indicated in Figure 4.5B.

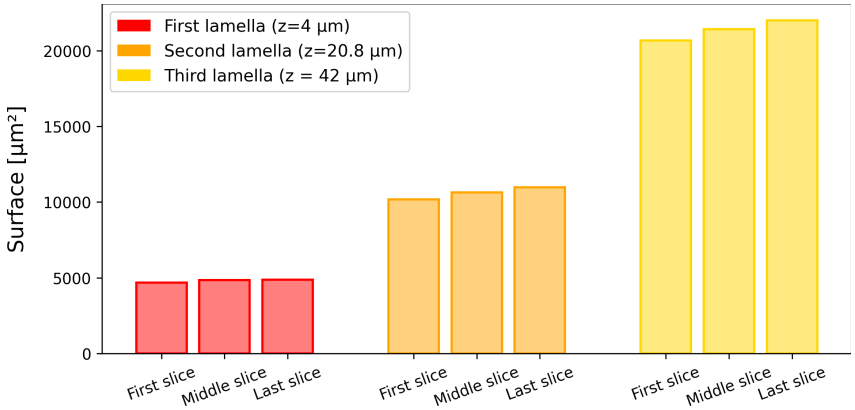


Figure 4.16: Histograms displaying the lamellar surface areas of the three most distinguishable innermost lamellae of osteon 3. Each group of three bars corresponds to one lamellae, with its associated color indicated in Figure 4.5C.

Finally, it is worth noting that our results remain plausible from a quantitative point of view. The Haversian canal typically exhibits a diameter of approximately 50 µm, corresponding to a cross-sectional area of roughly 1960 µm² (assuming that the cross-section is a perfect circle). Assuming similarly idealized circular shapes for the lamellae, their diameters range from 94 to 128 µm (for osteon 1).

B) Reconstruction of an entire osteon

Figure 4.17 illustrates five reconstructed slices of osteon 1. The mathematical representation of the osteon, shown in red, is superimposed on the corresponding raw image slice.

Among the 114 reconstructed slices, five are displayed here. These include the three slices that were manually reconstructed following the protocol described in Section 4.4 - namely the first, middle, and last slices of the binary image stack - as well as two intermediate slices reconstructed according to the method detailed in Section 4.5. For each slice, the corresponding depth z (in pixels) is indicated. Several comments can be made.

We begin with the examination of the three manually estimated slices, located at $z \in \{7, 63, 120\}$ pixels. Notably, the osteon could be successfully reconstructed in both the first and last slices, despite the low SHG signal observed in the corresponding raw images. This reconstruction was made possible through post-processing techniques aimed at enhancing the contrast between bright and dark bands, followed by binarization via segmentation. The resulting mathematical object aligns almost perfectly with the

raw SHG signal, indicating that our reconstruction model provides an accurate approximation of the lamellae. Moreover, as we aimed to achieve, the mathematical approximation of the osteon offers a simpler and more interpretable depiction than the skeleton of the osteon. It is worth noting, however, that certain regions (as indicated in Figure 4.17A) are more accurately approximated than others (see Figure 4.17B). Nevertheless, the estimated signal remains closely aligned with the raw data.

Given that the manual reconstruction of lamellae at each slice is highly time-consuming, a semi-automatic methodology, outlined in the sections above, was implemented to estimate the lamellar structure at any depth z. The slices at $z = 35$ and $z = 91$ pixels are two illustrative examples of the application of this approach. As with the reference slices discussed in the previous paragraph, the lamellae reconstructed in some regions (see Figure 4.17C) appear to more accurately approximate the raw SHG signal than in others (such as in Figure 4.17D). These discrepancies may arise from the image processing steps, segmentation, or simply the inherent approximate nature of the reconstruction technique itself - for instance, and in particular, the use of smoothing splines. On the other hand, it can happen, although infrequently, that reconstruction artifacts appear in certain regions of the osteon (as can be observed in Figure 4.17E). In such areas, the reconstructed object slightly deviates from the underlying signal, resulting in geometries that may appear implausible. We hypothesize that these defects are artifacts induced by the fitting of the intermediate lamella through points resulting from linear regressions. In particular, in the case of a spiraling lamella, a segment may deviate because it is forced to fit a linear regression point located on an adjacent segment of that lamella.

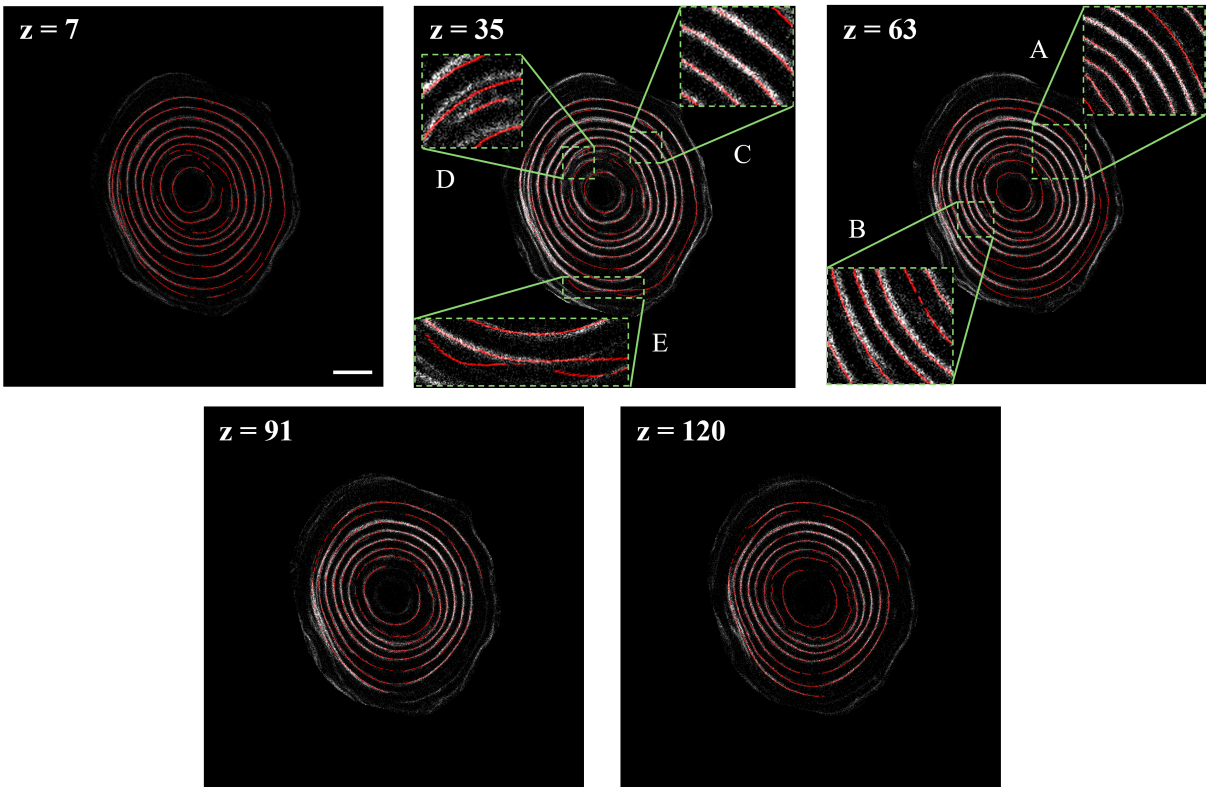


Figure 4.17: Osteon 1 represented as a mathematical object. The mathematical reconstruction is shown in red, superimposed on the raw background image. Only 5 out of 114 slices are displayed, with the corresponding depth (in pixels) indicated on each slice. The slices at $z = 7$, $z = 63$, and $z = 120$ pixels were manually reconstructed, as described in Section 4.4, while the remaining two were estimated using the protocol detailed in Section 4.5. Regions **A** and **C** highlight areas where the reconstruction closely approximates the raw SHG signal, whereas regions **B** and **D** illustrate areas where the estimated signal shows reduced fitting to the original signal. Region **E** displays an area where reconstruction artifacts are present. Scale bar: 40 µm.

Finally, it should be noted that between the middle and the last slices, several segments of certain lamel-

lae - particularly the innermost lamella - were not reconstructed, despite the presence of a SHG signal in the raw images. This limitation is directly attributed to the formulation given in equation 1. Indeed, as previously mentioned, the radial position r of a pixel located at a given angular coordinate θ is computed only if corresponding pixels exist in both reference slices at that same angular position. Since some pixels are absent in the last slice (at $z = 120$ pixels), it becomes impossible, within the framework of our model, to estimate the corresponding pixel positions for depths between $z = 63$ and $z = 120$ pixels. In other words, a lamella segment cannot be reconstructed if the required information is missing from one of the two reference slices. The results of the reconstruction of osteons 2 and 3 are presented in Figures 4.18 and 4.19.

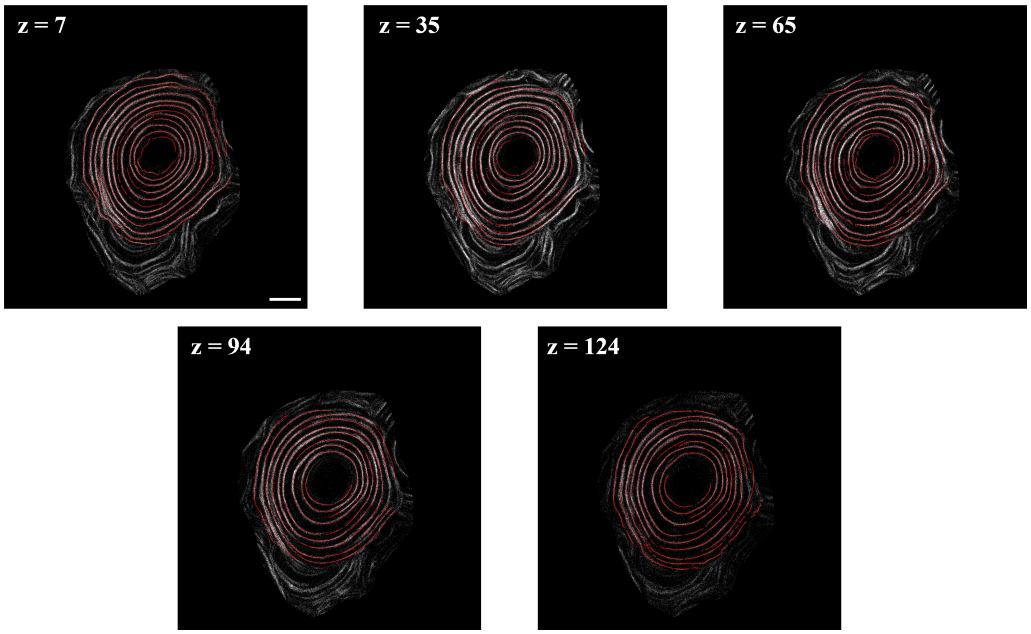


Figure 4.18: Osteon 2 represented as a mathematical object. Scale bar: 40 µm.

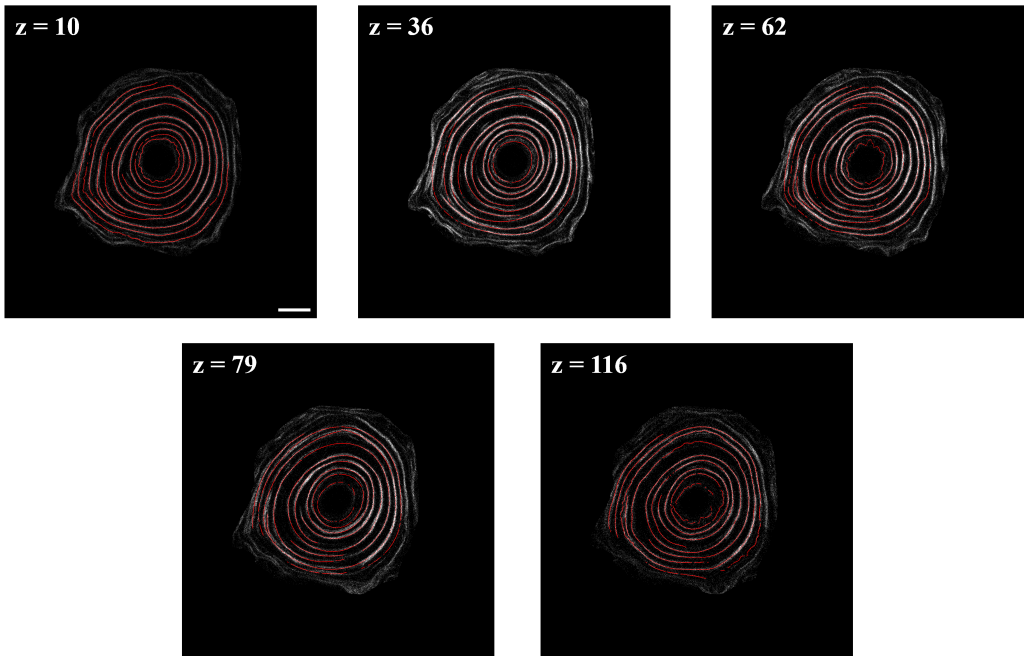


Figure 4.19: Osteon 3 represented as a mathematical object. Scale bar: 40 µm.

Figure 4.20 illustrates the three complete osteons, reconstructed as three-dimensional discrete objects. These images were obtained by superimposing all the reconstructed slices using the CTvox software.



Figure 4.20: All three complete osteons, reconstructed as three-dimensional mathematical objects.

C) Interlamellar thickness

Figures 4.21, 4.22, 4.23 illustrate the interlamellar thickness measurements for the lamellae of the first, middle, and last slices, respectively. Each figure displays several curves, corresponding to the thickness profiles between successive pairs of adjacent lamellae. These measurements are computed from the innermost lamella to the outermost lamella, with a grayscale gradient ranging from light gray to black to indicate the progression. For each slice, a visual representation of the osteon cross-section is provided, where the lamellae are color-coded to match the corresponding thickness curves. Each lamella exhibits the color of the curve that represents the thickness between it and the next outer lamella. Consequently, the outermost lamella is depicted with a dashed line, as there is no outer layer. The red curves represent the thickness between two adjacent segments of a spiraling lamella.

Firstly, no clear pattern emerges from the curves, suggesting that lamellae evolve quite differently in the radial distribution as the angular coordinate is spanned.

Secondly, within each slice, the intermediate lamellae — that is, those located at mid-radial positions — tend to exhibit relatively smooth and consistent thickness profiles compared to the innermost and outermost lamellae. Furthermore, they all appear to display a thickness close to 8 µm. Once again, this supports the hypothesis that lamellae located neither too close to the Haversian canal nor too close to the cement line possess a higher degree of structural organization. From this perspective, the red, purple, blue, and turquoise lamellae appear to be the most structurally organized and similar to each other.

Finally, the presence of bumps can be observed, particularly in the last curve of Figure 4.22. This phenomenon is attributed to the fact that, in the presence of a spiraling lamella, the innermost segment of a lamella is not defined across all angular positions. When one pixel is missing at a given angular value θ, the thickness is computed relative to the outer adjacent segment, which is by definition located further away from the intended reference lamella.

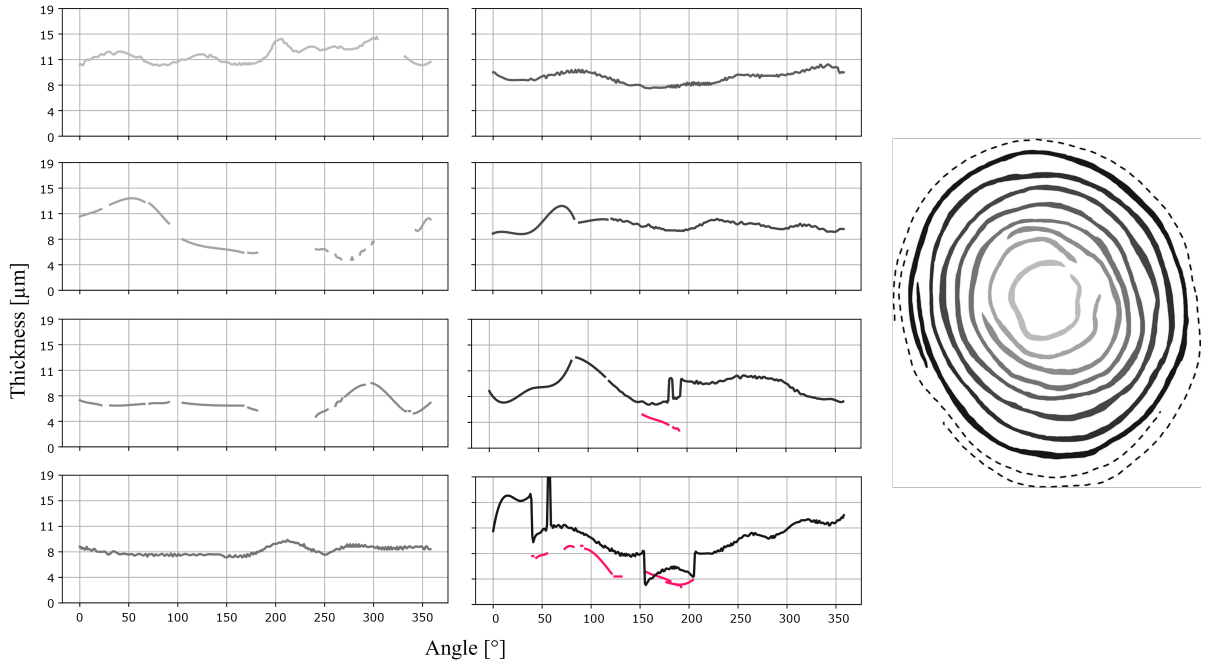


Figure 4.21: Measurements of the interlamellar thickness for the first slice of osteon 1. A visual representation of the cross-section is provided to enable matching between the lamellae and the plotted curves. Each lamella is color-coded according to the curve that displays the thickness between it and the next outer lamella. As one moves toward the cement line, the curves progressively darken, reflecting the increasing radial position. The red curves represent the thickness between two adjacent segments of a spiraling lamella.

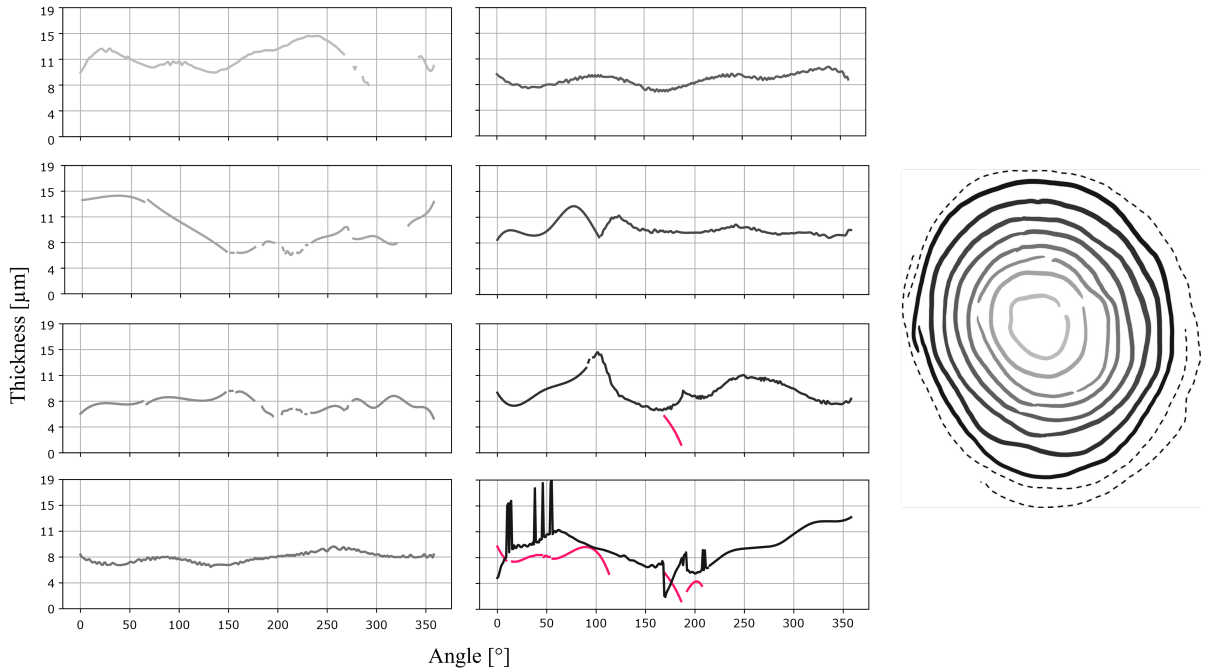


Figure 4.22: Measurements of the interlamellar thickness for the middle slice of osteon 1.

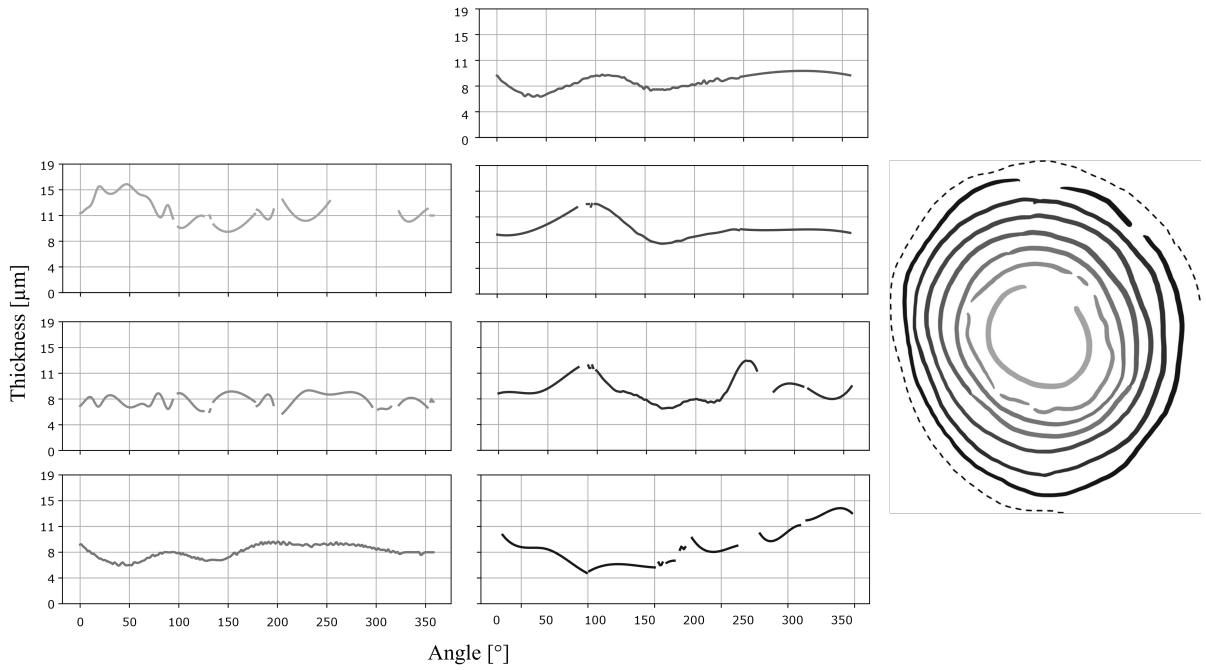


Figure 4.23: Measurements of the interlamellar thickness for the last slice of osteon 1.

One noteworthy aspect we would like to mention is the fact that, based on the polar plot — that is, the profile $r(\theta)$ — it is possible to derive the curvature profile $\kappa(\theta) = \frac{1}{r(\theta)}$ of each lamella. As can be observed in Figure 4.11 (specifically, in the two upper slices), the radius - and thus the curvature - appears to vary with the angular position. Notably, the interlamellar thickness profiles sometimes exhibit local maxima around angular positions that align with the major axis of the elliptical shape of osteon 1, approximately located at $\theta = 80°$ and $\theta = 260°$. These observations suggests that the lamellar curvature may influence the local rate of bone matrix deposition. Specifically, a higher curvature might be associated with increased osteoid secretion, as reflected by an increase in interlamellar thickness. This interpretation is consistent with findings from previous studies (Alias and Buenzli, 2017; Alias and Buenzli, 2018; Hegarty-Cremer et al., 2021; Pilia et al., 2013), which identified increased osteoblast density in regions associated with higher curvature. Therefore, the higher the amount of osteoids deposited, the thicker the lamella. While such trends are not systematically evident and true across all plots, and may not always be of sufficient importance, this hypothesis offers an interesting perspective that deserves further investigation.

This additional analysis, carried out after the main objective of reconstructing the osteon as a mathematical object, was performed only on the first osteon. Due to time constraints, it could not be extended to the other two. Nevertheless, the results obtained, along with the observations and reflections they led to, are promising and open up interesting opportunities for future investigations.

Chapter 5

Perspectives

This final chapter aims to discuss the limitations of the present work and outlines the potential improvements and directions for future projects.

5.1 Limitations

Despite the promising results obtained by applying the methodologies that we implemented, several delicate aspects must be addressed. In this section, we discuss them individually, in relation to the corresponding parts of the work.

Overall, the methods developed in this work were not applied to all lamellae within each osteon. Indeed, lamellae located near the cement line exhibit quite different structural features relative to those analyzed in this project. These peripheral lamellae lack the regularity and interpretability observed in internal ones and, more importantly, they are not consistently defined throughout the entire depth of the SHG image stack.

A) Experimental protocol
As described in Section 2.1, the sample underwent a series of experimental steps prior to imaging. Some of these procedures were not specifically intended for the acquisition of SHG images, but were performed because the sample was simultaneously imaged using other techniques (notably CLSM). Resin embedding requires dehydration of the sample, a process that has been shown to potentially alter the molecular structure of collagen fibers, affecting their cross-linking density (Wess and Orgel, 2000; Liu et al., 2023). Consequently, the SHG signal may be influenced as well, which may not reflect the native state of collagen fibers. Perhaps it would have been more appropriate to acquire images of a non-embedded sample, although embedding significantly facilitates and improves the polishing process, which in turn enhances SHG image quality. This is a trade-off that requires further investigation.

B) Collagen fiber orientation
In this study, we interpreted the SHG signal in a specific manner. As previously stated, a bright signal would indicate an orientation parallel to the imaging plane, whereas a dark signal would reflect a different orientation. No further assumptions were made. To assess which type of model should be considered to enhance the interpretability of the SHG signal (as discussed in Subsection 1.1.4 D), a promising approach would be the use of FIB SEM, which enables direct observation of fiber orientation. Comparing the resulting images with those obtained from SHG could provide valuable insights.

An alternative approach that aims to characterize the fiber orientation could be based on a previous study employing a variant of SHG microscopy, called polarized-SHG (Müller, 2009). From the acquired images, several parameters are extracted — namely the second-order susceptibility ratio, the fibril distribution asymmetry, and the weighted-average fibril orientation — from which the organization of collagen fibers can be inferred, allowing for a three-dimensional reconstruction of these fibers within the lamellae.

C) Image post-processing and segmentation
The image processing techniques used in this thesis are limited in number compared to the wide range of existing methods. Here, we only used two techniques, although others were tested and proved to be ineffective. It is quite evident that, as each method involves multiple parameters, the space of possible combinations expands rapidly, making the process time-consuming. Ideally, a more comprehensive exploration of alternative approaches should be conducted.

Regarding segmentation performed on Dragonfly, several comments can be made. First, the method involves a certain degree of subjectivity, as the user must manually segment several frames. Depending

on how the user interprets the bright or dark signals, the result may vary. While post-processing of the images did enhance contrast, some level of subjectivity nonetheless remains. In addition, several training models are available. In this study, a specific type of the U-Net architecture was used, but it would be beneficial to compare the resulting binary images with those produced by different models - whether by using other architectures or parameters. It should also be noted that some models require more training time than others.

In any case, it would also have been interesting to assess the performance of image processing and segmentation procedures using quantitative criteria. In this study, however, we relied solely on a visual inspection to select among various candidate combinations of processing steps and segmentation models.

Naturally, the skeletonization process is also influenced by the image processing techniques described above. As a result, the reconstruction of the osteon as a mathematical object is inherently dependent on these methods. A priori, the definition of what one could consider as an "effective process" is context-dependent and should be guided by the intended use of the resulting data.

D) Osteon centering

To achieve consistent reslicing at different angles, the osteon was centered within the transverse image. As detailed in Section 3.4, the applied shift was determined based on the first clearly visible lamella near the Haversian canal, and only across five slices of the binary image stack. The average x and y coordinates of the center of mass should be computed across all slices, while also considering multiple clearly identifiable lamellae. However, this process would be time-consuming as each lamella must be individually isolated to calculate its center of mass, which is further complicated by the fact that the osteon is not perfectly perpendicular to the imaging plane. And due to this tilting, the osteon is not intersected exactly through its center along the entire depth of the stack - comparable to slicing the Leaning Tower of Pisa using vertical planes.

E) Osteon reslicing

Given that the SHG images have dimensions of 1024×1024 pixels, and that the reslicing is performed at position $y = 512$ pixels - where the global center of mass of the osteon is assumed to be located - it is evident that obtaining a reslice precisely at the midpoint of the osteon volume is not feasible. Indeed, from a computational aspect, reslicing involves the extraction of a matrix from a volume along a plane different from the imaging plane. Since the image dimensions are even, the y-position of the extracted matrix cannot exactly coincide with the center between $y = 0$ and $y = 1023$ pixels. This is illustrated in Figure 5.1, where a volume of size $6 \times 6 \times 6$ is illustrated as an example: only the pink or blue matrices can be extracted, neither of which are precisely located at the central y-position. Although this limitation is unlikely to have a significant impact on our results, it is nonetheless worth mentioning.

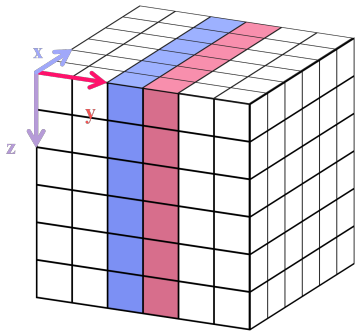


Figure 5.1: Schematic visualization of how reslicing is performed on a volume of low and even size ($6 \times 6 \times 6$). Each cube represents a voxel. As can be seen, the reslice cannot be taken exactly in the midpoint of the y-coordinate. Only the pink or blue matrices can be extracted.

Moreover, reslicing was performed at specific angular positions – ranging from 0° to 150° in increment

of 30° - due to the fact that, to fit a linear regression to each lamella, the latter must be isolated. Given that approximately twenty lamellae are present in each reslice, our manual process does not allow for the extraction of a higher number of reslices. Furthermore, the color coding of lamellae was performed manually as well, using a simple brush. In the future, it would be useful to automate these steps.

Increasing the number of reslices would enable a more comprehensive characterization of the three-dimensional structure of the lamellae - particularly by fully reconstructing the plot of the lamellar angle as a function of the osteon rotation angle (recall Figure 3.26, where points of the same color were simply connected by straight lines). Furthermore, it would facilitate the direct reconstruction of the osteon as a mathematical object. Indeed, if each regression line yields a point when evaluated at a given depth, then increasing the number of reslices also increases the number of points for a given lamella. A two-dimensional spline can then be fitted to these points to reconstruct a lamella.

F) Reconstruction of an entire osteon as a mathematical object

Our reconstruction protocol, which aims to approximate each lamella (or lamellar segment) at specific slices, is only semi-automatic, as it requires user intervention. Ideally, a more automated approach could be implemented, to enable the reconstruction of each lamella at every slice of the skeletonized image stack. This would suppress the need to estimate lamellae in intermediate slices between two reference slices.

In any case, a couple of aspects of our methodology could be improved. Firstly, it would be beneficial to address the fact that when structural information is missing from one of the reference slices, it is not possible to reconstruct the corresponding portion of the lamella in intermediate slices. Intuitively, one may understand that selecting the first reference slice deeper and the last one more superficial enhances lamellar visibility in the binary images. This leads to greater information, improving the reconstruction of the osteon in intermediate slices. At this stage, a compromise must be made between reconstructing the osteon over a larger depth - while accepting the presence of some missing lamellar segments - and reconstructing it over a smaller depth, but with more complete structural content in each slice. Secondly, several exceptional cases were handled to preserve consistency of the reconstructed object with the raw SHG signal — such as spiraling lamellae. However, certain cases remain unresolved. Beyond general reconstruction artifacts, a particular example is illustrated in Figure 4.11, specifically in slices located in $z = 7$ (first slice) and $z = 63$ pixels (middle slice). When observing the outermost lamella (labeled in light green), the rightmost segment at $z = 7$ pixels is located above the central segment, whereas the opposite configuration is observed at $z = 63$ pixels. Applying our current protocol results in a lamella which exhibits implausible geometric deformation. To address this, we simply considered the two segments as a single structure and computed their average radial values over the overlapping region. Nevertheless, it would be desirable to develop an alternative solution to such cases.

G) Use of AI in this work

Although this does not strictly fall under the scope of limitations, we mention here the ways in which AI was used. ChatGPT was used to rephrase certain sentences, particularly in cases of excessive repetitions or when a more academic formulation was required. It was also used for translating specific expressions from French to English, as well as for generating high-quality plots (notably histograms). Ultimately, it proved useful for clarifying the role of the different components of the SHG setup. Github Copilot was used to support the implementation of Python codes. Nevertheless, a critical perspective was maintained throughout this process. AI was used as a tool, and not as a driving force behind the technical or intellectual aspects of this work.

5.2 Future work

The work presented in this master's thesis is relatively novel and, as such, opens up new avenues for further research. In this section, we outline some directions that could be pursued, whether they involve direct extensions of the current work or explore more distant yet related topics.

First, we could apply our methodologies to a larger dataset of osteons to evaluate the reproducibility of our results and observations. However, this would require considering other types of osteons, with more complex morphologies and three-dimensional orientations. In the context of this study, the focus was limited to circular osteons which were approximately perpendicular to the imaging plane. Future investigations would aim to characterize the structure of elliptical and asymmetrical osteons, for example, or those exhibiting a significant tilt relative to the imaging plane.

It would also be valuable to further investigate the structure of the three osteons analyzed in this work across a greater depth of the cortical bone. The current project was constrained by the limitations of the imaging technique, which allowed image acquisition over a depth of approximately 50 µm. Extending the depth of analysis could help determine whether the lamellar structure evolves as depth increases – particularly, whether the slopes of the linear regressions remain constant – thus providing a more comprehensive assessment of the lamellar conicity that we were able to identify. Furthermore, it would allow the reconstruction of the osteons as mathematical objects, over a greater depth. To achieve this, one could, for example, polish the surface of the sample by 50 µm increments and subsequently perform SHG imaging of the structure.

An alternative approach that could be adopted to investigate the conicity of the lamellae would involve imaging osteons in the longitudinal plane. In such a configuration, one might expect that bands appearing bright in the transverse plane would appear dark in the longitudinal plane, and vice versa for dark bands in the transverse view. However, since we are not sure about the orientation of the collagen fibers within a lamella, this remains a hypothesis that would be interesting to verify.

In Subsection 3.9 F, we mentioned the possibility of inferring the three-dimensional arrangement of a lamella based on the profile of the lamellar angle as a function of the osteon rotation angle. We then suggested to model a lamella as an ideal hollow truncated cone, tilted at a certain angle with respect to the vertical axis, and to perform reslicing at different angles, as illustrated in the schematic representation in Figure 5.2A. This approach would allow us to assess whether a sinewave-shaped profile - similar to the one observed in Figure 3.26 - emerges. This line of investigation could be pursued in the future.

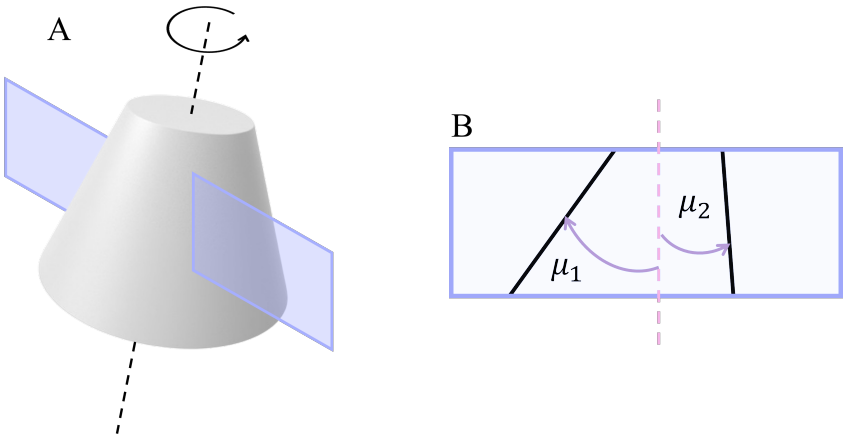


Figure 5.2: **A.** Schematic representation of an idealized lamella, modeled as a truncated cone which is tilted relative to the vertical axis. The blue plane denotes a reslice used for cross-sectional visualization. **B.** In the reslice view, the lamella appears as a pair of linear segments, from which the lamellar angle can be measured.

As explained in Subsection 1.1.4 E, cortical bone is also composed of a complex structure, the lacuno-canalicular network (LCN), which is interwoven with the osteons. Our mathematical model of osteons could be superimposed onto images of the LCN - acquired using confocal microscopy - thereby enabling a more comprehensive visualization and characterization of the cortical bone architecture. A first overview is illustrated in Figure 5.3. It should be noted that a similar work has previously been carried out, in which raw SHG images of concentric lamellae within human osteons were overlaid with

CLSM images of the LCN (Repp et al., 2017). Since osteocytes are involved in bone remodeling, the LCN - which in fact connects osteocytes together - is closely related to the structure of osteons. Therefore, the formation and functionality of these two systems are interrelated. Consequently, it is relevant to investigate potential correlation between the morphology of the LCN — including the canalicular density or the osteocyte morphology, for instance — and that of the lamellae. Since a mathematical representation of the LCN has already been established, the integration of our model of the osteon could enable a novel, simpler and more comprehensive analysis. We could, for example, evaluate the number of canaliculi intersecting each lamella. This idea integrates well with our model, as the lamellae are reduced to unit-thickness lines. Since the canaliculi of the LCN could be reduced to simple edges, the problem is equivalent to determining the mathematical intersections between two curves. In addition, such a model of the cortical bone could be integrated into a dynamic computational framework, in order to be simulated. For instance, one could investigate the impact of fluid flow on cortical bone architecture, specifically the lamellar structure. Indeed, osteocytes are believed to possess mechanosensing properties that allow them to detect mechanical loads induced by the flow of interstitial fluid through the LCN (Weinbaum et al., 1994; Jacobs et al., 2010). This ability may enable them to locally regulate the way they communicate with cells involved in bone remodeling - referred to as mechanotransduction - thereby shaping bone architecture to adapt to local mechanical requirements, akin to orchestra conductors. Recent work has combined experimental and computational methods to precisely quantify the fluid flow, in terms of permeability and fluid velocity, using the same sample as that of this study (van Tol et al., 2020). The lamellar structure, in turn, also plays a key role in shaping the architecture of the osteocyte network. Since osteocytes are the result of the bone remodeling process – specifically through the differentiation of osteoblasts – their embedding within the bone matrix, as well as the extension of their dendritic processes, is constrained by the geometry and orientation of the lamellae (Palumbo and Ferretti, 2021; Mader et al., 2013). This has important implications for osteocyte mechanosensing, bone mineralization, and bone adaptation.

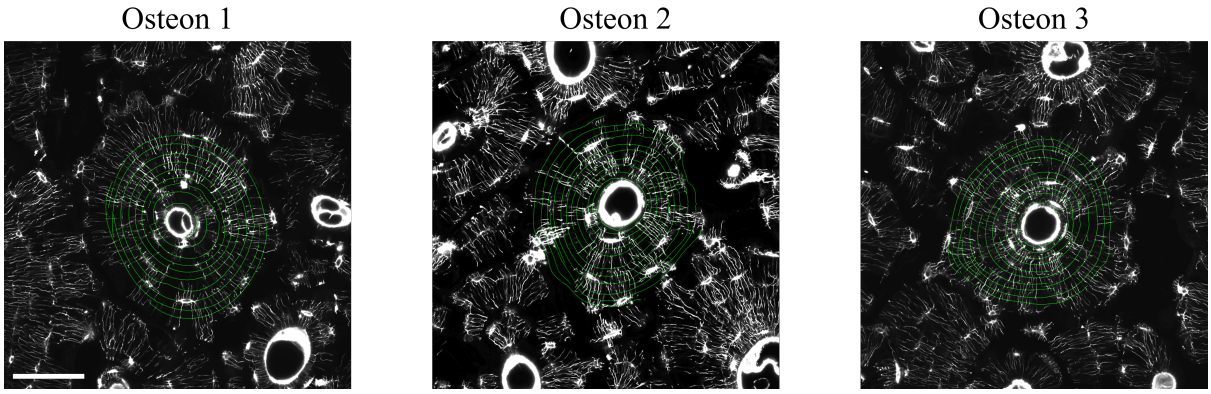


Figure 5.3: Superposition of our mathematical model of osteons (in green) onto LCN images acquired by CLSM (in black and white). For each osteon, the model elegantly aligns with the LCN. The osteocyte lacunae appear to be oriented parallel to the lamellae, while the canaliculi are predominantly oriented radially with respect to the Haversian canal, and therefore perpendicular to the reconstructed lamellae. The middle slice is illustrated for each osteon. Courtesy of Dr. Alexandra Tits. Scale bar: 80 µm.

A further step could involve investigating the relationship between the microarchitecture and other intrinsic properties of cortical bone, including its mineral content and mechanical properties. It would be useful to understand whether the lamellar organization is somehow correlated to these bone properties, and in which way. For instance, it could be that the shape of the osteons or the lamellar conicity are influenced by the mineral content. To investigate such hypotheses, qBEI images of the osteons could be used in combination with our work, allowing for a comprehensive structural assessment. The superimposition of SHG and qBEI images of osteons has already been attempted in previous studies, either to study if the cement line somehow appeared in the SHG images (Cantamessa et al., 2024), or to compare the mor-

phology of bright and dark osteons (as introduced in Subsection 1.2.1 E), specifically in the transverse plane (Stockhausen et al., 2021). However, to date, no study has truly explored the relationship between the mineral content and lamellar morphology of osteons in the longitudinal plane, in part due to the inherently two-dimensional nature of qBEI. The motivation for such an analysis stems in part from earlier findings that reported calcium concentration gradients within bone osteons, between the Haversian canal and the cement line. These studies observed a progressive decrease in calcium content towards the cement line (A. Roschger et al., 2019; Crofts et al., 1994). In particular, a peak in mineral content has been observed in the immediate proximity of Haversian canals. These hypermineralized regions, referred to as *halos* (B. Martin, 1994), potentially correspond to the innermost lamellae, whose distinct morphology compared to other lamellae was highlighted in our study. It would be interesting to investigate potential correlation between these bright halos — hypothetically acting as a calcium reservoir involved in the regulation of calcium homeostasis — and the structural organization of the innermost lamellae. Moreover, as such mineral gradients observed from the Haversian canal to the cement line are thought to be associated with the canalicular density of the LCN, one could perhaps explore connections between the three aspects.

Another promising direction for future research would be to connect our work with a recent study (Hegarty-Cremer et al., 2024), in which a computational model was developed to simulate the progressive formation of lamellae within bone osteons, starting from the cement line – a process referred to as osteon infilling.

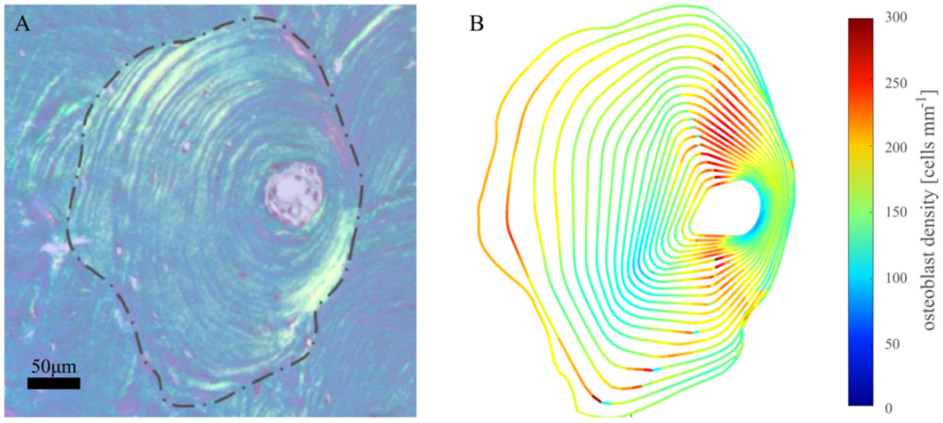


Figure 5.4: Comparison between a stained histological cross-section of an osteon (**A.**) and outcome of the mathematical model simulation (**B.**). Figure adapted from (Hegarty-Cremer et al., 2024).

If our methodology were to be carried out on asymmetric osteons, this computational model could be applied to the reconstructed osteons, to assess how well the simulated "pseudo-lamellae" align with our mathematical representation of lamellae. Furthermore, according to the authors, osteon asymmetry is governed by three main hypotheses, each of which is weighted by specific parameters in the mathematical equations governing the model. These three hypotheses are:

(a) Osteoid deposition is delayed on certain regions of the cement line

(b) Osteoblast generation is heterogeneous in space, resulting in faster infilling in regions where cell density is higher.

(c) Osteoblasts secrete bone matrix at varying rates along the Haversian canal surface, leading to locally accelerated infilling of the pore

By calibrating the parameters of the model so that the pseudo-lamellae align with the lamellae reconstructed from the protocol presented in our work, it may be possible to infer which bone remodeling

mechanisms - and especially, to what extent - contribute to the observed asymmetry in the osteon structure.

Finally, osteons are not the only structural components of bone that can be studied using SHG microscopy. Indeed, trabeculae - which are also composed of lamellae - can similarly be visualized using this technique. As such, our work could, in the near future, be extended to investigate the lamellar architecture within trabecular bone. The microstructure of trabeculae remains poorly investigated as well, especially in terms of lamellar organization. Figure 5.5 illustrates an example of an SHG image of a trabecula. Future studies could aim to develop new methodologies to assess and characterize the morphology of lamellae in these structures.

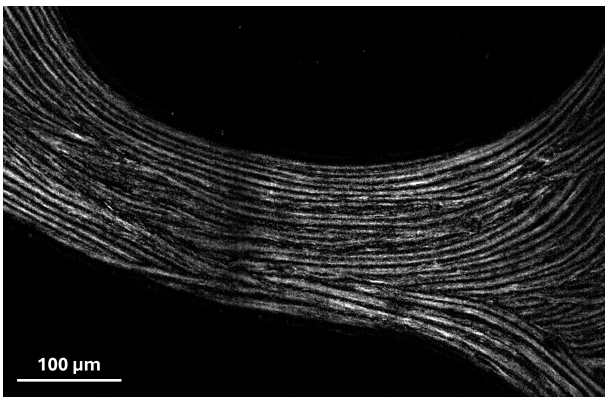


Figure 5.5: SHG image of a single trabecula. Courtesy of Edoardo Pedrinazzi.

Conclusion

The main aim of this Master's thesis was to further investigate the structure of osteons at the micrometer scale. Particular emphasis was placed on a detailed analysis of the three-dimensional architecture of lamellae. To achieve this, new methodologies were developed to improve the characterization of these structures, based on SHG images of three osteons from a femoral bone sample of a 56-year-old patient.

Initially, the structure of each osteon was analyzed in the longitudinal plane, solely based on the stack of cross-sectional images – thus avoiding the need for an alternative way of imaging the sample. This was achieved through reslicing. Since lamellae form concentric rings in the cross-sectional view, they appear as relatively straight lines in the longitudinal plane. This observations motivated the fitting of linear regressions to quantitatively characterize their organization. The following key observations were made:

- Contrary to the widely accepted assumption that lamellae form concentric cylindrical structures in space, our findings proved that they actually exhibit a conical geometry.
- The innermost lamellae exhibit quite a different structure compared to the others. Their opening consistently faces the surface of the sample as it was imaged, whereas for the remaining lamellae, the orientation depends on the reslice under consideration. This could be explained by the fact that, as they are the most recently deposited lamellae, they could be in an early stage of bone remodeling, thus exhibiting a less organized structure.
- While lamellae show variability from one another, adjacent lamellae show a notable degree of similarity - particularly if located in the intermediate region between the Haversian canal and the cement line. This may be attributed to a higher degree of structural organization. Interestingly, these intermediate lamellae are also the most clearly distinguishable in the SHG images.

Subsequently, a protocol was developed to reconstruct the osteon as a mathematical object, through the implementation of a simplified model of the lamellae as they appear in the raw SHG images. To refine the structure that was manually reconstructed at three specific slices of the image stack, the linear regressions introduced in the first part of the work were leveraged as additional information, to make connections with the second phase of the project. The resulting model yielded highly satisfactory results, with an approximation of the lamellae closely following the raw SHG signal. Nevertheless, as always, there remains room for improvement - particularly to address specific cases and exceptions, such as spiraling lamellae.

Lamellae result from successive temporal stages of bone formation. Discretizing them into mathematical objects is very interesting, as it would enable a comprehensive characterization of the temporal evolution of the LCN and of the osteocyte network. Nevertheless, one should keep in mind that when we image bone, we essentially capture a snapshot of its structure at a single, frozen instant in time. In other words, what we obtain is a static representation of a tissue whose structure is the result of dynamic processes. From this static state, we attempt to infer information about the underlying formation mechanisms and how the observed structure relates to mechanical and biological functions of bone. Although the images we analyze reflect a fingerprint of bone remodeling, we must be cautious not to overinterpret them. Misinterpreting static features as direct evidence of dynamic mechanisms might indeed lead to inaccurate or misleading conclusions.

In conclusion, this work mainly aimed to propose new evaluation methods, thereby opening the way to new opportunities in the field of research. We clearly specified the limitations and suggested a few improvements for the future. Furthermore, a wide range of future directions was outlined. This thesis may be seen as an additional piece added to an ongoing puzzle - placed alongside other scattered pieces. Over time, other pieces will help complete the picture and gradually reveal the broader landscape of knowledge.

Appendices

Appendix A: Inspection of the raw SHG images

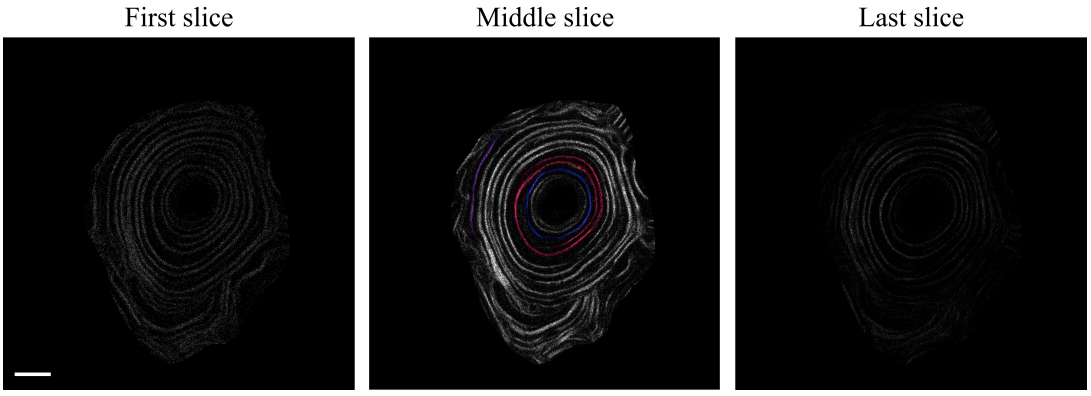


Figure 6: First, middle and last slices of the stack of images of osteon 2. In the middle slice, three particular configurations of bright bands (lamellae) are highlighted in colors. Scale bar: 40 µm.

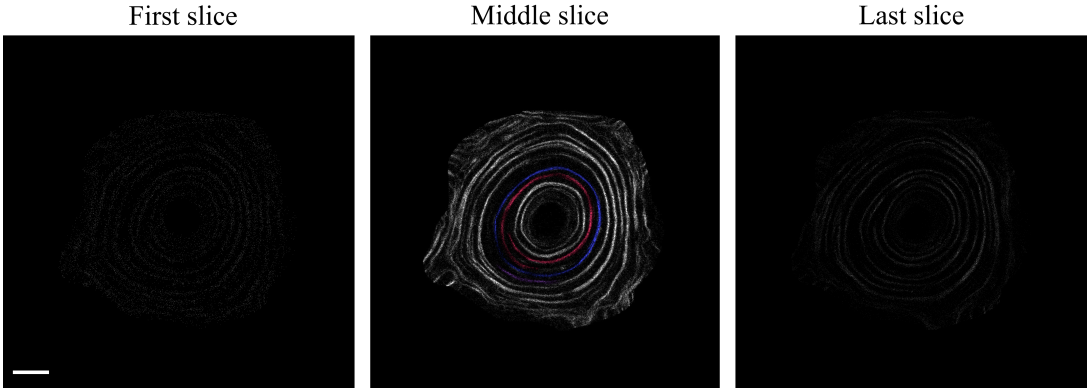


Figure 7: First, middle and last slices of the stack of images of osteon 3. In the middle slice, three particular configurations of bright bands (lamellae) are highlighted in colors. Scale bar: 40 µm.

Appendix B: Inspection of the binarized SHG images

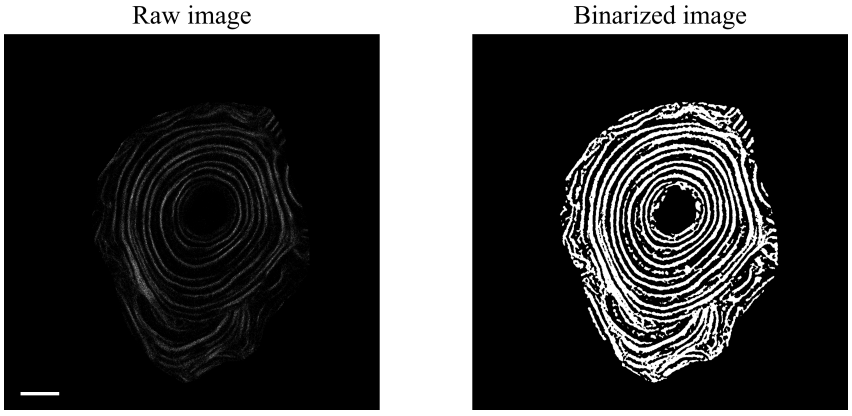


Figure 8: Comparison between the raw image and the binarized image for Osteon 2 (slice 68 out of 136). Scale bar: 40 µm.

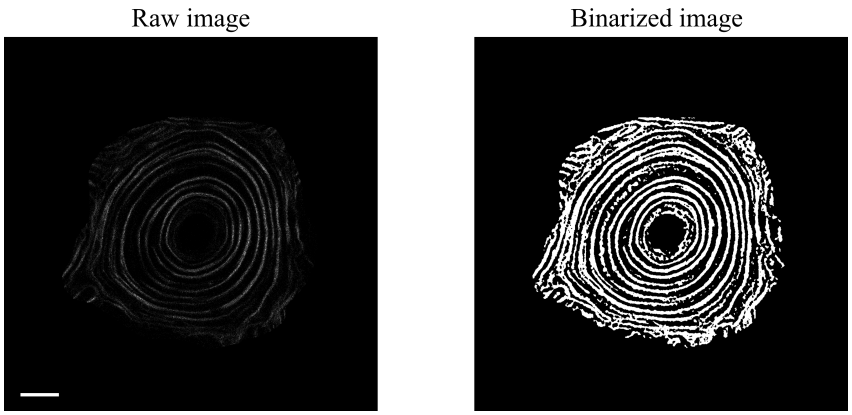


Figure 9: Comparison between the raw image and the binarized image for Osteon 3 (slice 68 out of 136). Scale bar: 40 µm.

Appendix C: Global center of mass of the osteon

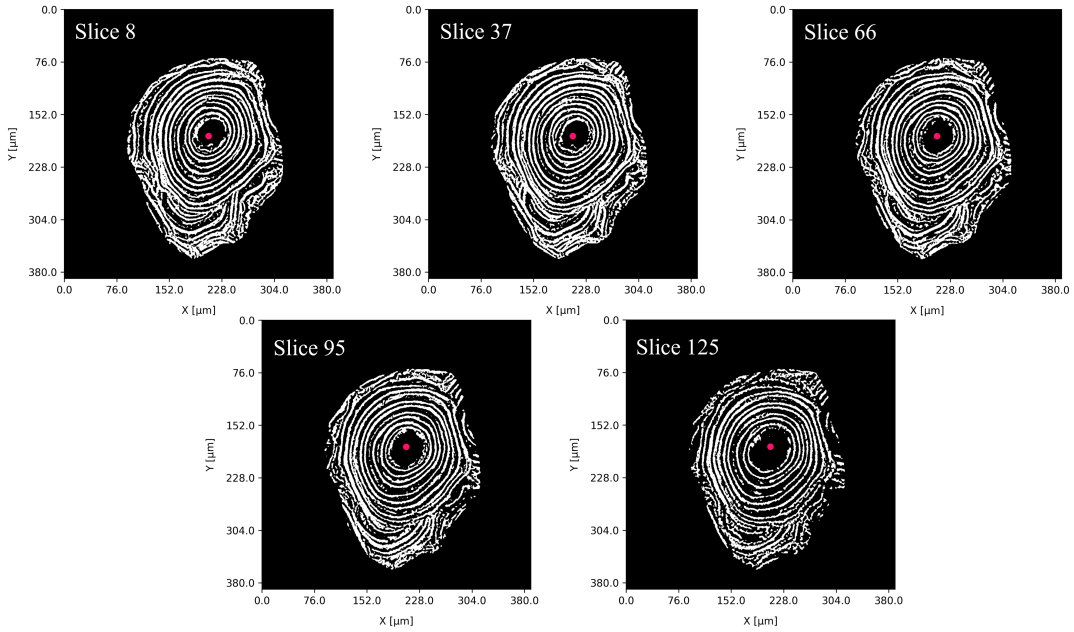


Figure 10: Specific slices of the binarized stack of images of osteon 2. For each slice, the global center of mass of the osteon is displayed as a red point. A magnified view is illustrated when the point is close to the innermost lamella. In all slices, the center of the osteon remains within the Haversian canal. The number of each slice is indicated (out of 136).

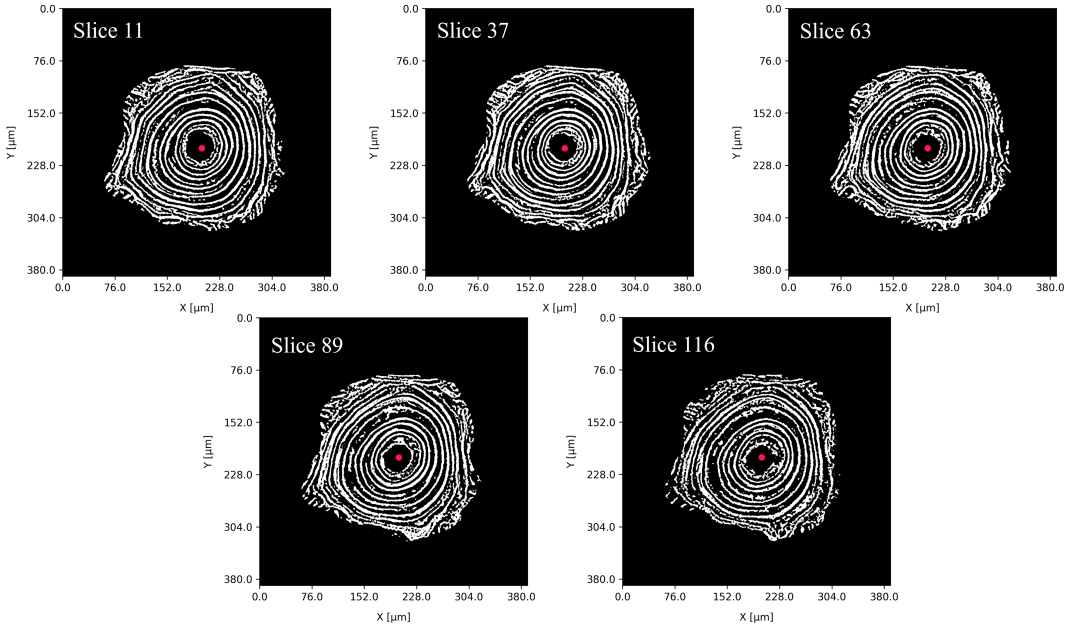


Figure 11: Specific slices of the binarized stack of images of osteon 3. For each slice, the global center of mass of the osteon is displayed as a red point. A magnified view is illustrated when the point is close to the innermost lamella. In all slices, the center of the osteon remains within the Haversian canal. The number of each slice is indicated (out of 136).

Appendix D: Osteon reslicing

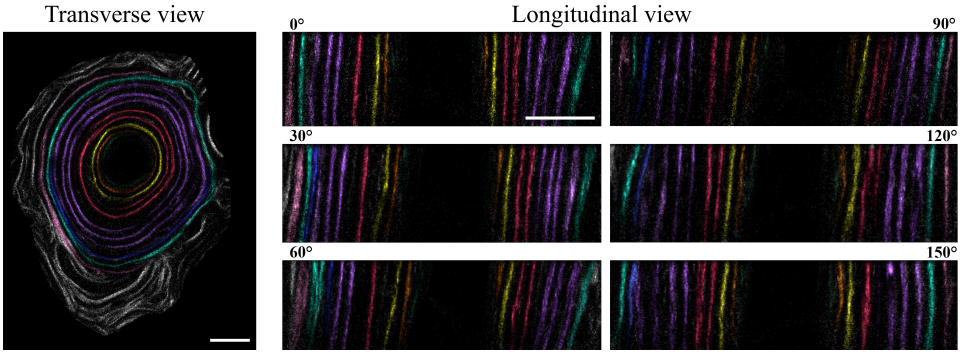


Figure 12: Reslices of osteon 2. The lamellae have been labeled through coloring to facilitate their identification from one cut to another, and their matching with respect to the the transverse plane. Scale bars: 40 µm.

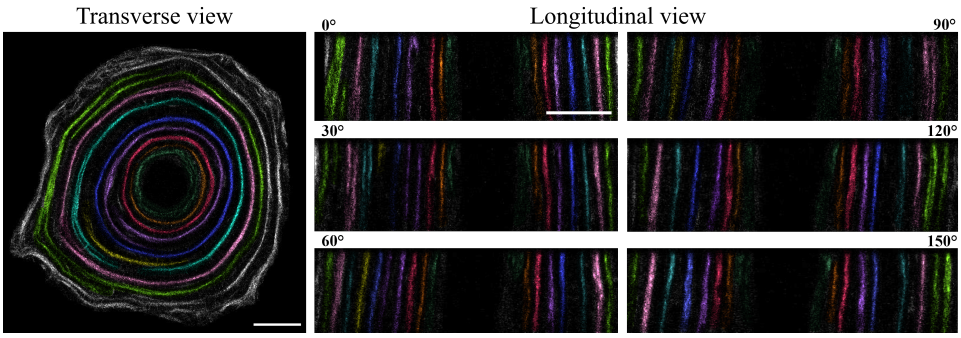


Figure 13: Reslices of osteon 3. The lamellae have been labeled through coloring to facilitate their identification from one cut to another, and their matching with respect to the the transverse plane. Scale bars: 40 µm.

Appendix E: Linear regression fit

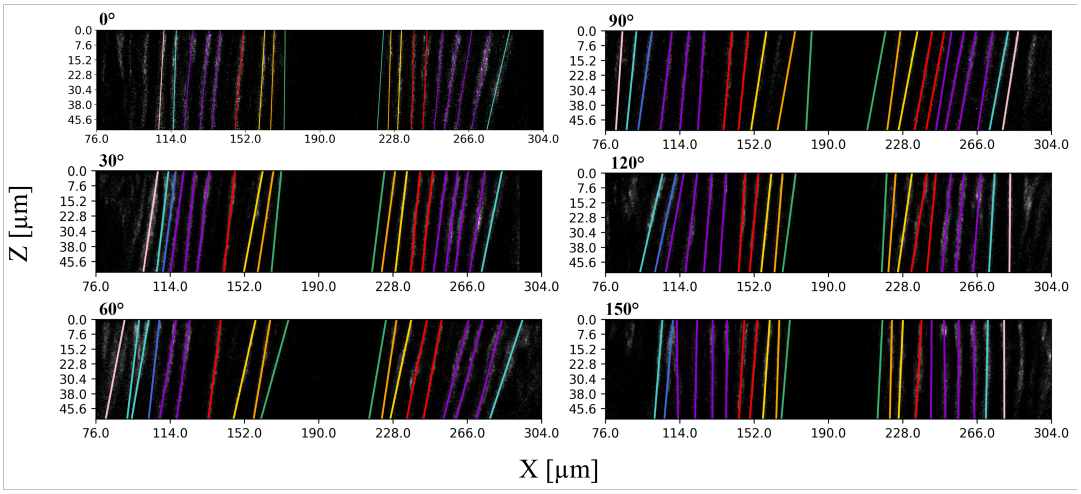


Figure 14: Regression lines fitted to the lamellae visible in all reslices, obtained after rotating osteon 2 every 30°.

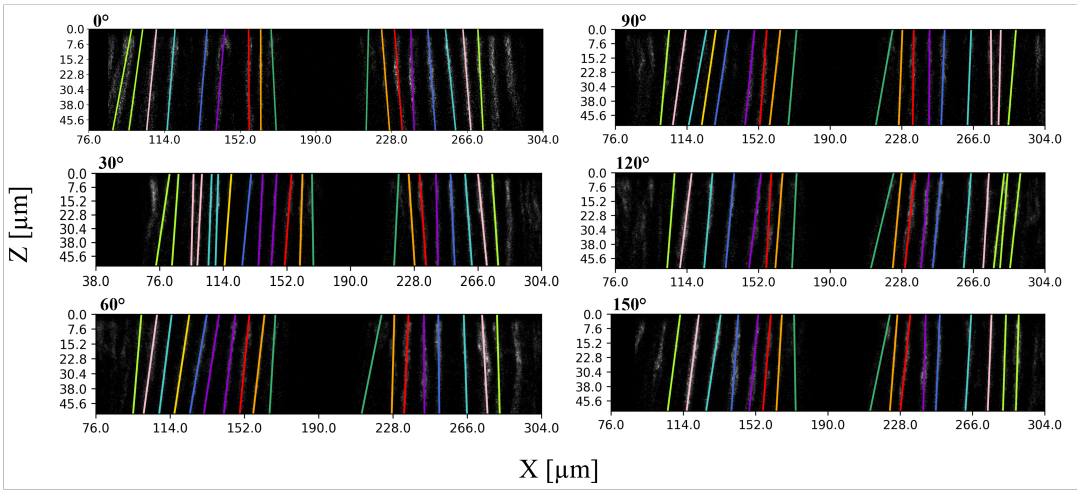


Figure 15: Regression lines fitted to the lamellae visible in all reslices, obtained after rotating osteon 3 every 30°.

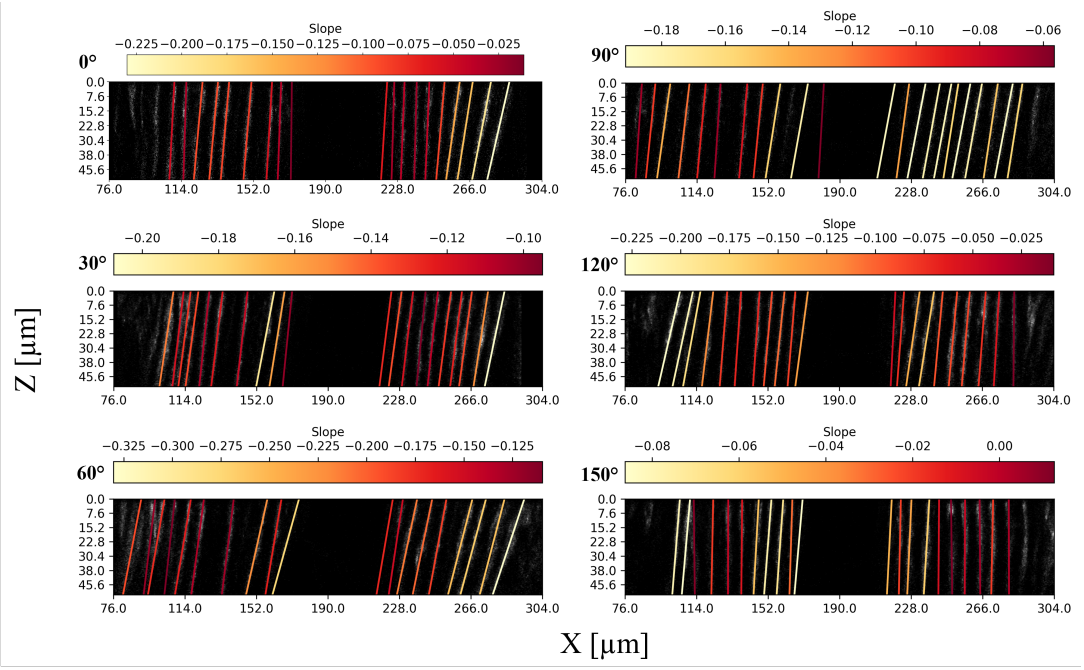


Figure 16: Color-coded regression lines according to slope values. All reslices of osteon 2 are shown.

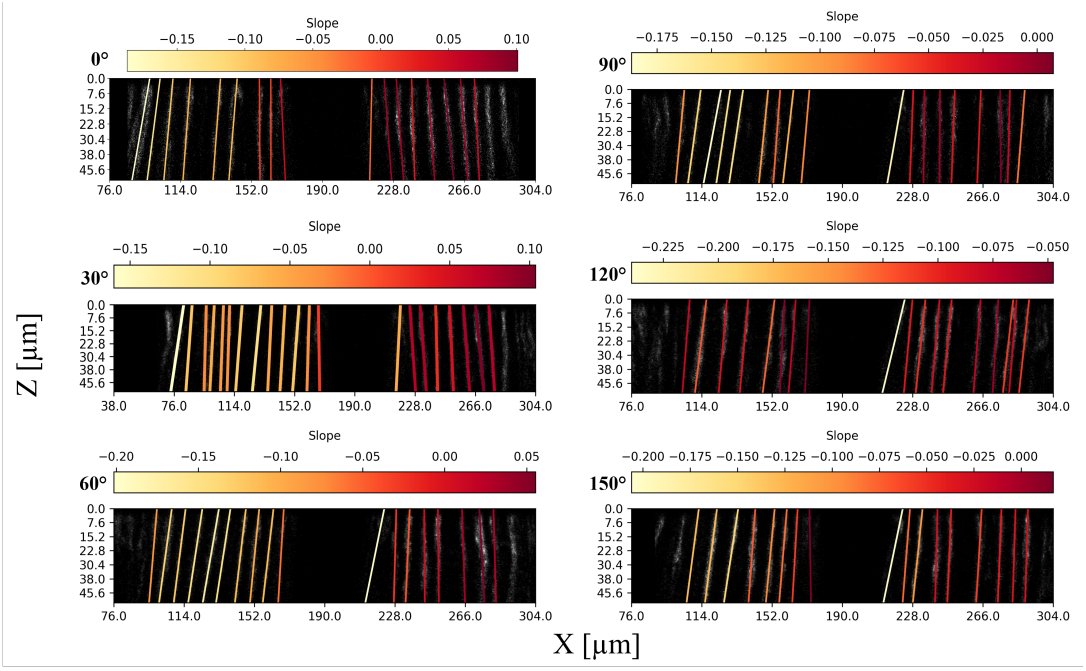


Figure 17: Color-coded regression lines according to slope values. All reslices of osteon 3 are shown.

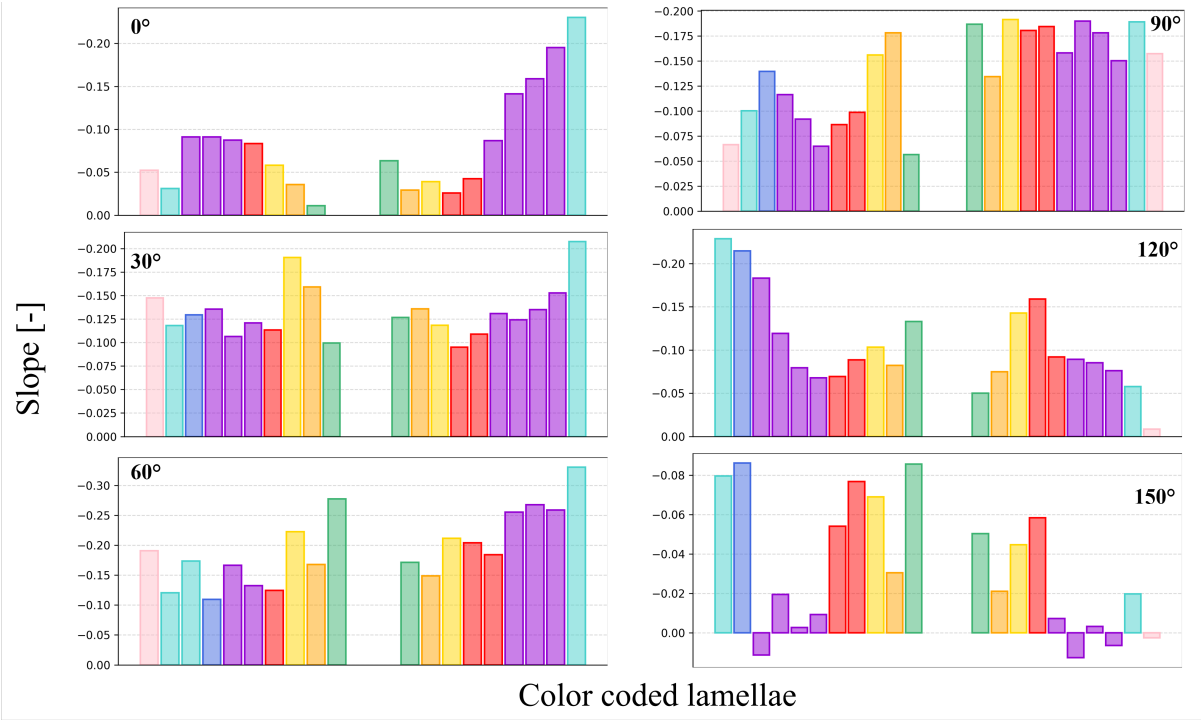


Figure 18: Histograms displaying the slope of each linear regression. Each bar corresponds to a lamella and shares its respective color. The gap representing the Haversian canal. These plots are related to osteon 2.

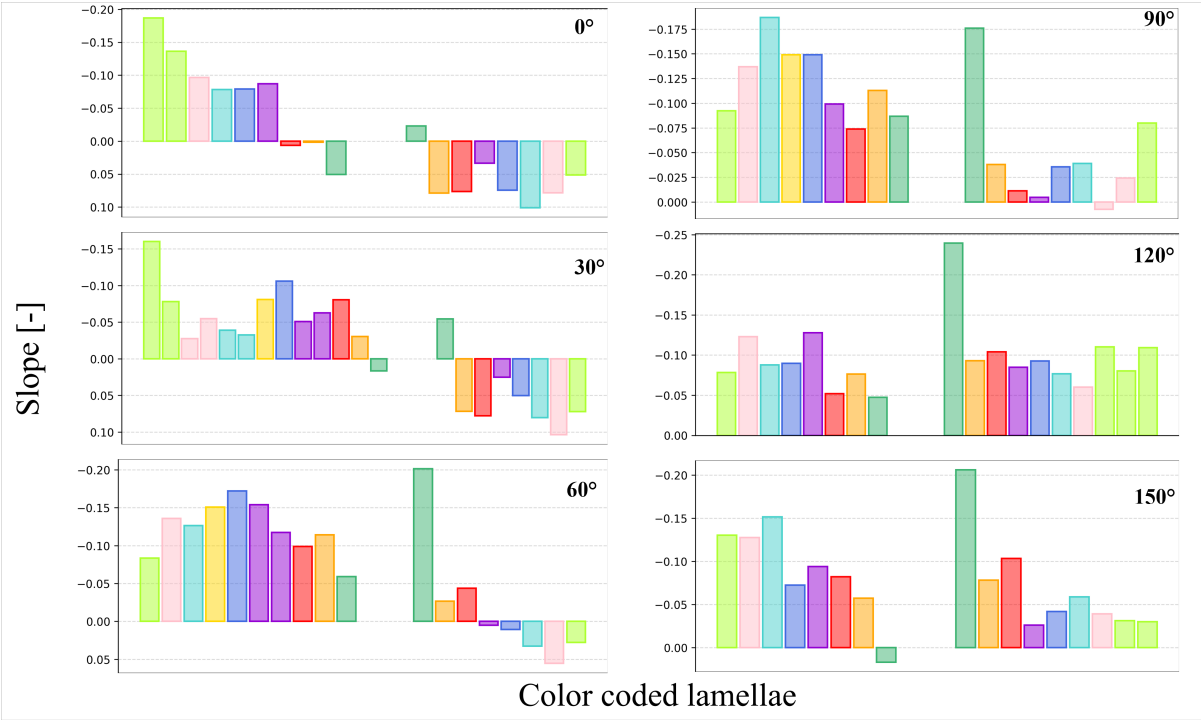


Figure 19: Histograms displaying the slope of each linear regression. Each bar corresponds to a lamella and shares its respective color. The gap representing the Haversian canal. These plots are related to osteon 3.

Appendix F: Lamellar intercept vs. osteon rotation angle

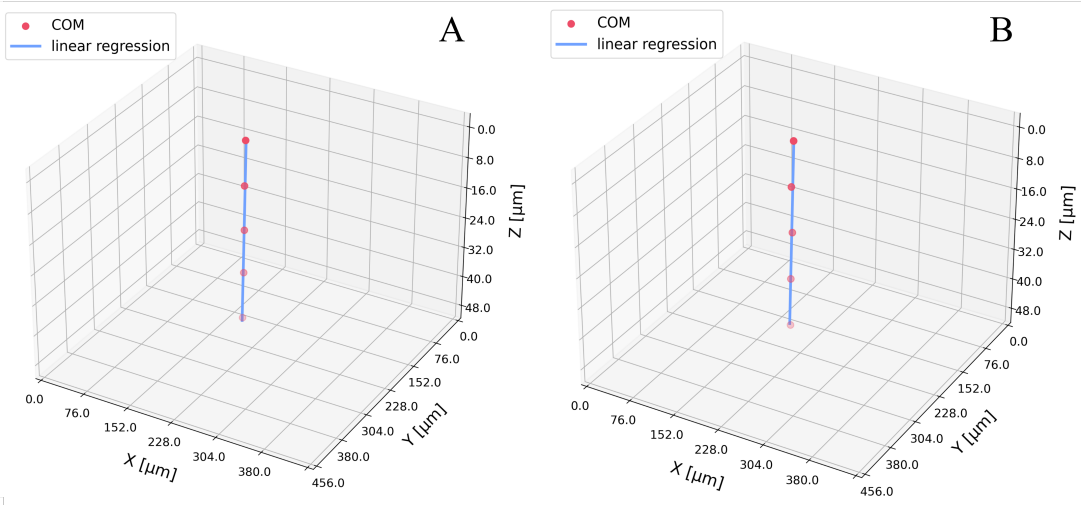


Figure 20: Linear regression (blue line) fitted to the osteon's center of mass measured at different depths (red points). **A.** Osteon 2 and **B.** Osteon 3.

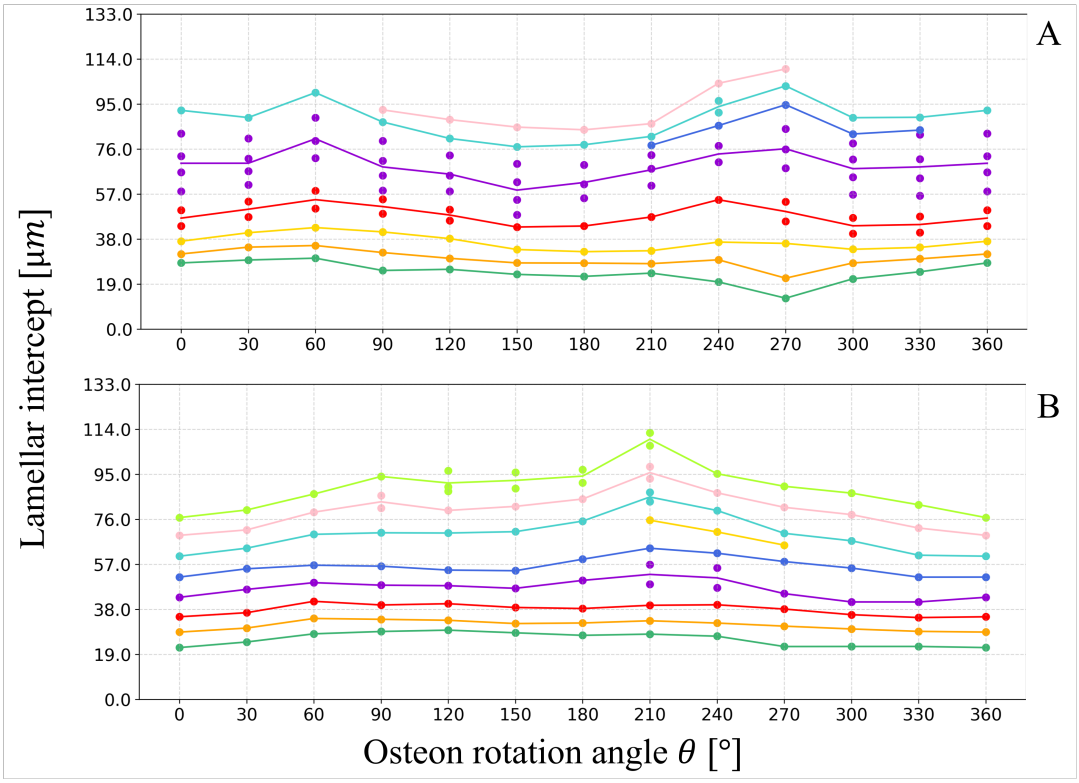


Figure 21: Lamellar x-intercept as a function of the osteon rotation angle. The coordinate system was shifted to align with the center of the image, to have consistent values. **A.** Osteon 2 and **B.** Osteon 3.

References

Aghigh, A., Bancelin, S., Rivard, M., Pinsard, M., Ibrahim, H., & Légaré, F. (2023). Second harmonic generation microscopy: A powerful tool for bio-imaging. *Biophysical Reviews*, *15*(1), 43–70. https://doi.org/10.1007/s12551-022-01041-6

Akhtar, K., Khan, S. A., Khan, S. B., & Asiri, A. M. (2018). Scanning electron microscopy: Principle and applications in nanomaterials characterization. In S. K. Sharma (Ed.), *Handbook of materials characterization* (pp. 113–145). Springer International Publishing. https://doi.org/10.1007/978-3-319-92955-2_4

Alias, M. A., & Buenzli, P. R. (2017). Modeling the effect of curvature on the collective behavior of cells growing new tissue. *Biophysical Journal*, *112*(1), 193–204. https://doi.org/10.1016/j.bpj.2016.11.3203

Alias, M. A., & Buenzli, P. R. (2018). Osteoblasts infill irregular pores under curvature and porosity controls: A hypothesis-testing analysis of cell behaviours. *Biomechanics and Modeling in Mechanobiology*, *17*(5), 1357–1371. https://doi.org/10.1007/s10237-018-1031-x

Ambekar, R., Lau, T.-Y., Walsh, M., Bhargava, R., & Toussaint, K. C. (2012). Quantifying collagen structure in breast biopsies using second-harmonic generation imaging [Publisher: Optica Publishing Group]. *Biomedical Optics Express*, *3*(9), 2021–2035. https://doi.org/10.1364/BOE.3.002021

Andreasen, C. M., Delaisse, J.-M., Van Der Eerden, B. C., Van Leeuwen, J. P., Ding, M., & Andersen, T. L. (2018). Understanding age-induced cortical porosity in women: The accumulation and coalescence of eroded cavities upon existing intracortical canals is the main contributor. *Journal of Bone and Mineral Research*, *33*(4), 606–620. https://doi.org/10.1002/jbmr.3354

Andronowski, J. M., & Cole, M. E. (2021). Current and emerging histomorphometric and imaging techniques for assessing age-at-death and cortical bone quality. *WIREs Forensic Science*, *3*(2), e1399. https://doi.org/10.1002/wfs2.1399

Ardizzoni, A. (2001). Osteocyte lacunar size–lamellar thickness relationships in human secondary osteons. *Bone*, *28*(2), 215–219. https://doi.org/10.1016/S8756-3282(00)00417-8

Baird, E., & Taylor, G. (2017). X-ray micro computed-tomography. *Current Biology*, *27*(8), R289–R291. https://doi.org/10.1016/j.cub.2017.01.066

Blouin, S., Roschger, A., Varga, F., Misof, B., Spitzer, S., Roschger, P., & Klaushofer, K. (2018). Confocal laser scanning microscopy—a powerful tool in bone research. *Wiener Medizinische Wochenschrift*, *168*(11), 314–321. https://doi.org/10.1007/s10354-018-0639-x

Bolamperti, S., Villa, I., & Rubinacci, A. (2022). Bone remodeling: An operational process ensuring survival and bone mechanical competence [Publisher: Nature Publishing Group]. *Bone Research*, *10*(1), 1–19. https://doi.org/10.1038/s41413-022-00219-8

Boskey, A., & Coleman, R. (2010). Aging and bone. *Journal of Dental Research*, *89*(12), 1333–1348. https://doi.org/10.1177/0022034510377791

Bouxsein, M. L., Boyd, S. K., Christiansen, B. A., Guldberg, R. E., Jepsen, K. J., & Müller, R. (2010). Guidelines for assessment of bone microstructure in rodents using micro–computed tomography. *Journal of Bone and Mineral Research*, *25*(7), 1468–1486. https://doi.org/10.1002/jbmr.141

Boyde, A., & Hobdell, M. H. (1968). Scanning electron microscopy of lamellar bone. *Zeitschrift für Zellforschung und Mikroskopische Anatomie*, *93*(2), 213–231. https://doi.org/10.1007/BF00336690

Boyde, A., & Riggs, C. M. (1990). The quantitative study of the orientation of collagen in compact bone slices. *Bone*, *11*(1), 35–39. https://doi.org/10.1016/8756-3282(90)90069-B

Britz, H. M., Thomas, C. D. L., Clement, J. G., & Cooper, D. M. L. (2009). The relation of femoral osteon geometry to age, sex, height and weight. *Bone*, *45*(1), 77–83. https://doi.org/10.1016/j.bone.2009.03.654

Bromage, T. G., Goldman, H. M., McFarlin, S. C., Warshaw, J., Boyde, A., & Riggs, C. M. (2003). Circularly polarized light standards for investigations of collagen fiber orientation in bone [_eprint:

https://onlinelibrary.wiley.com/doi/pdf/10.1002/ar.b.10031]. *The Anatomical Record Part B: The New Anatomist*, *274B*(1), 157–168. https://doi.org/10.1002/ar.b.10031

Buenzli, P. R., Pivonka, P., & Smith, D. W. (2014). Bone refilling in cortical basic multicellular units: Insights into tetracycline double labelling from a computational model. *Biomechanics and Modeling in Mechanobiology*, *13*(1), 185–203. https://doi.org/10.1007/s10237-013-0495-y

Burr, D. B. (n.d.). Bone quality: Understanding what matters.

Campagnola, P., & Dong, C.-Y. (2011). Second harmonic generation microscopy: Principles and applications to disease diagnosis [_eprint: https://onlinelibrary.wiley.com/doi/pdf/10.1002/lpor.200910024]. *Laser & Photonics Reviews*, *5*(1), 13–26. https://doi.org/10.1002/lpor.200910024

Cantamessa, A., Blouin, S., Rummler, M., Berzlanovich, A., Weinkamer, R., Hartmann, M. A., & Ruffoni, D. (2024, October 10). The mineralization of osteonal cement line depends on where the osteon is formed [Pages: 2024.10.06.616843 Section: New Results]. https://doi.org/10.1101/2024.10.06.616843

Cantamessa, A. (2025). *Looking beyond the boundaries: High-resolution multimodal characterization of material, mechanical, and biological properties of the cement line in human osteonal bone* [Doctoral dissertation, ULiège - Université de Liège [Faculté des Sciences Appliquées], Liège, Belgium] [Backup Publisher: FRIA - Fonds pour la Formation à la Recherche dans l'Industrie et dans l'Agriculture].

Cohen, J., & Harris, W. H. (1958). The three-dimensional anatomy of haversian systems. *JBJS*, *40*(2), 419. Retrieved May 10, 2025, from https://journals.lww.com/jbjsjournal/citation/1958/40020/The_Three_Dimensional_Anatomy_of_Haversian.15.aspx

Collins, C. J., Kozyrev, M., Frank, M., Andriotis, O. G., Byrne, R. A., Kiener, H. P., Pretterklieber, M. L., & Thurner, P. J. (2020). The impact of age, mineralization, and collagen orientation on the mechanics of individual osteons from human femurs. *Materialia*, *9*, 100573. https://doi.org/10.1016/j.mtla.2019.100573

Compston, J. (2006). Bone quality: What is it and how is it measured? *Arquivos Brasileiros de Endocrinologia & Metabologia*, *50*(4), 579–585. https://doi.org/10.1590/S0004-27302006000400003

Cooke, K. M., Mahoney, P., & Miszkiewicz, J. J. (2022). Secondary osteon variants and remodeling in human bone [_eprint: https://onlinelibrary.wiley.com/doi/pdf/10.1002/ar.24646]. *The Anatomical Record*, *305*(6), 1299–1315. https://doi.org/10.1002/ar.24646

Cox, G. (2011). Biological applications of second harmonic imaging. *Biophysical Reviews*, *3*(3), 131–141. https://doi.org/10.1007/s12551-011-0052-9

Cox, G., Kable, E., Jones, A., Fraser, I., Manconi, F., & Gorrell, M. D. (2003). 3-dimensional imaging of collagen using second harmonic generation. *Journal of Structural Biology*, *141*(1), 53–62. https://doi.org/10.1016/S1047-8477(02)00576-2

Crofts, R. D., Boyce, T. M., & Bloebaum, R. D. (1994). Aging changes in osteon mineralization in the human femoral neck. *Bone*, *15*(2), 147–152. https://doi.org/10.1016/8756-3282(94)90701-3

Currey, J. D. (2002). *Bones: Structure and mechanics* [Google-Books-ID: 2jYsJhxiNWQC]. Princeton University Press.

Dallas, S. L., & Bonewald, L. F. (2010). Dynamics of the transition from osteoblast to osteocyte [_eprint: https://onlinelibrary.wiley.com/doi/pdf/10.1111/j.1749-6632.2009.05246.x]. *Annals of the New York Academy of Sciences*, *1192*(1), 437–443. https://doi.org/10.1111/j.1749-6632.2009.05246.x

Delmas, P. D., & Seeman, E. (2004). Changes in bone mineral density explain little of the reduction in vertebral or nonvertebral fracture risk with anti-resorptive therapy. *Bone*, *34*(4), 599–604. https://doi.org/10.1016/j.bone.2003.12.022

Dempster, D. W. (2017). Tethering formation to resorption: Reversal revisited. *Journal of Bone and Mineral Research*, *32*(7), 1389–1390. https://doi.org/10.1002/jbmr.3169

Doube, M. (2022). Closing cones create conical lamellae in secondary osteonal bone [Publisher: Royal Society]. *Royal Society Open Science*, *9*(8), 220712. https://doi.org/10.1098/rsos.220712

Fratzl, P., Gupta, H. S., Paschalis, E. P., & Roschger, P. (2004). Structure and mechanical quality of the collagen–mineral nano-composite in bone [Publisher: The Royal Society of Chemistry]. *Journal of Materials Chemistry*, *14*(14), 2115–2123. https://doi.org/10.1039/B402005G

Fratzl, P., & Weinkamer, R. (2007). Nature's hierarchical materials. *Progress in Materials Science*, *52*(8), 1263–1334. https://doi.org/10.1016/j.pmatsci.2007.06.001

Frost, H. M. (1991). Some ABC's of skeletal pathophysiology. 6. the growth/modeling/remodeling distinction. *Calcified Tissue International*, *49*(5), 301–302. https://doi.org/10.1007/BF02556248

Frost, H. M. (1964). The laws of bone structure. springfield il. *Charles C. Thomas*.

Gauderon, R., Lukins, P. B., & Sheppard, C. J. R. (2001). Optimization of second-harmonic generation microscopy. *Micron*, *32*(7), 691–700. https://doi.org/10.1016/S0968-4328(00)00066-4

Gebhardt, W. (1906). Über funktionell wichtige anordnungsweisen der feineren und gröberen bauelemente des wirbeltierknochens. ii. spezieller teil der bau der haversschen lamellensysteme und seine funktionelle bedeutung. *Arch. Entwickl. Mech. Org*, *20*, 187–322.

Genthial, R., Beaurepaire, E., Schanne-Klein, M.-C., Peyrin, F., Farlay, D., Olivier, C., Bala, Y., Boivin, G., Vial, J.-C., Débarre, D., & Gourrier, A. (2017). Label-free imaging of bone multiscale porosity and interfaces using third-harmonic generation microscopy [Publisher: Nature Publishing Group]. *Scientific Reports*, *7*(1), 3419. https://doi.org/10.1038/s41598-017-03548-5

Giraud-Guille, M. M. (1988). Twisted plywood architecture of collagen fibrils in human compact bone osteons. *Calcified Tissue International*, *42*(3), 167–180. https://doi.org/10.1007/BF02556330

Goldstein, J. (2012, December 6). *Practical scanning electron microscopy: Electron and ion microprobe analysis* [Google-Books-ID: zBEDCAAAQBAJ]. Springer Science & Business Media.

Hadjidakis, D. J., & Androulakis, I. I. (2006). Bone remodeling. *Annals of the New York Academy of Sciences*, *1092*(1), 385–396. https://doi.org/10.1196/annals.1365.035

Hartmann, M. A., Blouin, S., Misof, B. M., Fratzl-Zelman, N., Roschger, P., Berzlanovich, A., Gruber, G. M., Brugger, P. C., Zwerina, J., & Fratzl, P. (2021). Quantitative backscattered electron imaging of bone using a thermionic or a field emission electron source. *Calcified Tissue International*, *109*(2), 190–202. https://doi.org/10.1007/s00223-021-00832-5

Hegarty-Cremer, S. G. D., Borggaard, X. G., Andreasen, C. M., van der Eerden, B. C. J., Simpson, M. J., Andersen, T. L., & Buenzli, P. R. (2024). How osteons form: A quantitative hypothesis-testing analysis of cortical pore filling and wall asymmetry. *Bone*, *180*, 116998. https://doi.org/10.1016/j.bone.2023.116998

Hegarty-Cremer, S. G. D., Simpson, M. J., Andersen, T. L., & Buenzli, P. R. (2021). Modelling cell guidance and curvature control in evolving biological tissues. *Journal of Theoretical Biology*, *520*, 110658. https://doi.org/10.1016/j.jtbi.2021.110658

Helmchen, F., & Denk, W. (2005). Deep tissue two-photon microscopy [Publisher: Nature Publishing Group]. *Nature Methods*, *2*(12), 932–940. https://doi.org/10.1038/nmeth818

Hennig, C., Thomas, C. D. L., Clement, J. G., & Cooper, D. M. L. (2015). Does 3d orientation account for variation in osteon morphology assessed by 2d histology? *Journal of Anatomy*, *227*(4), 497–505. https://doi.org/10.1111/joa.12357

Hirashima, S., Ohta, K., Kanazawa, T., Togo, A., Tsuneyoshi, R., Miyazono, Y., Kusukawa, J., & Nakamura, K.-i. (2020). Correlative imaging of collagen fibers and fibroblasts using CLEM optimized for picrosirius red staining and FIB/SEM tomography. *Microscopy*, *69*(5), 324–329. https://doi.org/10.1093/jmicro/dfaa024

Hoover, E. E., & Squier, J. A. (2013). Advances in multiphoton microscopy technology [Publisher: Nature Publishing Group]. *Nature Photonics*, *7*(2), 93–101. https://doi.org/10.1038/nphoton.2012.361

Houle, M.-A., Couture, C.-A., Bancelin, S., Van der Kolk, J., Auger, E., Brown, C., Popov, K., Ramunno, L., & Légaré, F. (2015). Analysis of forward and backward second harmonic generation images to probe the nanoscale structure of collagen within bone and cartilage [_eprint: https://onlinelibrary.wiley.com/doi/pdf/10.1002/jbio.201500150]. *Journal of Biophotonics*, *8*(11), 993–1001. https://doi.org/10.1002/jbio.201500150

Jacobs, C. R., Temiyasathit, S., & Castillo, A. B. (2010). Osteocyte Mechanobiology and Pericellular Mechanics [Publisher: Annual Reviews]. *Annual Review of Biomedical Engineering*, *12*, 369–400. https://doi.org/10.1146/annurev-bioeng-070909-105302

Jaworski, Z. F., & Lok, E. (1972). The rate of osteoclastic bone erosion in haversian remodeling sites of adult dog's rib. *Calcified Tissue Research*, *10*(1), 103–112. https://doi.org/10.1007/BF02012540

Jilka, R. L., Weinstein, R. S., Bellido, T., Parfitt, A. M., & Manolagas, S. C. (1998). Osteoblast programmed cell death (apoptosis): Modulation by growth factors and cytokines. *Journal of Bone and Mineral Research*, *13*(5), 793–802. https://doi.org/10.1359/jbmr.1998.13.5.793

Jones, S. J., Boyde, A., & Pawley, J. B. (1975). Osteoblasts and collagen orientation. *Cell and Tissue Research*, *159*(1), 73–80. https://doi.org/10.1007/BF00231996

Kanis, J. A. (2002). Diagnosis of osteoporosis and assessment of fracture risk [Publisher: Elsevier]. *The Lancet*, *359*(9321), 1929–1936. https://doi.org/10.1016/S0140-6736(02)08761-5

Kerschnitzki, M. (2012, March 1). *Bone material characteristics influenced by osteocytes* [Doctoral dissertation, Mathematisch-Naturwissenschaftliche Fakultät I]. https://doi.org/10.18452/16479

LaComb, R., Nadiarnykh, O., Townsend, S. S., & Campagnola, P. J. (2008). Phase matching considerations in second harmonic generation from tissues: Effects on emission directionality, conversion efficiency and observed morphology. *Optics Communications*, *281*(7), 1823–1832. https://doi.org/10.1016/j.optcom.2007.10.040

Lafage-Proust, M.-H., Roche, B., Langer, M., Cleret, D., Vanden Bossche, A., Olivier, T., & Vico, L. (2015). Assessment of bone vascularization and its role in bone remodeling. *BoneKEy Reports*, *4*, 662. https://doi.org/10.1038/bonekey.2015.29

Lassen, N. E., Andersen, T. L., Pløen, G. G., Søe, K., Hauge, E. M., Harving, S., Eschen, G. E. T., & Delaisse, J.-M. (2017). Coupling of bone resorption and formation in real time: New knowledge gained from human haversian BMUs. *Journal of Bone and Mineral Research*, *32*(7), 1395–1405. https://doi.org/10.1002/jbmr.3091

Lerebours, C., Weinkamer, R., Roschger, A., & Buenzli, P. R. (2020). Mineral density differences between femoral cortical bone and trabecular bone are not explained by turnover rate alone. *Bone Reports*, *13*, 100731. https://doi.org/10.1016/j.bonr.2020.100731

Liu, F., Yu, Z., Wang, B., & Chiou, B.-S. (2023). Changes in structures and properties of collagen fibers during collagen casing film manufacturing [Number: 9 Publisher: Multidisciplinary Digital Publishing Institute]. *Foods*, *12*(9), 1847. https://doi.org/10.3390/foods12091847

Lutz, V., Sattler, M., Gallinat, S., Wenck, H., Poertner, R., & Fischer, F. (2012). Impact of collagen crosslinking on the second harmonic generation signal and the fluorescence lifetime of collagen autofluorescence [_eprint: https://onlinelibrary.wiley.com/doi/pdf/10.1111/j.1600-0846.2011.00549.x]. *Skin Research and Technology*, *18*(2), 168–179. https://doi.org/10.1111/j.1600-0846.2011.00549.x

Mader, K. S., Schneider, P., Müller, R., & Stampanoni, M. (2013). A quantitative framework for the 3d characterization of the osteocyte lacunar system. *Bone*, *57*(1), 142–154. https://doi.org/10.1016/j.bone.2013.06.026

Maggiano, I. S., Maggiano, C. M., Clement, J. G., Thomas, C. D. L., Carter, Y., & Cooper, D. M. L. (2016). Three-dimensional reconstruction of haversian systems in human cortical bone using synchrotron radiation-based micro-CT: Morphology and quantification of branching and transverse connections across age [_eprint: https://onlinelibrary.wiley.com/doi/pdf/10.1111/joa.12430]. *Journal of Anatomy*, *228*(5), 719–732. https://doi.org/10.1111/joa.12430

Marotti, G. (1993). A new theory of bone lamellation. *Calcified Tissue International*, *53*(1), S47–S56. https://doi.org/10.1007/BF01673402

Marotti, G., Ferretti, M., & Palumbo, C. (2013). The problem of bone lamellation: An attempt to explain different proposed models [_eprint: https://onlinelibrary.wiley.com/doi/pdf/10.1002/jmor.20114]. *Journal of Morphology*, *274*(5), 543–550. https://doi.org/10.1002/jmor.20114

Martin, B. (1994). Mathematical model for the mineralization of bone [_eprint: https://onlinelibrary.wiley.com/doi/pdf/10 *Journal of Orthopaedic Research*, *12*(3), 375–383. https://doi.org/10.1002/jor.1100120310

Martin, R. B. (1991). Determinants of the mechanical properties of bones. *Journal of Biomechanics*, *24*, 79–88. https://doi.org/10.1016/0021-9290(91)90379-2

Matan. (2023, March). Polarization density | description, example & application. https://your-physicist.com/polarization-density/

Matic, I., Matthews, B. G., Wang, X., Dyment, N. A., Worthley, D. L., Rowe, D. W., Grcevic, D., & Kalajzic, I. (2016). Quiescent bone lining cells are a major source of osteoblasts during adulthood. *Stem Cells*, *34*(12), 2930–2942. https://doi.org/10.1002/stem.2474

Mazess, R. B. (1982). On aging bone loss. *Clinical Orthopaedics and Related Research®*, *165*, 239. Retrieved May 13, 2025, from https://journals.lww.com/clinorthop/citation/1982/05000/on_aging_bone_loss.37.aspx

McClung, M. R. (2005). The relationship between bone mineral density and fracture risk. *Current Osteoporosis Reports*, *3*(2), 57–63. https://doi.org/10.1007/s11914-005-0005-y

Meunier, P. J., & Boivin, G. (1997). Bone mineral density reflects bone mass but also the degree of mineralization of bone: Therapeutic implications. *Bone*, *21*(5), 373–377. https://doi.org/10.1016/S8756-3282(97)00170-1

Milovanovic, P., Vom Scheidt, A., Mletzko, K., Sarau, G., Püschel, K., Djuric, M., Amling, M., Christiansen, S., & Busse, B. (2018). Bone tissue aging affects mineralization of cement lines. *Bone*, *110*, 187–193. https://doi.org/10.1016/j.bone.2018.02.004

Mitchell, J., & Van Heteren, A. H. (2016). A literature review of the spatial organization of lamellar bone. *Comptes Rendus Palevol*, *15*(1), 23–31. https://doi.org/10.1016/j.crpv.2015.04.007

Moss, M. L. (1997). The functional matrix hypothesis revisited. 2. the role of an osseous connected cellular network. *American Journal of Orthodontics and Dentofacial Orthopedics*, *112*(2), 221–226. https://doi.org/10.1016/S0889-5406(97)70249-X

Müller, R. (2009). Hierarchical microimaging of bone structure and function [Publisher: Nature Publishing Group]. *Nature Reviews Rheumatology*, *5*(7), 373–381. https://doi.org/10.1038/nrrheum.2009.107

National Institute of Biomedical Imaging and Bioengineering. (2023). Computed tomography (ct) [Accessed: 2025-05-30]. https://www.nibib.nih.gov/science-education/science-topics/computed-tomography-ct

Nguyen, N. (2021). Physique 3, 2021. Lecture slides [Unpublished teaching material].

Oliviero, F., & Punzi, L. (2022). Basics of polarized light microscopy. In B. F. Mandell (Ed.), *Synovial fluid analysis and the evaluation of patients with arthritis* (pp. 79–90). Springer International Publishing. https://doi.org/10.1007/978-3-030-99612-3_9

Oryan, A. (n.d.). Bone injury and fracture healing biology.

Palumbo, C., & Ferretti, M. (2021). The osteocyte: From "prisoner" to "orchestrator" [Number: 1 Publisher: Multidisciplinary Digital Publishing Institute]. *Journal of Functional Morphology and Kinesiology*, *6*(1), 28. https://doi.org/10.3390/jfmk6010028

Parfitt, A. M. (1994). Osteonal and hemi-osteonal remodeling: The spatial and temporal framework for signal traffic in adult human bone. *Journal of Cellular Biochemistry*, *55*(3), 273–286. https://doi.org/10.1002/jcb.240550303

Pazzaglia, U. E., Congiu, T., Marchese, M., & Dell'Orbo, C. (2010). The shape modulation of osteoblast–osteocyte transformation and its correlation with the fibrillar organization in secondary osteons. *Cell and Tissue Research*, *340*(3), 533–540. https://doi.org/10.1007/s00441-010-0970-z

Pazzaglia, U. E., Congiu, T., Marchese, M., Spagnuolo, F., & Quacci, D. (2012). Morphometry and patterns of lamellar bone in human haversian systems. *The Anatomical Record*, *295*(9), 1421–1429. https://doi.org/10.1002/ar.22535

Pfeiffer, S., Crowder, C., Harrington, L., & Brown, M. (2006). Secondary osteon and haversian canal dimensions as behavioral indicators. *American Journal of Physical Anthropology*, *131*(4), 460–468. https://doi.org/10.1002/ajpa.20454

Philips, C. (2024). Medical imaging, 2024. lecture slides [Unpublished teaching material].

Pilia, M., Guda, T., Shiels, S. M., & Appleford, M. R. (2013). Influence of substrate curvature on osteoblast orientation and extracellular matrix deposition. *Journal of Biological Engineering*, *7*(1), 23. https://doi.org/10.1186/1754-1611-7-23

Pilitsis, J. G., Lucas, D. R., & Rengachary, S. R. (2002). Bone healing and spinal fusion [Publisher: American Association of Neurological Surgeons]. *Neurosurgical focus*, *13*(6), 1–6. Retrieved March 25, 2025, from https://thejns.org/focus/view/journals/neurosurg-focus/13/6/foc.2002.13.6.2.xml

Portigliatti Barbos, M., Bianco, P., Ascenzi, A., & Boyde, A. (1984). Collagen orientation in compact bone: II. distribution of lamellae in the whole of the human femoral shaft with reference to its mechanical properties. *Metabolic Bone Disease and Related Research*, *5*(6), 309–315. https://doi.org/10.1016/0221-8747(84)90018-3

Raguin, E., & Streeter, M. A. (2018). Brief communication: Test of a method to identify double-zonal osteon in polarized light microscopy. *American Journal of Physical Anthropology*, *167*(2), 407–415. https://doi.org/10.1002/ajpa.23616

Redelstorff, R. (2012). Unique bone histology in partial large bone shafts from aust cliff (england, upper triassic): An early independent experiment in gigantism. *Acta Palaeontologica Polonica*. https://doi.org/10.4202/app.2012.0073

Repp, F. (2015, September 21). *Computational analysis of dynamic bone structure and processes* [Doctoral dissertation, Mathematisch-Naturwissenschaftliche Fakultät]. https://doi.org/10.18452/17308

Repp, F., Kollmannsberger, P., Roschger, A., Berzlanovich, A., Gruber, G. M., Roschger, P., Wagermaier, W., & Weinkamer, R. (2017). Coalignment of osteocyte canaliculi and collagen fibers in human osteonal bone. *Journal of Structural Biology*, *199*(3), 177–186. https://doi.org/10.1016/j.jsb.2017.07.004

Reznikov, N., Almany-Magal, R., Shahar, R., & Weiner, S. (2013). Three-dimensional imaging of collagen fibril organization in rat circumferential lamellar bone using a dual beam electron microscope reveals ordered and disordered sub-lamellar structures. *Bone*, *52*(2), 676–683. https://doi.org/10.1016/j.bone.2012.10.034

Reznikov, N., Chase, H., Brumfeld, V., Shahar, R., & Weiner, S. (2015). The 3d structure of the collagen fibril network in human trabecular bone: Relation to trabecular organization. *Bone*, *71*, 189–195. https://doi.org/10.1016/j.bone.2014.10.017

Reznikov, N., Shahar, R., & Weiner, S. (2014). Bone hierarchical structure in three dimensions. *Acta Biomaterialia*, *10*(9), 3815–3826. https://doi.org/10.1016/j.actbio.2014.05.024

Rho, J.-Y., Kuhn-Spearing, L., & Zioupos, P. (1998). Mechanical properties and the hierarchical structure of bone. *Medical Engineering & Physics*, *20*(2), 92–102. https://doi.org/10.1016/S1350-4533(98)00007-1

Robling, A. G., & Stout, S. D. (1999). Morphology of the drifting osteon. *Cells Tissues Organs*, *164*(4), 192–204. https://doi.org/10.1159/000016659

Roschger, A., Roschger, P., Wagermaier, W., Chen, J., van Tol, A. F., Repp, F., Blouin, S., Berzlanovich, A., Gruber, G. M., Klaushofer, K., Fratzl, P., & Weinkamer, R. (2019). The contribution of the pericanalicular matrix to mineral content in human osteonal bone. *Bone*, *123*, 76–85. https://doi.org/10.1016/j.bone.2019.03.018

Roschger, P., Fratzl, P., Eschberger, J., & Klaushofer, K. (1998). Validation of quantitative backscattered electron imaging for the measurement of mineral density distribution in human bone biopsies. *Bone*, *23*(4), 319–326. https://doi.org/10.1016/S8756-3282(98)00112-4

Roschger, P., Gupta, H. S., Berzlanovich, A., Ittner, G., Dempster, D. W., Fratzl, P., Cosman, F., Parisien, M., Lindsay, R., Nieves, J. W., & Klaushofer, K. (2003). Constant mineralization density distribution in cancellous human bone. *Bone*, *32*(3), 316–323. https://doi.org/10.1016/S8756-3282(02)00973-0

Roschger, P., Paschalis, E. P., Fratzl, P., & Klaushofer, K. (2008). Bone mineralization density distribution in health and disease. *Bone*, *42*(3), 456–466. https://doi.org/10.1016/j.bone.2007.10.021

Ruffoni, D., Fratzl, P., Roschger, P., Klaushofer, K., & Weinkamer, R. (2007). The bone mineralization density distribution as a fingerprint of the mineralization process. *Bone*, *40*(5), 1308–1319. https://doi.org/10.1016/j.bone.2007.01.012

Ruffoni, D., Fratzl, P., Roschger, P., Phipps, R., Klaushofer, K., & Weinkamer, R. (2008). Effect of temporal changes in bone turnover on the bone mineralization density distribution: A computer simulation study. *Journal of Bone and Mineral Research*, *23*(12), 1905–1914. https://doi.org/10.1359/jbmr.080711

Schneider, P., Meier, M., Wepf, R., & Müller, R. (2010). Towards quantitative 3d imaging of the osteocyte lacuno-canalicular network. *Bone*, *47*(5), 848–858. https://doi.org/10.1016/j.bone.2010.07.026

Schrof, S., Varga, P., Galvis, L., Raum, K., & Masic, A. (2014). 3d raman mapping of the collagen fibril orientation in human osteonal lamellae. *Journal of Structural Biology*, *187*(3), 266–275. https://doi.org/10.1016/j.jsb.2014.07.001

Sedlin, E. D., Frost, H. M., & Villanueva, A. R. (1963). Age changes in resorption in human rib cortex. *Journal of Gerontology*, *18*(4), 345–349.

Seeman, E., & Delmas, P. D. (2006). Bone quality — the material and structural basis of bone strength and fragility. *New England Journal of Medicine*, *354*(21), 2250–2261. https://doi.org/10.1056/NEJMra053077

Sims, N. A., & Vrahnas, C. (2014). Regulation of cortical and trabecular bone mass by communication between osteoblasts, osteocytes and osteoclasts. *Archives of Biochemistry and Biophysics*, *561*, 22–28. https://doi.org/10.1016/j.abb.2014.05.015

Stauber, M., & Müller, R. (2008). Micro-computed tomography: A method for the non-destructive evaluation of the three-dimensional structure of biological specimens. In J. J. Westendorf (Ed.), *Osteoporosis: Methods and protocols* (pp. 273–292). Humana Press. https://doi.org/10.1007/978-1-59745-104-8_19

Stockhausen, K. E., Qwamizadeh, M., Wölfel, E. M., Hemmatian, H., Fiedler, I. A. K., Flenner, S., Longo, E., Amling, M., Greving, I., Ritchie, R. O., Schmidt, F. N., & Busse, B. (2021). Collagen fiber orientation is coupled with specific nano-compositional patterns in dark and bright osteons modulating their biomechanical properties [Publisher: American Chemical Society]. *ACS Nano*, *15*(1), 455–467. https://doi.org/10.1021/acsnano.0c04786

Tata, B. V. R., & Raj, B. (1998). Confocal laser scanning microscopy: Applications in material science and technology. *Bulletin of Materials Science*, *21*(4), 263–278. https://doi.org/10.1007/BF02744951

Tits, A. (2023). *Attaching soft to hard: A multimodal correlative investigation of the tendon-bone interface* [Doctoral dissertation, ULiège - Université de Liège [Sciences Appliquées], Liège, Belgium].

Turčanová, M., Hrtoň, M., Dvořák, P., Novák, K., Hermanová, M., Bednařík, Z., Polzer, S., & Burša, J. (2021). Full-range optical imaging of planar collagen fiber orientation using polarized light microscopy [_eprint: https://onlinelibrary.wiley.com/doi/pdf/10.1155/2021/6879765]. *BioMed Research International*, *2021*(1), 6879765. https://doi.org/10.1155/2021/6879765

van Oers, R. F. M., Ruimerman, R., Tanck, E., Hilbers, P. A. J., & Huiskes, R. (2008). A unified theory for osteonal and hemi-osteonal remodeling. *Bone*, *42*(2), 250–259. https://doi.org/10.1016/j.bone.2007.10.009

van Tol, A. F., Roschger, A., Repp, F., Chen, J., Roschger, P., Berzlanovich, A., Gruber, G. M., Fratzl, P., & Weinkamer, R. (2020). Network architecture strongly influences the fluid flow pattern through the lacunocanalicular network in human osteons. *Biomechanics and Modeling in Mechanobiology*, *19*(3), 823–840. https://doi.org/10.1007/s10237-019-01250-1

Varga, P., Pacureanu, A., Langer, M., Suhonen, H., Hesse, B., Grimal, Q., Cloetens, P., Raum, K., & Peyrin, F. (2013). Investigation of the three-dimensional orientation of mineralized collagen fibrils in human lamellar bone using synchrotron x-ray phase nano-tomography. *Acta Biomaterialia*, *9*(9), 8118–8127. https://doi.org/10.1016/j.actbio.2013.05.015

Wagermaier, W., S. Gupta, H., Gourrier, A., Burghammer, M., Roschger, P., & Fratzl, P. (2006). Spiral twisting of fiber orientation inside bone lamellae. *Biointerphases*, *1*(1), 1–5. https://doi.org/10.1116/1.2178386

Watkins, M., Grimston, S. K., Norris, J. Y., Guillotin, B., Shaw, A., Beniash, E., & Civitelli, R. (2011). Osteoblast connexin43 modulates skeletal architecture by regulating both arms of bone remodeling [Publisher: American Society for Cell Biology (mboc)]. *Molecular Biology of the Cell*, *22*(8), 1240–1251. https://doi.org/10.1091/mbc.e10-07-0571

Webb, J., & Tricker, J. (2000). A review of fracture healing. *Current Orthopaedics*, *14*(6), 457–463. https://doi.org/10.1054/cuor.2000.0145

Weinbaum, S., Cowin, S. C., & Zeng, Y. (1994). A model for the excitation of osteocytes by mechanical loading-induced bone fluid shear stresses. *Journal of Biomechanics*, *27*(3), 339–360. https://doi.org/10.1016/0021-9290(94)90010-8

Weiner, S., Arad, T., Sabanay, I., & Traub, W. (1997). Rotated plywood structure of primary lamellar bone in the rat: Orientations of the collagen fibril arrays. *Bone*, *20*(6), 509–514. https://doi.org/10.1016/S8756-3282(97)00053-7

Weiner, S., Traub, W., & Wagner, H. (1999). Lamellar bone: Structure–function relations. *Journal of Structural Biology*, *126*(3), 241–255. https://doi.org/10.1006/jsbi.1999.4107

Wess, T. J., & Orgel, J. P. (2000). Changes in collagen structure: Drying, dehydrothermal treatment and relation to long term deterioration. *Thermochimica Acta*, *365*(1), 119–128. https://doi.org/10.1016/S0040-6031(00)00619-5

Whitehouse, W. J., & Dyson, E. D. (1974). Scanning electron microscope studies of trabecular bone in the proximal end of the human femur. *Journal of Anatomy*, *118*, 417–444. Retrieved May 11, 2025, from https://www.ncbi.nlm.nih.gov/pmc/articles/PMC1231543/

Withers, P. J. (2007). X-ray nanotomography. *Materials Today*, *10*(12), 26–34. https://doi.org/10.1016/S1369-7021(07)70305-X

Wolman, M. (1975). Polarized light microscopy as a tool of diagnostic pathology. [Publisher: Journal of Histochemistry & Cytochemistry]. *Journal of Histochemistry & Cytochemistry*, *23*(1), 21–50. https://doi.org/10.1177/23.1.1090645